

# DESIGN OF A LINEAR INDUCTION MACHINE FOR RAILWAY SYSTEMS USING FINITE ELEMENT CALCULATION

Dem Fachbereich 18  
Elektrotechnik und Informationstechnik  
der Technischen Universität Darmstadt  
zur Erlangung des akademischen Grades  
einer Doktor-Ingenieurin (Dr.-Ing.)  
vorgelegte Dissertation

von

**Martina Hofmann**

geboren am 15. August 1973  
in Gross-Umstadt

Referent:	Prof. Dr.-Ing. habil. Andreas Binder
Korreferent:	Prof. Dr.-Ing. Dave Rodger
Tag der Einreichung:	2. Juli 2001
Tag der mündlichen Prüfung:	3. Dezember 2001

Berichte aus der Elektrotechnik

**Martina Hofmann**

**Design of a Linear Induction Machine  
for Railway Systems  
using Finite Element Calculation**

D 17 (Diss. TU Darmstadt)

Shaker Verlag  
Aachen 2002

Die Deutsche Bibliothek - CIP-Einheitsaufnahme

*Hofmann, Martina:*

Design of a Linear Induction Machine for Railway Systems  
using Finite Element Calculation / Martina Hofmann.

Aachen : Shaker, 2002

(Berichte aus der Elektrotechnik)

Zugl.: Darmstadt, Techn. Univ., Diss., 2001

ISBN 3-8265-9953-5

Copyright Shaker Verlag 2002

All rights reserved. No part of this publication may be reproduced, stored in a retrieval system, or transmitted, in any form or by any means, electronic, mechanical, photocopying, recording or otherwise, without the prior permission of the publishers.

Printed in Germany.

ISBN 3-8265-9953-5

ISSN 0945-0718

Shaker Verlag GmbH • P.O. BOX 1290 • D-52013 Aachen

Phone: 0049/2407/9596-0 • Telefax: 0049/2407/9596-9

Internet: [www.shaker.de](http://www.shaker.de) • eMail: [info@shaker.de](mailto:info@shaker.de)

*To Frank.*



*Then I saw all the work of God, and that man may not get knowledge of the work which is done under the sun; because, if a man gives hard work to the search he will not get knowledge, and even if the wise man seems to be coming to the end of his search, still he will be without knowledge.*

*Ecclesiastes 8:17*

# Table of Contents

Table of Contents	vii
Abstract	xi
Acknowledgements	xii
Introduction	1
<b>1 Fundamentals of linear electric machines and electromagnetics</b>	<b>5</b>
1.1 Theory of linear induction drives . . . . .	5
1.1.1 The traveling magnetic field and the definition of slip . . . . .	7
1.1.2 Equivalent circuit . . . . .	8
1.1.3 Winding peculiarities . . . . .	9
1.1.4 Coil parameters . . . . .	12
1.1.5 Power flow and losses . . . . .	15
1.1.6 Thermal loads and conventions . . . . .	16
1.1.7 Flux density . . . . .	17
1.1.8 Tractive effort . . . . .	18
1.2 Electromagnetic theory . . . . .	20
1.2.1 Numerical methods in electromagnetics . . . . .	20
1.2.2 On the Finite Element Program <i>MEGA</i> . . . . .	22
1.2.3 2-D Problems . . . . .	23
1.2.4 3-D Problems . . . . .	24
1.2.5 Difference of 2-D and 3-D calculations . . . . .	27
<b>2 Initial considerations for the linear machine design</b>	<b>28</b>
2.1 Definition of design constraints for linear machines in the railway system . . . .	28
2.2 Feasibility of different kinds of linear machines in railway applications . . . .	31
2.3 Determination of maximum available space for the linear machine . . . . .	32
<b>3 Numerical calculation of the linear eddy current brake</b>	<b>35</b>
3.1 Introduction . . . . .	35
3.1.1 Geometrical considerations . . . . .	35
3.1.2 Finite Element modeling . . . . .	35
3.2 Evaluation of longitudinal end effects by two-dimensional calculations . . . . .	38
3.2.1 Influence of longitudinal end effects on force generation . . . . .	40
3.2.2 Flux density characteristics . . . . .	41

3.2.3	Longitudinal end effect factor . . . . .	44
3.3	Numerical 3-D calculation of an eddy current brake . . . . .	45
3.3.1	Three-dimensional modeling . . . . .	45
3.3.2	Results of force calculation . . . . .	46
3.3.3	Flux density and eddy current distribution . . . . .	48
3.4	Comparison of calculated and measured eddy current brake . . . . .	51
3.4.1	Comparison of force characteristics . . . . .	51
3.4.2	Comparison of flux density characteristics . . . . .	54
3.5	Concluding remarks to the calculation of the linear eddy current brake . . . .	56
<b>4</b>	<b>Numerical calculation of a linear induction machine</b>	<b>57</b>
4.1	Determination of initial conditions . . . . .	57
4.1.1	Evaluation of winding concepts . . . . .	57
4.1.2	Prerequisites for the machine design . . . . .	59
4.2	Calculation of a linear induction machine with fractional slot winding . . . . .	60
4.2.1	Geometrical considerations . . . . .	60
4.2.2	Finite Element modeling . . . . .	63
4.2.3	Results of the force calculations . . . . .	65
4.2.4	Flux density characteristics . . . . .	68
4.3	Calculation of a linear induction machine with integer slot yoke winding . . . .	70
4.3.1	Choice of the winding . . . . .	70
4.3.2	Finite Element modeling . . . . .	74
4.4	Evaluation of longitudinal end effects by two-dimensional calculations . . . . .	75
4.4.1	Flux density characteristics . . . . .	75
4.4.2	Influence of longitudinal end effects on force generation . . . . .	80
4.4.3	Longitudinal end effect factor . . . . .	81
4.5	Comparison of linear induction machine with fractional slot and integer slot yoke winding . . . . .	83
4.5.1	Analytical calculation of the coil resistance . . . . .	83
4.5.2	Results of the force calculations . . . . .	85
4.5.3	Additional tractive effort . . . . .	88
4.5.4	Flux density characteristics . . . . .	89
4.5.5	Power calculation . . . . .	94
4.6	Comparison of calculated and measured linear induction machine . . . . .	98
4.6.1	Comparison of measurement and calculation . . . . .	98
4.6.2	Investigation of the impact of conductivity on the calculation results . .	103
4.7	Concluding remarks to the calculation of the linear induction machine . . . . .	105
<b>5</b>	<b>Measurements</b>	<b>106</b>
5.1	Measurements with the DC eddy current brake . . . . .	106
5.1.1	Experimental set-up of the measurement . . . . .	106
5.1.2	Measurement results . . . . .	109
5.2	Measurement with the AC linear induction machine . . . . .	111
5.2.1	Experimental set-up of the measurement . . . . .	111
5.2.2	Measurement results . . . . .	115
5.3	Measurement of the rail conductivity . . . . .	119

---

5.4 Measurement fault detection . . . . .	120
<b>6 Summary and Conclusions</b>	<b>121</b>
<b>List of Symbols and Abbreviations</b>	<b>123</b>
<b>A Material composition of the used rail profiles</b>	<b>128</b>
<b>B Finite Element models</b>	<b>129</b>
<b>C Measurement devices</b>	<b>134</b>
C.1 Measurement transducer . . . . .	134
C.2 Force transducer . . . . .	134
C.3 <i>Hall</i> probe . . . . .	135
<b>D Locomotive <i>BR152</i></b>	<b>138</b>
<b>Bibliography</b>	<b>139</b>
<b>Index</b>	<b>145</b>



# Abstract

This work deals with the design of a linear induction machine for the application in the railway system. The railway regulations and standards give the boundary conditions for the design. The main design tool is the Finite Element program *MEGA*.

In the first part, fundamental laws and design constraints are given to introduce the reader to the tools used further on. Due to railway restrictions, the available space for the design is limited.

The second part deals with the linear eddy current brake. This machine has been available for measurements and is therefore used for verification of the calculations. Measurement data derived from own measurements as well as from publications is compared with calculation results.

The third part involves two possible designs for the linear induction machine, which are compared with each other. These designs arise from the space restrictions and are namely the fractional slot winding and the integer slot winding approach. For the design it is assumed to use water cooled coils to obtain maximum forces.

In the last part, the measurements on a linear induction machine are presented, which were carried out in the laboratory of the Institute of Electrical Energy Conversion. These measurements were made with the modified eddy current brake.

# Acknowledgements

I would like to thank Prof. Dr.-Ing. habil. Andreas Binder the head of the Institute of Electrical Energy Conversion for being my supervisor and for his many suggestions and constant support during this research. I am also very thankful to Dr.-Ing. Rudolf Pfeiffer for his guidance through many problems and for his unlimited support.

Many thanks go to the group of the Applied Electromagnetics Research Centre from the Bath University, UK. Special thanks to Dr. Paul Leonard for his continuing support and his enormous patience during the years of my work, constantly finding answers to silly questions. To Professor Dave Roger for being my secondreader, for saving me when everything seemed to be lost and for always finding the best pub.

The Institute of Electrical Energy Conversion has been my second home for four years. This is not only because I spent a lot of time there, but because there are great people. Thanks to all members (academic and non-academic) of the Institute of Electrical Energy Conversion and of the Department of Renewable Energy.

Of course, I am grateful to my family for their patience and support. Without them this work would never have come into existence. Special thanks to my father, Werner Hofmann for all the practical help and the wisdom, to my sister, Dr. Heike Endepols for all the proofreading and the fruitful discussions and to my boy-friend, Frank Wehrheim for staying on my side even in bad times. Thanks to Erich Daub for doing the last corrections and for the music.

Darmstadt,  
February 18, 2002

Martina Hofmann

# Introduction

In these days, the need for fast transportation devices requires new concepts for effective drives. There are different kinds of drives available for every kind of application. Their common feature is the conversion from different forms of energy (mostly chemical and electrical) into mechanical energy which is then driving a vehicle. One of the most important vehicles nowadays is the electric locomotive running on a rail. It is widely used throughout the world for transportation of goods and passengers over long distances. For this task, it is necessary to use effective drives at the locomotive in order to save energy and to provide safe and predictable transportation. The locomotive must be enabled to generate the needed tractive effort, which is the force moving the train. This force is often generated by conventional rotary machines which are located on a wheelset. They produce a torque on the wheel axis which leads to a rotation of the wheel itself. The wheel is carried by the rail. There is a mechanical contact between wheel and rail. Different forces are acting on the wheel-rail contact. The weight of the locomotive multiplied with the gravitational constant is acting as a normal force and the torque of the wheel-axis is generated by a tangential force due to friction between wheel and rail. This tangential force is causing an acceleration of the locomotive depending on the slip between wheel and rail. The generation of the tractive effort of a locomotive is explained in detail in chapter 1.1.8.

The increase of tractive effort can be put into practice by several methods. One possibility is to find the optimum of adhesion between wheel and rail for any condition. This can be done by controlling the slip between rail and wheel (which is already developed and put into operation [1]). Another method is to introduce an additional device which is independent of mechanical contact. One step into this direction was done by a German company (*Knorr-Bremse*) [2], which has developed a linear eddy current brake for the new German high speed train *ICE 3*. This linear brake is mounted between the two wheels on the bogie. It works independently from weather conditions and wheel-rail-adhesion. But this device can only generate braking forces in combination with attractive forces (see Figure 1).

Depending on the velocity of the locomotive, the maximum normal and tangential force components are designated. So, there was the idea to develop a similar linear machine which has additional features. It should be able to generate braking, accelerating and attracting forces, independent from the train speed.



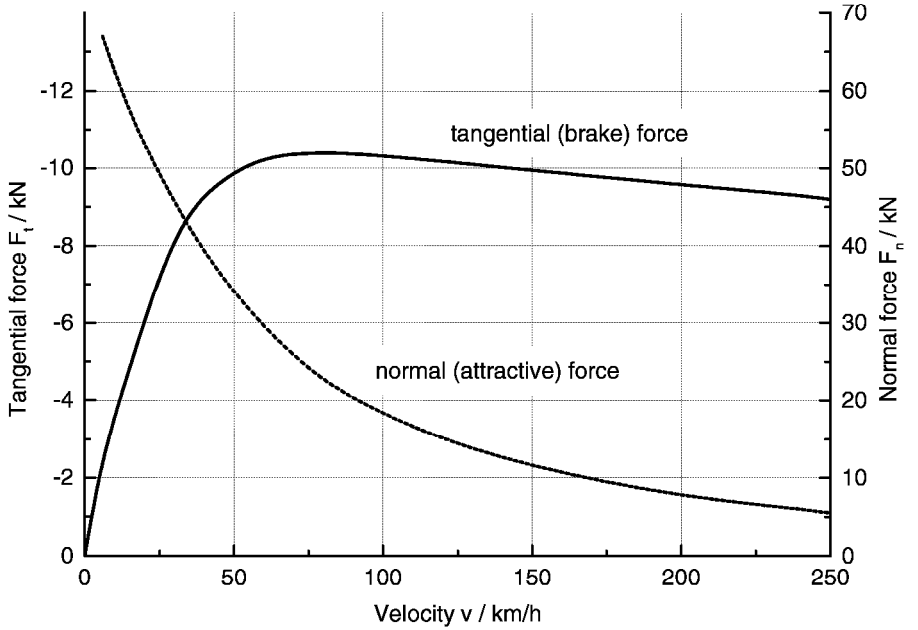


Figure 1: Measured forces of the six-pole eddy current brake [2]. The force was measured at an excitation of 67 kA ampere-turns per slot.

In order to realize this aim, an (asynchronous) linear induction machine (ALIM) will be designed and investigated. A general characteristic of an induction machine is shown in Figure 2.

Assuming that the machine is supplied by a frequency inverter, the characteristic curves could be shifted by changing the supply frequency. This makes it possible to obtain a wide variety of force components. Within the thermal limits of the machine and the inverter capability, the set of normal and tangential force can be chosen according to the characteristic curve independent of the train speed.

The induction machine will be designed as a linear short stator with the massive iron rail as secondary. The primary part with the three-phase winding will be mounted beneath the bogies (two ALIMs per bogie). It will operate as a booster to enhance the tractive effort of electric locomotives under wet weather conditions, when the tangential force of the wheel-rail contact is reduced.

The booster will provide additional accelerating and braking forces. The attractive force between wheel and rail can be used to amplify the vertical force on the wheels to compensate bad adhesion conditions. Furthermore, by choosing a frequency which is according to a zero tangential and a big normal force component, the locomotive will be pulled to the rail. This

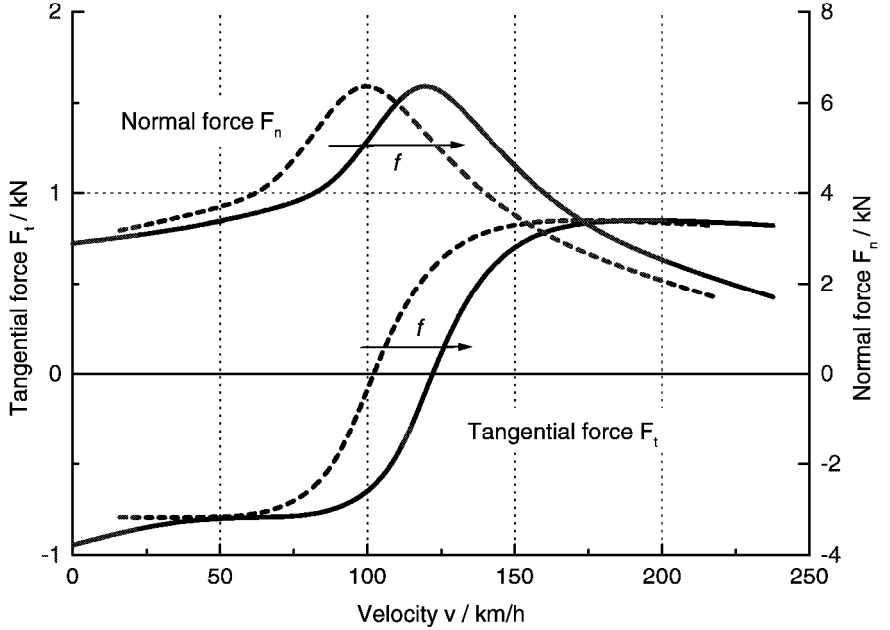


Figure 2: Force curves of a linear induction machine with different frequencies applied.

may be used to increase security of high speed trains in case of strong crosswind to hold the locomotive on the track.

The application of linear machines in railway systems has a long history and started in 1892 with a patent of the *electro-magnetic brake* [3, 4]. It continued in 1905 with the publications of *Wilson* [5] and *Zehden* [6, 7]. Then, it took more than half a century until this idea was revived for high-speed transportation systems in the 1970s. Since then, many countries (like Germany, Japan, USA, Canada, UK and Romania) have contributed to the ongoing design of linear machines mainly for high-speed applications.

The German research on linear machines for railway systems focuses mainly on the *Transrapid* [8] and the *linear eddy current brake* [2], [9], [10], [11]. This thesis arose from the endeavor of the German railway company *Deutsche Bahn AG* to develop a linear machine similar to the existing eddy current brake, but with additional features. Therefore, the work on linear eddy current brakes ([2], [11]) has been the basis for the computation of linear machines. For the further investigations on linear induction machines, it was possible to use fundamental work from some time ago [12] as well as today's research [13].

This work is an attempt to investigate the application of linear induction machines in the railway system of the German railways. It is intended to be a feasibility study for the currently

available technology and environment.

In the following chapters, the mainly used fundamentals in electromagnetics will be listed. The linear machine will be introduced with its historical context and the design constraints. Then, a chapter on the linear eddy current brake shows the initial considerations on the numerical approach for linear machines and presents calculated and measured results. The main part of this thesis is the chapter on the linear induction machine. The design of two different approaches will be shown. They are compared with each other by electrical parameters like flux density and power and by mechanical aspects like forces and their effect on the train. Finally, the measurements which were performed in the laboratory of the Institute of Electrical Energy Conversion are shown and discussed.

Calculations have been carried out using numerical and analytical methods. The numerical calculations have been performed with the Finite Element program package *MEGA* on a *DEC Alpha* workstation *500 au* with 512 Megabyte RAM running on *Digital Unix*.

# Chapter 1

## Fundamentals of linear electric machines and electromagnetics

In the following subsections, some fundamental laws are given, which are essential for dealing with numerical calculation and the design of electrical machines. All variables are listed in chapter 6.

### 1.1 Theory of linear induction drives

When confronted with a linear machine, many people have difficulties with imagining the working principle. Even though the linear machine was invented in 1841 [13] and is used in many industrial applications nowadays, the rotary machine is still more popular. A simple method of understanding linear machines is to imagine that the primary member of a conventional rotary motor has been cut by a radial plane and then unrolled, as shown in Figure 1.1 [7].

The rotor is replaced by a conducting sheet or plane. The stator is then designated as the primary and the rotor as the secondary<sup>1</sup>. The primary now has a finite length with a beginning and an end.

The presence of these two ends leads to the phenomenon of longitudinal end effects which does not exist in conventional rotating machines. In Figure 1.2, a DC-excited linear machine is shown for different velocities.

The flux lines are shown to demonstrate the longitudinal end effect. The upper sketch shows the linear machine with zero velocity. One can see that the inner poles are alternating between north and south poles with almost constant flux line distribution. At the left and the right end of the machine, the flux lines are shaped differently. The flux is weakened and distorted. At a velocity of 18 km/h, the end effect is amplified. There is still a weakened flux at both ends. Additionally, due to the motion, there is a distortion of the flux even at the inner poles. Whereas the velocity of the primary is going to the negative  $x$ -direction, the flux

<sup>1</sup>In the following chapters, the primary part will correspond to the stator and the secondary part to the rotor. This is important for the nomenclature of the variables.

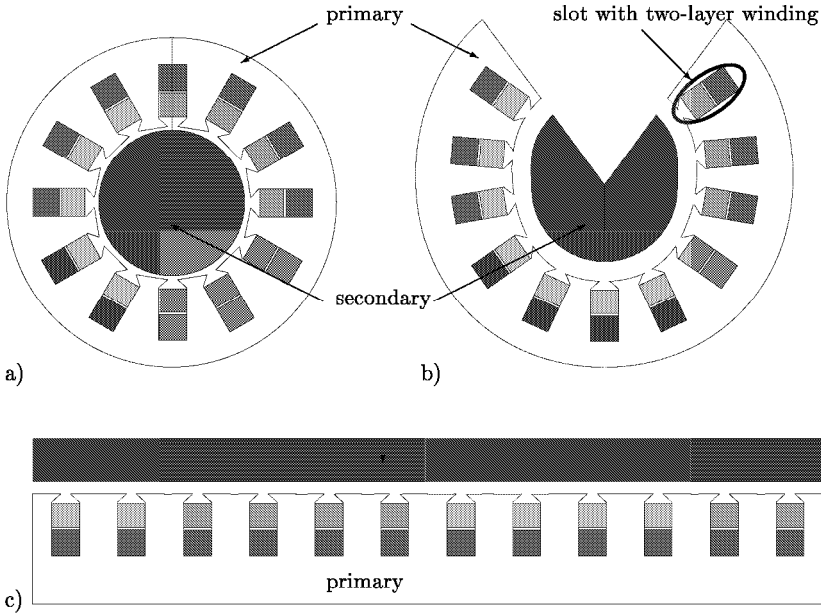


Figure 1.1: Imaginary process of unrolling a conventional machine to obtain a linear induction machine: a) rotary machine, b) rotary machine cut by a radial plane and started to unroll, c) completely unrolled rotary machine gives linear machine

lines in the secondary seem to be moving into positive  $x$ -direction. Thus, the flux at the entry end of the linear machine is weakened and the flux at the exit end is amplified.

This effect is increased with increasing velocity, decreasing number of poles and decreasing length of the primary [14, 15]. A more detailed investigation of longitudinal end effects will be shown in chapters 3.2 and 4.4.

Another phenomenon in an electric machine is called transversal end effect. It appears in every kind of machine (linear and rotating) due to the finite width of the machine itself. The transversal end effect might be compared with the longitudinal end effect at zero velocity and zero frequency as shown in Figure 1.2 a). It is not depending on the velocity, because the velocity is acting perpendicularly to the width of the machine. It only depends on the geometry of the primary part in  $y$ -direction.

To avoid misunderstandings in the definition of the direction of motion: In the FE models presented in this thesis, there is often a velocity applied. This velocity acts on the secondary part in the models into positive  $x$ -direction because this simplifies the modeling. For the presented results, it is always assumed, that the primary is moving to the negative  $x$ -direction as shown in Figure 1.2.

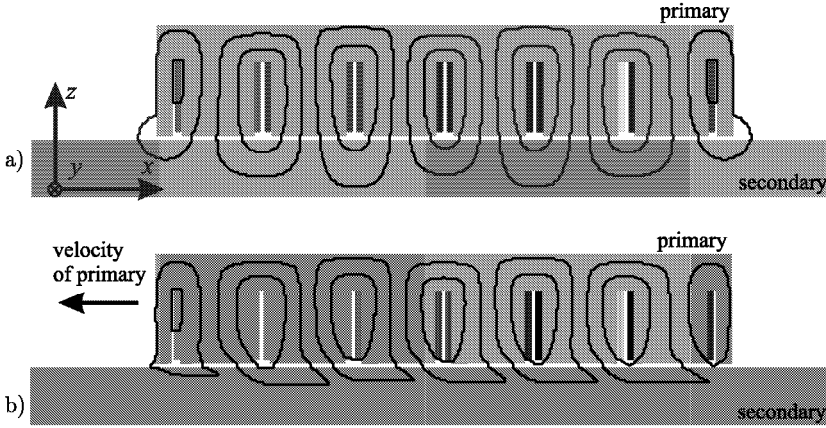


Figure 1.2: Sketch of a linear machine with flux lines at zero speed (a) and at 18 km/h (b) for DC excitation.

### 1.1.1 The traveling magnetic field and the definition of slip

For rotating machines, the slip is defined as the difference between the rotational speed of the traveling magnetic field (synchronous speed) and the rotational speed of the rotor related to the rotational speed of the traveling magnetic field (1.1).

$$s = \frac{n_{syn} - n}{n_{syn}} = 1 - \frac{n}{n_{syn}} \quad (1.1)$$

For the linear short stator induction machine with fixed secondary, this definition is not valid.

Assuming that the frequency is fixed, the synchronous speed of a rotating machine is replaced by the synchronous velocity of the linear traveling magnetic field (1.2), where  $\tau_p$  (pole pitch) is the geometric length of one pole.

$$v_{syn} = 2f\tau_p \quad (1.2)$$

This leads to a slip definition for linear induction machines as shown in (1.3).

$$s = \frac{v_{syn} - v}{v_{syn}} = 1 - \frac{v}{v_{syn}} \quad (1.3)$$

In order to illustrate the slip definitions, the different slip values for a linear induction machine are given in Table 1.1 related to Figure 1.3.

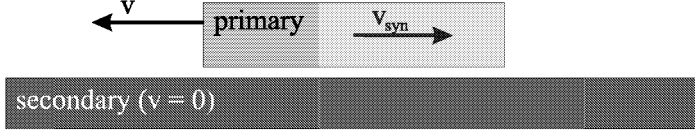


Figure 1.3: Sketch of a linear induction machine with indicated direction of the traveling magnetic field ( $v_{syn}$ ) and the direction of motion for the primary part ( $v$ ). The secondary part is not moving.

Table 1.1: Survey of the slip values for different velocities of the primary part at constant primary frequency (equivalent to fixed synchronous velocity).

velocity of primary	$v > v_{syn}$	$v = v_{syn}$	$v = v_{syn} \dots 0$	$v < 0$
slip	$s < 0$	$s = 0$	$s = 0 \dots 1$	$s > 1$

### 1.1.2 Equivalent circuit

According to [13] the equivalent circuit of a linear induction machine could be developed like shown in Figure 1.4.

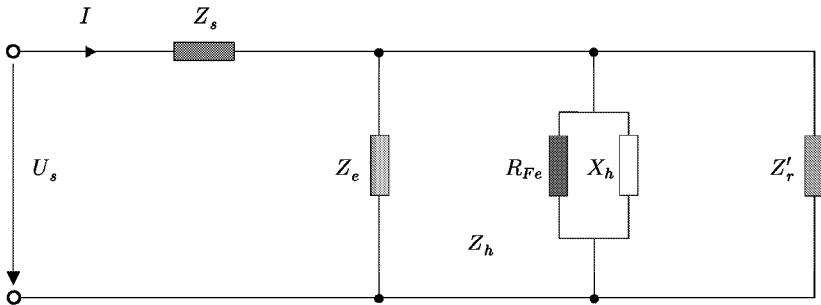


Figure 1.4: T-type equivalent circuit of a linear induction machine

The general behaviour is the same as for a rotary machine. The influence of the typical linear induction machine behaviour is expressed by an additional impedance  $Z_e$ . Equations (1.4) to (1.7) give the elements of the equivalent circuit.

$$Z_h = \frac{jX_h R_{Fe}}{jX_h + R_{Fe}} \quad , \quad (1.4)$$

$$Z_s = R_s + jX_s \quad (1.5)$$

$$\text{and} \quad Z'_r = \frac{R'_r}{s} + jX'_r \quad (1.6)$$

can be calculated in the same way as for a rotary induction machine as shown in [16], [17] and [18]. The impedance  $Z_e$  includes the end effect factor  $k_e$ , which is a complex equation. It can be derived by analytical calculations.

$$Z_e = \frac{1 - k_e}{k_e} \cdot \frac{Z_h Z'_r}{Z_h + Z'_r} \quad (1.7)$$

### 1.1.3 Winding peculiarities

In electrical machines there are always space harmonics with higher ordinal number due to the *Fourier* series expansion of the magnetic field distribution of the stator. These harmonics result from the distributed arrangement of the coils, the shape of teeth and slot openings. They move along the rotor with a higher or lower frequency than the fundamental wave and are heading in the same or the reverse direction of motion. This leads to time harmonics in the rotor e.m.f. with different frequencies. These rotor e.m.f.s cause rotor currents, which are interacting with the magnetic flux to produce driving or braking forces. Considering the principle of superposition, the generated forces of all harmonics are added to produce the final driving or braking force in the machine. These additional space harmonics lead to a force ripple and usually lead to lower values of the total force than the fundamental would produce alone.

One way of reducing this effect is to choose a fractional-pitch winding (chorded winding) with a proper pitch factor. This could drastically reduce the harmonic content of the machines output with only a small decrease in its fundamental component [19]. Chording of the coils reduces the fundamental linkage of the flux by the pitch factor

$$k_{p\nu} = \sin \left( \nu \frac{\pi w}{2 \tau_p} \right) \quad , \quad (1.8)$$

where  $\nu$  is the ordinal number of space harmonics,  $w$  the equivalent coil span and  $\tau_p$  the pole pitch.



In some cases (like  $q = 1$ , chording of  $2/3$ ), chording leads to an undesirable reduction of force generating flux (see Table 1.2). Therefore it is not recommended for this application, where  $q = 1$  is considered.

The ordinal numbers of space harmonics produced by a winding can be calculated with (1.9). It has to be calculated differently for different types of winding.

$$\begin{aligned}
 \text{Integer slot winding:} \quad \nu &= 1 + 2 \cdot m \cdot r & (1.9) \\
 &(q \text{ integer}) \\
 \text{Fractional slot winding:} \quad \nu &= \frac{2}{n} \cdot (1 + m \cdot r) \quad (n \text{ even}) \\
 &(q = \frac{z}{n}; z, n \text{ integer}) \\
 \nu &= \frac{1}{n} \cdot (1 + m \cdot r) \quad (n \text{ odd})
 \end{aligned}$$

$$\text{with: } r = 0, \pm 1, \pm 2, \pm 3, \dots$$

One of the most troublesome harmonics in AC machines are the slot harmonics. Their peculiarity is that they have the same distribution factor  $k_d$  (1.12) as the fundamental wave ( $\nu = 1$ ). Therefore, they usually have a negative impact on the e.m.f. in the rotor. A way to reduce the slot harmonics is to skew rotor conductors. The ordinal number of slot harmonics can be calculated using (1.10).

$$\nu = 1 + r \cdot \frac{Q}{p}, \quad \text{with } r = \pm 1, \pm 2, \pm 3, \dots \quad (1.10)$$

When the fractional slot winding is applied, the number of slots per pole and phase ( $q$ ) is usually an improper fraction  $q = \frac{z}{n}$ . The relation between  $q$  and other important winding parameters is given in (1.11) [18]

$$q = \frac{Q}{2mp}, \quad (1.11)$$

where  $Q$  is the number of slots,  $m$  the number of phases and  $p$  the number of pole pairs.

If the winding is not concentrated in one slot, but spread over more than one slot, the effective flux linkage of an uniformly distributed winding is expressed by the distribution factor  $k_d$  [16]. The distribution factor can be calculated using (1.12). This equation is valid for integer slot windings and for odd integer ordinal numbers of space harmonics  $\nu$  of fractional slot windings. For all other ordinal numbers of fractional slot windings, the distribution factor has to be calculated by geometrical addition of effective e.m.f. phasors divided by the arithmetic sum of these phasors (see [16] and [20]).

$$k_{d\nu} = \frac{\sin\left(\nu \frac{\pi}{2m}\right)}{z \sin\left(\nu \frac{\pi}{2mz}\right)} \quad (1.12)$$

where  $z$  is the numerator of  $q$  in case of a fractional slot winding.

The resulting influence of chording and winding is expressed by the winding factor

$$k_{w\nu} = k_{p\nu} \cdot k_{d\nu}. \quad (1.13)$$

For space harmonics with odd integer ordinal number, the fractional slot winding has the advantage of behaving as an integer slot winding with  $z$  slots per pole and phase. However, its disadvantage is the generation of more space harmonics with higher or lower ordinal number [16]. This effect is shown in Table 1.2 with a comparison of the distribution factors of fractional slot windings and integer slot windings.

Table 1.2: Winding factors for the space harmonics of different winding concepts. The number of phases  $m = 3$ .

ordinal number of space harmonics	$q = 1$ distrib. factor	$\frac{w}{\tau_p} = 1$ pitch factor	$q = 1$ distrib. factor	$\frac{w}{\tau_p} = \frac{2}{3}$ pitch factor	$q = \frac{1}{2}$ distrib. factor	$\frac{w}{\tau_p} = \frac{2}{3}$ pitch factor	$q = \frac{2}{7}$ distrib. factor	$\frac{w}{\tau_p} = \frac{7}{6}$ pitch factor
$\nu$	$ k_{d\nu} $	$ k_{p\nu} $	$ k_{d\nu} $	$ k_{p\nu} $	$ k_{d\nu} $	$ k_{p\nu} $	$ k_{d\nu} $	$ k_{p\nu} $
$\frac{1}{7}$	-	-	-	-	-	-	0.2588	0.2588
$-\frac{2}{7}$	-	-	-	-	-	-	0.5	0.5
$\frac{4}{7}$	-	-	-	-	-	-	0.866	0.866
$-\frac{5}{7}$	-	-	-	-	-	-	0.966	0.966
1	1	1	1	0.866	1	0.866	0.966	0.966
$-\frac{8}{7}$	-	-	-	-	-	-	0.866	0.866
$\frac{10}{7}$	-	-	-	-	-	-	0.5	0.5
$-\frac{11}{7}$	-	-	-	-	-	-	0.2588	0.2588
$\frac{13}{7}$	-	-	-	-	-	-	0.2588	0.2588
-2	-	-	-	-	1	0.866	0.5	0.5
...								
3	-	-	-	-	-	-	-	-
4	-	-	-	-	1	0.866	0.866	0.866
-5	1	1	1	0.866	1	0.866	0.2588	0.2588
6	-	-	-	-	-	-	-	-
7	1	1	1	0.866	1	0.866	0.2588	0.2588
-8	-	-	-	-	1	0.866	0.866	0.866

In the special case of  $q = 1/2$ , the distribution factor is not reduced compared to  $q = 1$ . However, for  $q = 2/7$ , the distribution factors are smaller than for  $q = 1$ . The disadvantage of the fractional slot winding can be seen for  $q = 2/7$ . Here, a big number of harmonics of lower and higher ordinal number are generated. Even for  $q = 1/2$ , there are more harmonics of higher ordinal number compared to  $q = 1$ .

### 1.1.4 Coil parameters

The coils of the linear machine can be modeled in the Finite Element program in a very special way as reduced scalar regions (see chapter 1.2.1). This means, that they are considered in the numerical models as carrying the current. But it is not possible to obtain the resistance of the coil out of the reduced scalar region. The resistance of the coils has to be calculated analytically. For AC problems, depending on the frequency, the current will not flow through the whole conductor surface due to the skin effect. The penetration depth [21] of the current in the coils is calculated using (1.14).

$$\delta_p = \sqrt{\frac{1}{\pi f \mu \kappa_{b_s}^{b_c}}} \quad (1.14)$$

The skin effect acting on the resistance of the coils can be separated into first and second order effect [16].

The first order skin effect is occurring when the conductor is divided into parallel wires which are connected either at the end of each turn or each coil or at the terminals. First, the worst case will be investigated with the connection of parallel wires at the end of each turn (see Figure 1.5).

Linked by different flux due to a different geometrical position in the slot, a voltage will be induced in the conductors, driving an additional eddy current through the conductors. The increase of resistance due to the higher eddy current losses in the conductors (first order skin effect) can be estimated using (1.15)-(1.19).

$$k_{r1} = \varphi(\xi) + \eta \cdot (\eta + 1) \cdot \psi(\xi) \quad (1.15)$$

$$\varphi(\xi) = \xi \cdot \frac{\sinh 2\xi + \sin 2\xi}{\cosh 2\xi - \cos 2\xi} \quad (1.16)$$

$$\psi(\xi) = 2 \cdot \xi \cdot \frac{\sinh \xi - \sin \xi}{\cosh \xi + \cos \xi} \quad (1.17)$$

$$\xi = \frac{h_o \cdot a}{\delta_p} \sqrt{\frac{l_{Fe}}{l_c}} \quad (1.18)$$

$$\text{worst case: } \eta = \frac{N_c - 1}{2}, \quad \text{best case: } \eta = -\frac{1}{2} \quad (1.19)$$

In the best case, the parallel wires would be connected at the terminals. The order of the conductors in the slot could be changed in layer 2 with respect to layer 1 (see Figure 1.5), so that the induced current would be very low.

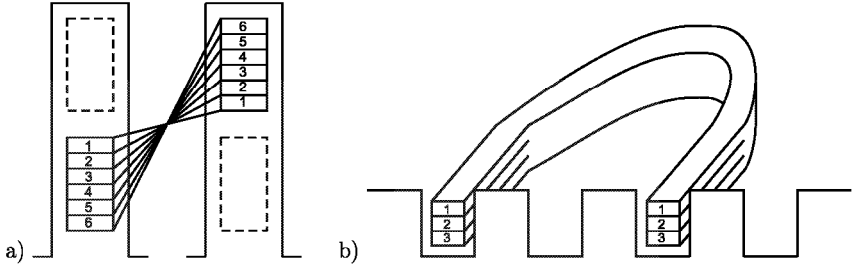


Figure 1.5: a) Sketch of a two-layer winding. The order of conductors for layer 1 is from bottom to top, whereas the order of conductors for layer 2 is from top to bottom (best case). b) Sketch of a winding with three parallel wires connected at the end of the turn (worst case).

In this case, the first order skin effect could be neglected within one coil. By the use of *Roebel* bars, the first order skin effect can be eliminated also for one bar per slot [22]. This can be achieved by varying the position of each wire throughout the whole width of the machine (= length of the slot). The use of *Roebel* bars is only possible if the width of the machine allows each wire to change place with every other layer a whole number of times.

The second order skin effect is due to the (slot) stray field of each wire acting on the other wires in the slot. The second order skin effect factor can be calculated with (1.16), (1.17), (1.20) and (1.21).

$$k_{r2} = \varphi(\xi^*) + p_p \cdot (p_p - 1) \cdot \psi(\xi^*) \quad (1.20)$$

$$\xi^* = \frac{h_o}{\delta_p} \quad (1.21)$$

In the winding overhangs, this effect is small enough to be neglected here. Therefore, the factor

$$k = \frac{1}{N_c \cdot a} \left( \sum_{p=1}^{N_c \cdot a} \varphi(\xi^*) + p_p \cdot (p_p - 1) \cdot \psi(\xi^*) \right) \quad (1.22)$$

has to be averaged on the whole turn by (1.23).

$$k = \frac{k \cdot l_{Fe} + l_c - l_{Fe}}{l_c} \quad (1.23)$$

For high current densities ( $J > 14 \text{ A/m}^2$ ) in the conductors, the coils need to be cooled to prevent a thermal overload of the machine at continuous operation. This can be achieved by using hollow conductors. In order to calculate the resistance of a hollow conductor, the "hollow conductor coefficient"  $\nu_h$  has to be used as an additional factor. The parameters of (1.24) are shown in Figure 1.6.

$$\nu_h = \frac{(w_o \cdot h_o^3 - w_i \cdot h_i^3) \cdot (w_o \cdot h_o - w_i \cdot h_i)}{w_o^2 \cdot h_o^4} \quad (1.24)$$

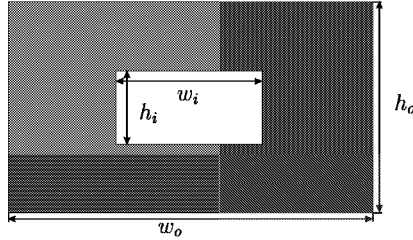


Figure 1.6: Hollow conductor with main parameters.

Finally, the coil resistance including the skin effects and the hollow conductor coefficient can be calculated using (1.25) and (1.24).

$$R_s = R_0 \cdot (1 + (k_{r1} - 1) \nu_h + (k - 1) \nu_h) \quad (1.25)$$

Eddy current losses in the winding overhangs due to the stray field are neglected.

### 1.1.5 Power flow and losses

The power flow diagram of an AC motor is shown in Figure 1.7.

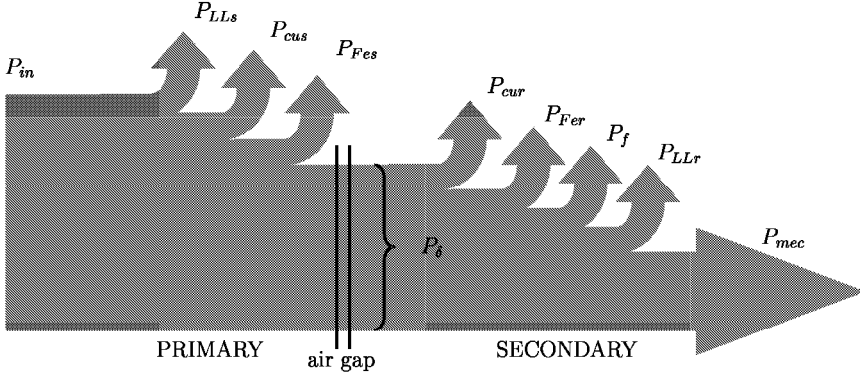


Figure 1.7: Power flow diagram of an AC motor. The input power flowing into the primary part (left side) is reduced by the primary copper losses and the primary core losses. Then it crosses the air gap and is again reduced by the secondary copper losses and the secondary core, friction and windage losses. In the end, the rest is transformed into mechanical power.

There are different categories of losses in AC machines:

- Constant losses
  - Losses in the active iron ( $P_{Fe}$ )
  - Losses due to friction and total windage losses ( $P_f$ )
- Load losses
  - Primary load loss ( $P_{cus}$ )
  - Secondary load loss ( $P_{cur}$ )
- Additional load losses ( $P_{LL}$ )
  - Active load losses in metal parts other than the conductors
  - Eddy current losses in conductors caused by current-dependent flux pulsation

The resistance of the rotor and stator coils can be measured. By knowing the supply current, the rotor and stator load losses can be calculated using (1.26).

$$P_{cu} = m \cdot I^2 \cdot R \quad (1.26)$$

By measuring the input power at no-load, the constant losses can be determined. The additional load losses are usually taken to be 0.5% - 1% of the output power of the machine [23].

If the electrical voltage and current at the terminals of a motor are given, then the input power can be calculated using (1.27) to (1.29) [24].

$$S = m \cdot U \cdot I^* \quad (1.27)$$

$$P_{in} = m \cdot \text{Re}\{U \cdot I^*\} \quad (1.28)$$

$$Q = m \cdot \text{Im}\{U \cdot I^*\} \quad (1.29)$$

The air gap power (1.30) could then be calculated by subtracting the losses in the primary from the input power.

$$P_\delta = P_{in} - P_{cus} - P_{Fes} - P_{LLs} \quad (1.30)$$

The mechanical power can be expressed with (1.31)

$$\begin{aligned} P_{mec} &= M \cdot \omega && \text{for a rotating machine, or} \\ P_{mec} &= F_t \cdot v && \text{for a linear machine.} \end{aligned} \quad (1.31)$$

The power factor  $\cos \varphi$  is given by (1.32).

$$\cos \varphi = \frac{P_{in}}{S} \quad (1.32)$$

### 1.1.6 Thermal loads and conventions

The thermal load of an electrical machine is an important quantity for the design. It might be expressed by the multiplication of the current-sheet  $A$  and the current-density  $J$ . The current-sheet simply expresses, how much current is flowing related to the surface of a machine (see Figure 1.8). It can be calculated with (1.33).

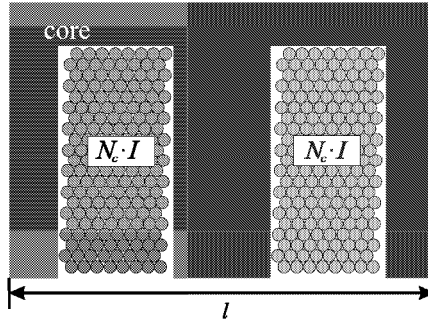


Figure 1.8: Sketch of two slots in the primary part of an electric machine. The slots are filled with  $N_c$  wires. Each wire carries the current  $I$ .

$$A = \frac{2 \cdot N_c \cdot I}{l} \quad (1.33)$$

The current-density represents how much current is flowing through the conductor cross-section. Using the parameters shown in Figure 1.6, the current-density will be calculated according to (1.34),

$$J = \frac{I}{w_o \cdot h_o - w_i \cdot h_i} \quad (1.34)$$

where  $I$  is the current flowing through one single conductor. The current-density is only an overall design parameter. The reduction of the conducting cross-section due to the skin effect is not considered for the calculation of  $J$ .

### 1.1.7 Flux density

The flux density is a very important phenomenon for dealing with electrical machines. The principle of electrical machines is based on the transformation of electrical energy to mechanical energy and vice versa by carrying energy across an air gap. This energy flow, already introduced as the air gap power, consists of the interaction of the primary and secondary electromagnetic fields.

Several laws, arising from *Maxwell's* equations, are given for dealing with this transformation [25]. *Ampere's* law (1.35) states how moving charges cause magnetic fields.

$$\oint_s \vec{H} \cdot d\vec{s} = \int_A \left( \frac{\partial \vec{D}}{\partial t} + \vec{J} \right) \cdot d\vec{A} \cong \int_A \vec{J} \cdot d\vec{A} \quad (\text{for low frequency}) \quad (1.35)$$



*Faraday's law* (1.36) states, how changing magnetic fields cause electric fields.

$$\oint_s \vec{E} \cdot d\vec{s} = - \int_A \frac{\partial \vec{B}}{\partial t} \cdot d\vec{A} \quad (1.36)$$

In both equations we can see the flux density if we substitute  $\vec{B} = \mu \cdot \vec{H}$  in (1.35). Also for the calculation of forces, the flux density is essential, as shown in (1.37) and (1.38) [26].

$$F_n = \int \frac{B_n^2 - B_t^2}{2\mu_0} \cdot dA \quad (1.37)$$

$$F_t = \int \frac{B_n \cdot B_t}{\mu_0} \cdot dA \quad (1.38)$$

A sketch of the used directions including normal and tangential direction and x, y and z as coordinates is shown in Figure 1.9.

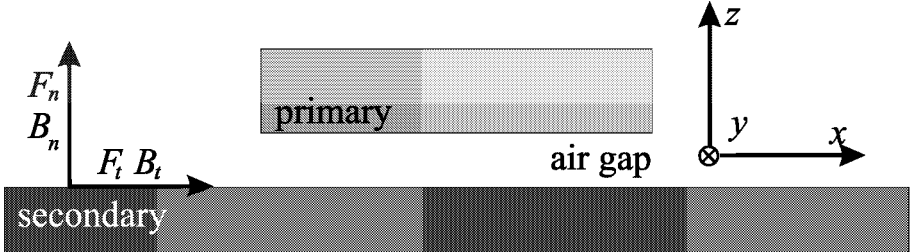
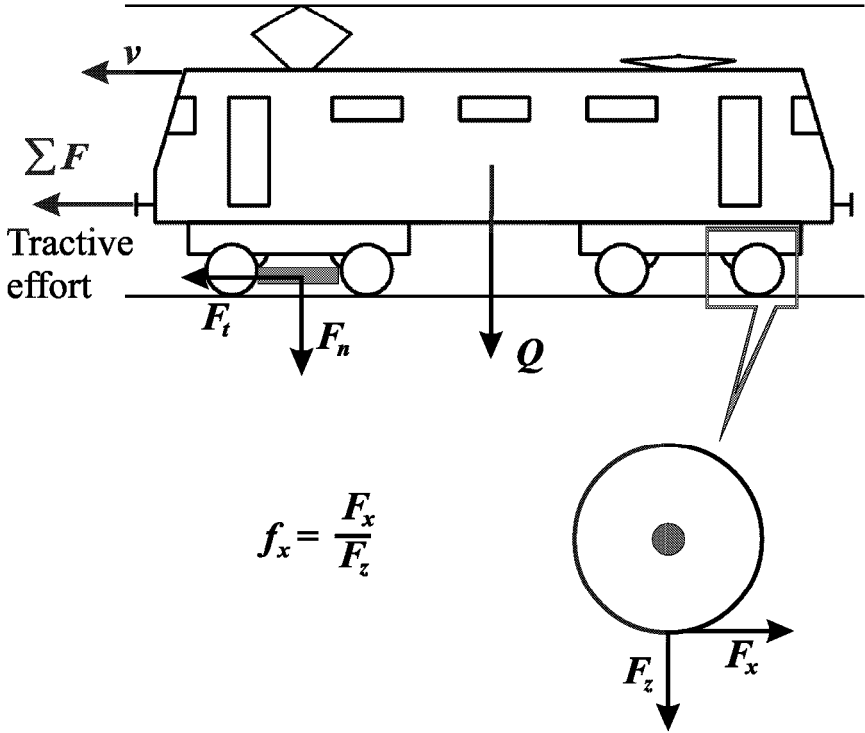


Figure 1.9: Sketch of used arrangement and direction definition.

In the following chapters, the flux density will always appear as a tool to explain processes and tendencies of the linear machines. It is significant for understanding and calculating effects in electrical machines. Besides, it is a measurable quantity which makes it even more important for the comparison of calculated and measured results.

### 1.1.8 Tractive effort

The tractive effort of a locomotive is the force that it exerts on the rail to overcome resistance such as inclines, wind drag and rolling resistance in order to drive or brake the train. It is dependent on the traction due to the wheel-rail contact and the torque transmitted from the drive to the wheels. Figure 1.10 shows a sketch of a locomotive with indicated tractive effort and forces between wheel and rail. A linear machine with a normal and tangential force component is included to show its influence on the tractive effort.



$$f_x = \frac{F_x}{F_z}$$

Figure 1.10: Sketch of the locomotive with indicated tractive effort, forces at the wheel-rail contact due to the adhesion coefficient and additional linear motor arrangement.

The tractive effort can be calculated with (1.39)

$$\Sigma F = (Q + F_n) \cdot f_x + F_t. \quad (1.39)$$

The biggest force component for the tractive effort is the force at the wheel-rail contact due to the torque of the main rotational drive. This torque can only be transformed into a tangential force if there is an adhesion between wheel and rail. The adhesion is depending on the surface conditions of the mechanical contact. For bad weather conditions (= wet/icy rail, slippery leaves on the rail), the adhesion conditions are poor with an adhesion coefficient of about  $f_x = 0.15$ . For good weather conditions (= dry rail), the adhesion coefficient is increased to a value of about  $f_x = 0.33^2$  [27]. The weight force  $Q$  and the normal force  $F_n$  are pressing

<sup>2</sup>For very good conditions, the adhesion coefficient can be even more than  $f_x = 0.4$ . Here, the value  $f_x = 0.33$  is used as an average value for good conditions.

the locomotive onto the rail and are thus determining the maximum transferable tangential force at the wheel-rail contact depending on the adhesion coefficient  $f_x$ . In general, the drive motors of the locomotive can produce the maximum transferable force at the wheel-rail contact. Therefore, the force calculation of (1.39) is always valid and moreover, care has to be taken to prevent the wheel from slipping. The tangential force component produced by the linear machine is directly added to the tractive effort.

## 1.2 Electromagnetic theory

The *Maxwell* equations are the fundamental set of equations which are used to define the electromagnetic field characteristics.

When the frequency of the exciting current or voltage is low (here:  $f < 1$  kHz), the displacement currents ( $\frac{\partial \vec{D}}{\partial t}$ ) can be neglected and the following subset of *Maxwell's* equations ((1.40)- (1.43)) [25] can be used.

$$\nabla \times \vec{H} = \vec{J} \quad (1.40)$$

$$\nabla \times \vec{E} + \frac{\partial \vec{B}}{\partial t} = 0 \quad (1.41)$$

$$\nabla \cdot \vec{D} = \varrho \quad (1.42)$$

$$\nabla \cdot \vec{B} = 0 \quad (1.43)$$

The constitutive relations are

$$\vec{B} = \mu \vec{H} \quad (1.44)$$

$$\vec{D} = \varepsilon \vec{E}. \quad (1.45)$$

### 1.2.1 Numerical methods in electromagnetics

There are different techniques available to solve electromagnetic field problems. These techniques can be classified as experimental, analytical or numerical. Experiments can be expensive, time consuming and even dangerous. Usually there are not many parameters which can

be varied within an experiment and sometimes vital parameters for understanding the physical behaviour of tested objects cannot be measured.

Analytical and numerical methods might be applied for problems which involve newly designed objects. Analytical methods are well tested and with the classical methods of separation of variables and integral equation solutions a wide range of electromagnetic problems can be solved. However, analytical methods require a high degree of ingenuity, experience and effort and only a narrow range of practical problems can be investigated due to complex geometries [28]. Therefore the need for numerical methods arises. These methods give approximate solutions of sufficient accuracy for engineering purposes.

Numerical computation of electromagnetic problems can be done by different methods. Some of the widely used possibilities are the Finite Element Method, the Finite Difference Method and the Finite Integration Technique.

The Finite Difference Method is one of the older differential schemes. In its original form, it requires a simple rectangular mesh, which has to be uniform. For example, the potential at the grid points of the rectangular mesh is computed by discretizing the governing differential equations for the electrostatic potential [25].

The Finite Element Method was intended to overcome difficulties of the Finite Difference Method by using other methods such as numerical evaluation of the variational integral, weighted residuals or the *Galerkin* approach [29]. It is a general technique for the solution of differential equations and at present the most advanced method for the solution of electromagnetic field problems [25]. The mesh does not have to be uniform and it might consist of elements with different shapes, such as triangular and quadrilateral in two dimensions (2-D) and tetrahedral and hexahedron in three dimensions (3-D).

The Finite Integration Technique has been developed specifically for the solution of *Maxwell's* equations. It presents a transformation of *Maxwell's* equations in integral form onto a grid pair. The Finite Integration Technique is a general numerical method for all electrodynamics and other subjects (e.g. acoustics, elastodynamics and temperature problems) derived from a generalization of the Finite Difference Time Domain method [29]. The grid is composed of elementary volumes, which are filled with a homogeneous material. Depending on the problem in hand, an appropriate grid type can be chosen, which might be triangular, quadrilateral and even irregular [30].

The numerical approaches have the advantage of allowing users to carry out calculations without knowledge of higher mathematics or physics. Nevertheless, it is required of the users to have a basic knowledge of physical laws to be able to detect errors within the numerical calculation. These errors might be due to an inappropriate mesh, wrong boundary conditions, wrong material properties or even misapprehension of the program itself.

### 1.2.2 On the Finite Element Program *MEGA*

The program *MEGA*, which is used in this thesis, is based on the Finite Element Method. It solves the low frequency subset of *Maxwell's* equations, including a wide variety of 2-D and 3-D problems [31]. The basic steps of the Finite Element Method are according to [32]:

- Discretization or subdivision of the domain
- Selection of the interpolation functions
- Formulation of the system of equations (forming a matrix)
- Solution of the system of equations

The solution of the whole system is approximated by a finite number of unknown coefficients. The most important capabilities of *MEGA* for this thesis are according to [31]:

- Steady-state AC with eddy currents using a complex number representation in 2-D and 3-D.
- Moving conductor problems in which the cross-section of the conductor normal to the velocity is invariant using the *Minkowski* transformation in both 2-D and 3-D.
- Non-linear permeability. Transient, DC or pseudo steady state using a complex number representation in 2-D and 3-D.
- Voltage or current forced wire wound coils. Can be connected to external circuit.

The *MEGA* program can solve time transient, DC and steady-state AC non-linear problems. All the schemes use the same solver module. A non-linear problem is solved by starting at the demagnetised state<sup>3</sup> and solving the problem for constant permeabilities [33]. Then, the next value of permeability is taken from the  $B(H)$  curve according to the solution results. The solver stops, when the magnetic flux density remains constant between non-linear iterations. The used value of change is 0.5 %. In addition, the residual<sup>4</sup> must reach a value of  $1 \cdot 10^{-4}$ .

In numerical calculations mainly two different error types appear. The first is the discretization error, which is due to replacement of the continuous problem by the discrete model [34]. This error is decreasing with a decreasing mesh size (smaller and more elements). The second error is called round-off error. It appears when the discrete equations are not solved exactly. Thus, it is present in iterative solutions since the iteration is only continued until no change takes place up to a certain number of digits [34]. This error will be small for increasing mesh sizes (bigger and fewer elements). This leads to the trouble, that decreasing the mesh

<sup>3</sup>Magnetic flux density and magnetic field intensity are zero.

<sup>4</sup>The residual is an internal parameter which takes care that the solving process does not go completely wrong.

size (refining the mesh) not necessarily increases the accuracy of the solution. For this reason care has to be taken with mesh sizes and furthermore, there is a strong need for comparing numerical solutions with measurements in order to validate their accuracy.

Forces derived from the numerical solution have been calculated integrating the *Maxwell* stress tensor over the surface of the secondary.

If a problem to be calculated is symmetric, then symmetric or periodic boundary conditions might be applied. This allows us to reduce the size of the mesh and thus makes the calculation faster and more stable.

Symmetric boundary conditions might be applied if the magnetic flux density is known to be directed normal to a surface or tangential to a surface. In all 3-D models presented in this thesis, only one half of the geometry is modeled. On the symmetry plane, the symmetric boundary condition is set to tangential flux.

Periodic boundary conditions might be applied if only a periodic part of a geometry is modeled like one pole instead of eight poles. For a linear machine, the use of periodic boundary conditions makes the program consider an infinitely long machine. Thus, longitudinal end effects are not taken into account and have to be investigated separately.

The periodic boundary conditions have to be assigned to nodes, which are called *master* and *slave* nodes. They have to be marked in the same order so that each slave node can be mapped correctly onto the corresponding master node. Furthermore, the phase difference between master and slave nodes has to be specified. If there is only one pole modeled, the phase difference has to be chosen to be 180 degrees. When two poles are modeled, the phase difference is zero. If the geometry allows us to model 2/3 of a pole, the phase difference will be 120 degrees. The phase differences of the periodic boundary conditions for the models presented in this thesis are shown in Table B.2 on page 131.

### 1.2.3 2-D Problems

The 2-D Cartesian problems in this thesis are calculated using the magnetic vector potential  $\vec{A}_m$ . The reason for choosing this approach is that currents in one conducting material are flowing in one direction perpendicularly to the considered 2-D plane, yielding two components of the flux density  $\vec{B}$  within the 2-D plane. In reality, the currents are not flowing in only one direction. At least, they have to change direction in the winding overhangs, which leads to the transversal end effects already mentioned. Nevertheless, it is possible to use the 2-D calculation to get a quick and rough insight. Moreover, the 2-D models can be used to estimate the longitudinal end effects, which cannot be taken into account with the 3-D models (due to hardware limitations).

The solution is carried out for a single component of the magnetic vector potential,  $\vec{A}_m = \vec{A}_{mz} = A_{mz}\vec{e}_z$ . The field quantities are derived from  $\vec{A}_m$ . The induced electric field is

$$\vec{E}_z = - \frac{\partial \vec{A}_{mz}}{\partial t} \quad (1.46)$$

and the magnetic flux density is

$$\vec{B} = \nabla \times \vec{A}_{mz}. \quad (1.47)$$

For velocity problems, the *Minkowski* transformation can be used [25, 32]. The electric field in the moving part can be regarded as having two components. The first part is the normal transformer effect due to the changing flux in the frame of reference (1.46). The second part is an electric field in the conductor frame of reference due to the motion, which gives the apparent electric field in the conductor frame of reference [31]

$$\vec{E} = - \frac{\partial \vec{A}_{mz}}{\partial t} + \vec{v} \times \vec{B}. \quad (1.48)$$

The equation to be solved is then

$$\nabla \times \frac{1}{\mu} \nabla \times \vec{A}_m + \kappa \frac{\partial \vec{A}_m}{\partial t} - \kappa \vec{v} \times \nabla \times \vec{A}_m = 0, \quad (1.49)$$

using (1.40) and  $\vec{J} = \kappa \vec{E}$ . Equation (1.49) can be reduced for 2-D Cartesian problems to

$$-\nabla \cdot \frac{1}{\mu} \nabla \vec{A}_{mz} + \kappa \frac{\partial \vec{A}_{mz}}{\partial t} - \kappa \vec{v} \times \nabla \times \vec{A}_{mz} = 0 \quad (1.50)$$

### 1.2.4 3-D Problems

The classical method of representing electromagnetic fields is using the magnetic vector potential  $\vec{A}_m$  and an electric scalar potential  $V$  [25, 31, 32]. Thus, (1.47) and (1.51) are used.

$$\vec{E} = - \frac{\partial \vec{A}_{mz}}{\partial t} - \nabla V \quad (1.51)$$

If the eddy current region of the problem has constant conductivity, the electric scalar potential can be set to zero and the field can be represented using the magnetic vector potential  $\vec{A}_m$ .

$$\nabla \times \frac{1}{\mu} \nabla \times \vec{A}_m + \kappa \left( \frac{\partial \vec{A}_m}{\partial t} \right) = 0 \quad (1.52)$$

For problems with materials with low conductivity or at very low frequency, convergence problems can appear, as the matrix tends towards a singular system<sup>5</sup> [31]. This problem can be overcome by introducing a penalty on the divergence of  $\vec{A}_m$ .

$$\nabla \times \frac{1}{\mu} \nabla \times \vec{A}_m - \left\{ \frac{1}{\mu_0} \nabla \nabla \cdot \vec{A}_m \right\} + \kappa \frac{\partial \vec{A}_m}{\partial t} = 0 \quad (1.53)$$

In order to fully gauge  $\vec{A}_m$ , the normal component of  $\vec{A}_m$  on the conductor surfaces should be set to zero.

For problems with moving conducting regions, the apparent electric field in the conductor frame of reference is

$$\vec{E} = - \frac{\partial \vec{A}_m}{\partial t} - \nabla V + \vec{v} \times \vec{B}. \quad (1.54)$$

The electric scalar can be substituted by  $V = \vec{A}_m \cdot \vec{v}$ .

Using  $\vec{v} \times \nabla \times \vec{A}_m = \nabla(\vec{A}_m \cdot \vec{v}) - (\vec{v} \cdot \nabla) \vec{A}_m$  gives the equation for solving moving conductor problems [31].

$$\nabla \times \frac{1}{\mu} \nabla \times \vec{A}_m + \kappa \left( \frac{\partial \vec{A}_m}{\partial t} + (\vec{v} \cdot \nabla) \vec{A}_m \right) = 0 \quad (1.55)$$

3-D models in *MEGA* are built in a very special way. First, there has to be the geometry modeled in 2-D. This 2-D model is then taken as the base plane for the 3-D model. The base plane is expanded in the  $z$ -direction to form a 3-D mesh. This is the only way to create a 3-D model. There is no possibility to have an element shape different from a rectangle in the third dimension. Therefore, the most complex geometry should be modeled in the base plane. Figure 1.11 shows a 3-D model with its base plane and a cut view showing the third dimension.

<sup>5</sup>A system of equations is singular, if the determinant of the system matrix equals zero [35].



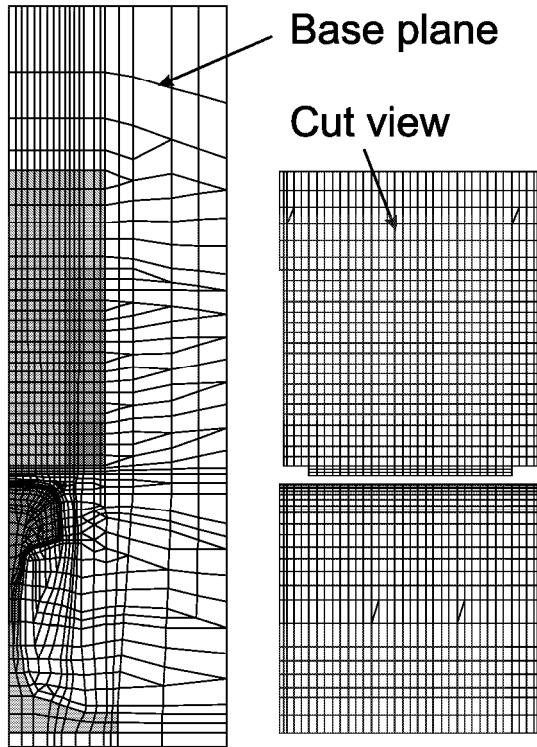


Figure 1.11: Base plane and cut view on the symmetry plane of model L3PF $\delta$ 6M. In the cut view, the air is neglected.

### 1.2.5 Difference of 2-D and 3-D calculations

The general difference between 2-D and 3-D is shown in Figure 1.12 on the example of eddy currents in the secondary.

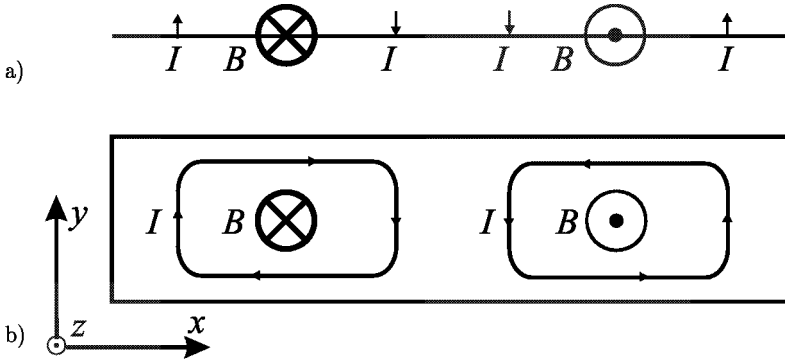


Figure 1.12: Scheme of the eddy current distribution in a) 2-D and b) 3-D models. The eddy currents  $I$  (indicated by arrows) could perform a whole loop in the 3-D model, whereas they will curl in the 2-D model in the infinity. The flux density is assumed to point into the surface with a cross and to point out of the surface with a dot.

Looking from above onto the surface of the secondary, the eddy currents will be considered in the calculation as expressed by vectors. The exciting flux density is indicated by a cross as pointing into the surface and by a dot as pointing out of the surface. Assuming the same induced voltage in the secondary, the eddy currents in the 2-D models will be stronger than those of the 3-D models. This is due to the larger ohmic resistance of the secondary for the 3-D models. Here, the eddy currents have to curl around the inducing flux, whereas they are simply perpendicular to the 2-D plane in the 2-D models.

## Chapter 2

# Initial considerations for the linear machine design

### 2.1 Definition of design constraints for linear machines in the railway system

The German railway system is a huge network of railway tracks with a great variety of electromagnetic devices (such as the inductive electromagnetic security device *INDUSI* and axle counting devices) near or at the track. The track runs over standard ground, over bridges, through tunnels and even goes up and down on slopes over mountains. Each part of the railway system is standardized to obtain uniform components throughout the country. Railway tracks are classified as suitable for low speed, high speed, planar, slope, etc. Thus, for every type of railway track and for every single type of train, the geometrical dimensions of the track, the train and all the periphery are determined as minimum and maximum values. These regulations are given by the "Eisenbahnbundesamt" (EBA) and collected in the "Eisenbahn- Bau- und Betriebsordnung" (EBO)[36].

If a new device has to be integrated into the railway system, the first task is to figure out the design constraints, meaning the available space at the supposed place, the temperature and mechanical limits.

For the design of the linear induction machine, the following regulations and limitations have to be abided:

- Standards and regulations of the *EBO* and the *UIC* (Union International des Chemins de fer)[37]
- EMC (electro magnetic compatibility) regulations by EN 50121 Part 1-5 [38]
- Interference current limit by the *EBA* [39]
- Maximum rail temperature of 70°C on bridges and 100°C on other places. The time interval between the passing of two trains has to be considered, if eddy currents will heat up the rail.
- The maximum transient mechanical peak acceleration is 50 *g*.

- The braking power of the linear induction machine should be similar to the braking power obtained by the eddy current brake. Thus, the eddy current brake might be replaced.
- The input power has to be feasible for the locomotive "BR152" (for details see Appendix D).
- The geometric conditions have to be chosen according to the *EBO* and *UIC*.

The following items are desirable:

- The normal force for the operating modes "braking" and "accelerating" has to be minimized<sup>1</sup>.
- The normal force should be used to compensate aerodynamical effects.
- As far as possible, the brake should be regenerative.

The standards and regulations of the *EBO* and the *UIC* will be considered in the following chapters. The interference current limits are depending on the frequency of the interference current and its duration. The rail temperature is mainly depending on the eddy currents induced in the rail. This will be considered in chapter 4.5. The transient peak load has to be abided in the mechanical design. After finishing the electrical design, a mechanical strength investigation should follow. Since a prototype of the machine has not been built, the mechanical strength investigation has not been done here. The obtainable forces are part of the Finite Element calculation and will be discussed in detail in the corresponding chapters.

The rail itself as the mechanically essential and electrically supporting part of the track is shown in Figure 2.1 [40].

For different railway applications, different rail profiles are available. The German railway company uses the rail profile *UIC60* for the tracks with high loads and high speed trains. Some examples for other profiles are *S41* and *S49* for trams and subways and *S64* for tunnels and surface mining [41]. The difference between the profiles mainly lies in the geometrical dimensions, but also in the chemical composition. Depending on the application, different percentages of the particular elements (Carbon, Manganese, Silicon, Chromium, Phosphorus and Sulfur) are used (see Appendix A).

<sup>1</sup>This is desired mainly for the region around railway stations. There could be a mechanical damage to the track when moving parts are attracted and removed by the linear machine.

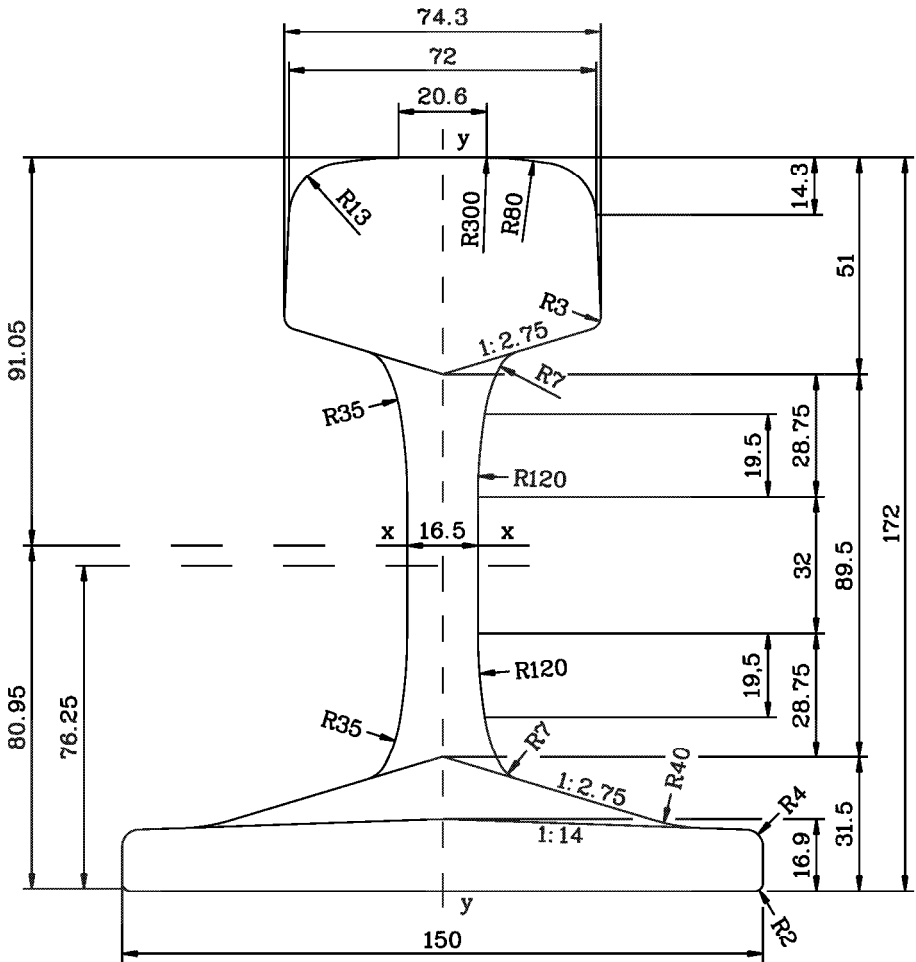


Figure 2.1: Rail profile *UIC60* with main dimensions given in mm [40].

## 2.2 Feasibility of different kinds of linear machines in railway applications

There are many ways of mounting a linear machine in the railway system. Some of them were already documented [13]. The common way of integrating a linear machine in rail cars is mounting it on the undercarriage. Figure 2.2 displays four different methods.

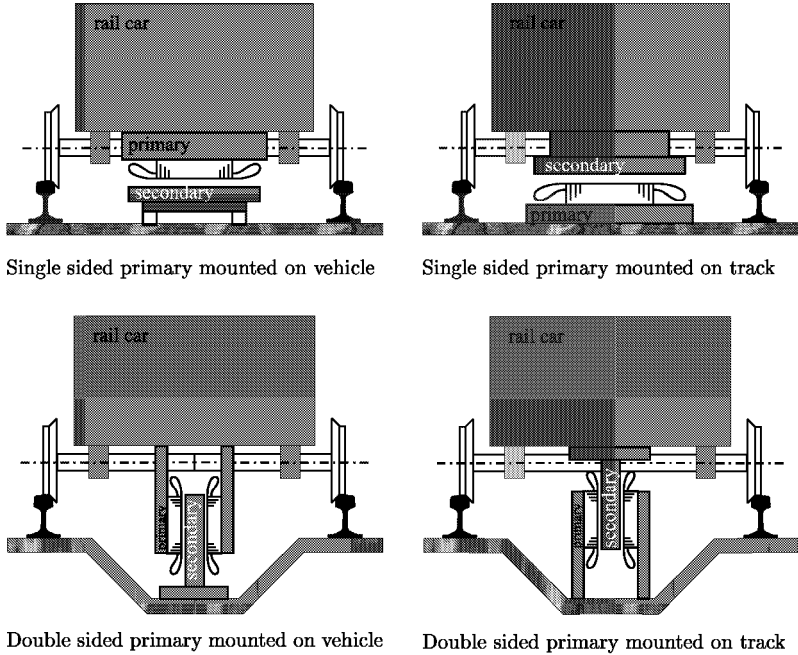


Figure 2.2: Different methods of mounting linear machines on rail cars [13]. The yoke of the primary part is colored in light grey. The secondary part is colored in dark grey. The primary iron is supposed to be laminated and the end turns are shown on both sides of the primary iron.

Basically, the primary can be mounted on the undercarriage as well as on the rail track, and the primary can be single or double sided. All possibilities have their advantages and disadvantages. The main aspects of the different approaches are collected in Table 2.1.

Comparing the features of the possibilities already mentioned of linear machines in railway applications with the constraints listed in chapter 2.1, they are not in agreement. The problem mainly lies in the geometric boundary conditions of the German railways. Generally, it is hardly possible to mount any additional device in the railway track. Therefore, a solution

Table 2.1: Main aspects of different linear machine configurations.

<b>Configuration:</b>	<b>Features:</b>
Single sided primary mounted on the car	Short primary, excitation on rail car, asymmetrical air gap possible
Single sided primary mounted on the track	Short secondary, excitation along the whole track, asymmetrical air gap possible
Double sided primary mounted on the car	Higher force generation than single sided approach, excitation on rail car, much space needed in vertical direction
Double sided primary mounted on the track	Higher force generation than single sided approach, excitation along the whole track, much space needed in vertical direction

has to be found, which is in agreement with all the given conditions. The installation of an additional primary or secondary in the middle of the track is very expensive. The advantages of a linear machine in this place do not offset the high costs. Therefore, this is not an economical solution.

The simplest method is to mount the primary in the rail car and to use the rail itself as secondary. Of course, the shape of the rail together with its material would not be the first choice for developing a new electric machine, but it fulfills all the requirements and will therefore be the approach to be discussed further in this thesis.

## 2.3 Determination of maximum available space for the linear machine

In order to make sure that the linear machine will operate with an air gap as constant as possible, the wheel-set in the bogie was chosen to be the most suitable place for mounting it. Contrary to the body of the rail car, the wheel-set belongs to the non-suspended mass. Therefore it will keep a steady position to the rail most of the time. Thus, the linear machine will be mounted on the bogie between the wheels above the rail. This is the same principle of mounting as already realized with the eddy current brake for the *ICE 3* [2] (see Figure 2.3).

Figure 2.4 shows a cut view of the railway track with the rail, the wheel and the guard-rail. The guard rail takes care of the tracking of the wheel at track junctions. The wheel itself is shown with its maximum displacement on the rail. The vertical movement of the wheel will be approximately 1.5 mm [43]. In order to avoid mechanical contact between the linear machine and devices on the track, the possible width is small. The marked region shows the space available on the bogie. The geometrical values of a rectangular box fitting in the available space are given in Table 2.2.

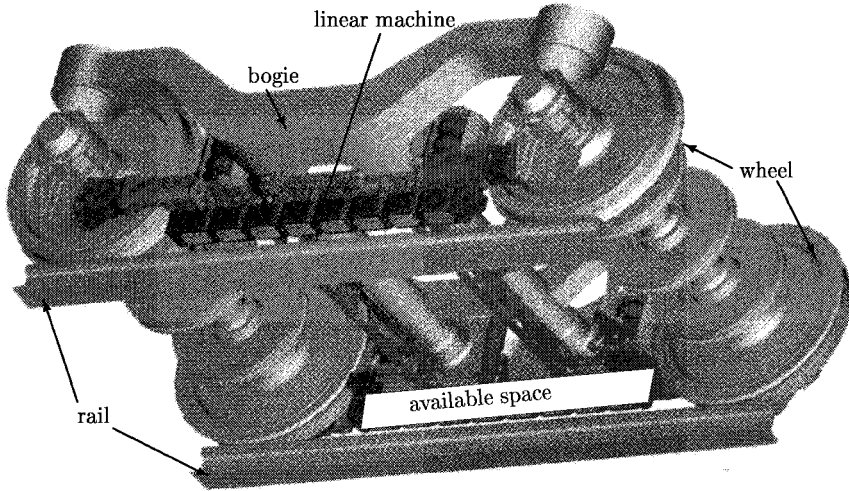


Figure 2.3: Principle of mounting the linear machine on the bogie [42]. The linear machine is mounted beneath the wheels above the rail. On the rear part of the bogie, the available space is marked. The bogie belongs to the German high speed train *ICE 3*. The latest linear eddy current brake, shown in this figure, could be substituted by the linear induction machine

Table 2.2: Maximum geometrical sizes available for mounting the linear machine.

length	width	height
1413 mm	135 mm	250 mm



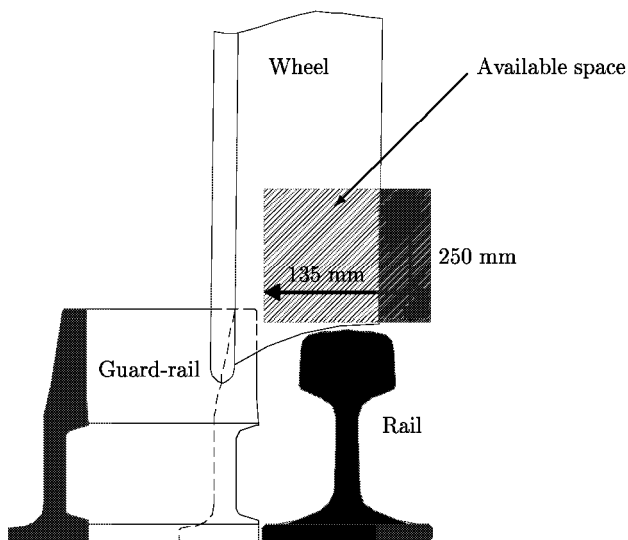


Figure 2.4: Cut view through the railway track with marked occupied and free space. The guard rail is shown in a view of all possible distances to the rail. The wheel is shown in its maximum displacement in the direction of the guard rail.

# Chapter 3

## Numerical calculation of the linear eddy current brake

### 3.1 Introduction

The linear eddy current brake is a device which has already been built, tested and put into operation in the German high-speed train *ICE 3*. One very early prototype of this machine has been available for measurements at our department. Furthermore, there was published data from former measurements available [2]. This has been a good prerequisite for starting a new design: First investigating an existing prototype of a linear eddy current brake and then use the validated procedures for the new design of a linear induction machine.

The measurements will be compared with the results from Finite Element (FE) calculations to verify the numerical models.

#### 3.1.1 Geometrical considerations

The geometry of the eddy current brake is shown in Figure 3.1.

Six poles, forming the primary are excited by DC-current yielding a stationary magnetic field in the air gap  $\delta$  between primary and rail. Different models have been considered to calculate the eddy current brake for different train velocities  $v$ , taking the non-linear material property  $B(H)$  of the iron parts (primary, rail) into account. The holes in the primary part of the eddy current brake, which are essential to connect the coils, but reduce the cross section of the iron back, are not considered in the FE models.

#### 3.1.2 Finite Element modeling

Two different  $B(H)$ -curves have been considered, based on [11] and are shown in Figure 3.2.

The shown magnetization curves are measured by the manufacturing company for a rail profile *S49*. Since no other measurements have been available, this curve has been used for the computation.

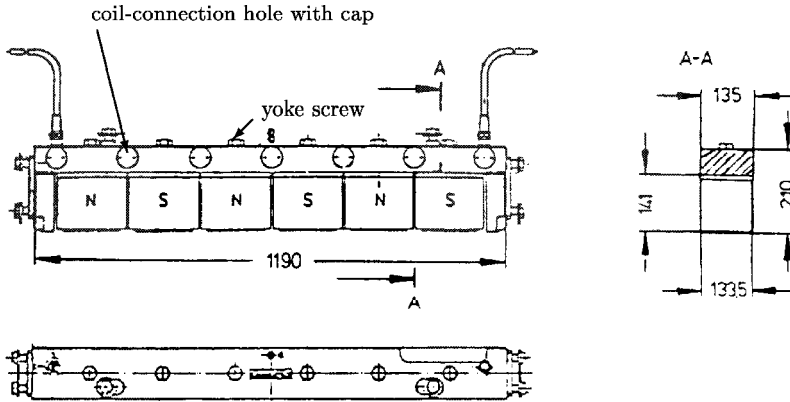


Figure 3.1: Geometrical dimensions of the eddy current brake [2]. The poles are fixed individually on the yoke by a screw which can be seen on top of the poles at the yoke. The coils are connected with screwed clips, which are hidden behind the circular caps on the yoke.

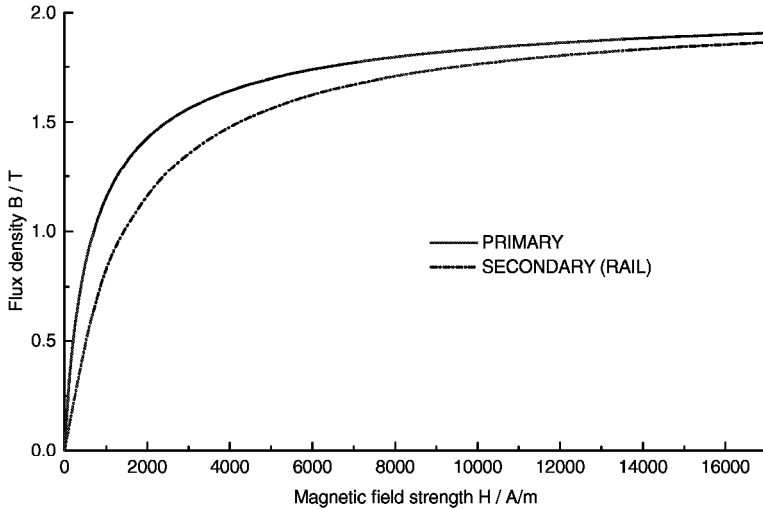


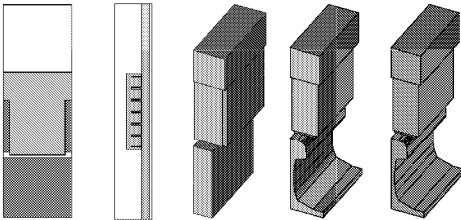
Figure 3.2:  $B(H)$ -curves of the primary part of the eddy current brake and the rail. The primary part of the eddy current brake is made of steel *St 37*, whereas the rail iron is made of a material composition according to the profile *S 49* [11].

The rail dimensions and the conductivity (see chapter 4.6.2) are taken for the profile *UIC60* (see Figure 2.1), because it is used by the German railways for the investigated application<sup>1</sup>.

For the convergence of the FE-models it is necessary to obtain the second derivative of the  $B(H)$ -curve steady for every point of the curve. This has been achieved by using an implemented tool of the FE program *MEGA*. This tool uses a spline fit on the data points and produces warning messages if the curve has any negative slopes.

The computational approach of the eddy current brake has been performed in four steps. First, two kinds of two-dimensional models have been created<sup>2</sup>. One model (E2P) has been built with one pole and periodic boundary conditions, the other one (E2E) with six poles and a long rail allowing longitudinal end effects. Then two kinds of three-dimensional models were set up with different rail shapes. The first rail shape (E3PR) was rectangular to facilitate the model generation and the solving process. The second rail shape (E3P, E3P $\kappa$ 2.5) was chosen according to the dimensions of the *UIC60* profile. The main features of these models are collected in Table 3.1.

Table 3.1: Main features of the different Finite Element models for computation of the eddy current brake.



Model	E2P	E2E	E3PR	E3P	E3P $\kappa$ 2.5
Considered dimensions	2	2	3	3	3
Longitudinal end effects	no	yes	no	no	no
Transversal end effects	no	no	yes	yes	yes
Rail shape	no	no	no	yes	yes
Number of elements	1144	12411	33600	45680	45680
Air gap height	6.5 mm	6.5 mm	6.5 mm	6.5 mm	6.5 mm
Ampere-turns per slot	67 kA	67 kA	67 kA	67 kA	67 kA
Rail conductivity / S/m	$5 \cdot 10^6$	$5 \cdot 10^6$	$5 \cdot 10^6$	$5 \cdot 10^6$	$2.5 \cdot 10^6$

For the models E2P, E2E and E3PR, the rail is considered to have a rectangular shape.

<sup>1</sup>The chemical composition of *S49* and *UIC60* are shown in Appendix A Table A.1.

<sup>2</sup>A complete survey of all created models with their main features and their nomenclature is given in Appendix B Table B.2

Model E3P is built with the correct rail shape. It has not been possible to build a model of the complete machine with a suitable rail length to include all induced eddy currents. This case would increase the number of elements over 200 000, which is the hardware limit. Therefore, it has not been possible to consider the complete brake geometry including longitudinal end effects. These effects are calculated only with 2-D models, where the transversal end effects are neglected. By comparing the results of the different models, a correction of the 3-D results for considering longitudinal end effects can be obtained (see chapter 3.2 ).

The forces calculated with model E2P and E2E are referred to a width of the primary of 80 mm (which is about the width of the rail). The air gap of model E2P, E2E and E3PR has a constant value of 6.5 mm. Model E3P was created with the original rail shape and therefore the air gap is not constant in  $z$ -direction. The air gap of the model equals 6.5 mm at the symmetry plane. In [44], it is proposed to introduce an equivalent air gap for the 2-D models. This equivalent air gap takes into account the flux density distribution along the rail shape, integrating over the different air gap heights. Furthermore, in [45] it is proposed to use the *Russell and Norsworthy*<sup>3</sup> factor [46] to take into account the finite width of the secondary by reducing the conductivity. Both proposals have not been applied to the 2-D models, since they are not designed to calculate the real behavior of the linear machine, but to estimate the end effects.

According to the published measurement [2], for all the calculations a number of ampere-turns per slot equal to 67 kA was applied.

## 3.2 Evaluation of longitudinal end effects by two-dimensional calculations

Throughout the recent literature, it is hardly possible to find publications with the estimation of longitudinal end effects in linear eddy current brakes. Some researchers omit the end effects [47, 48], and some have proposed to evaluate the influence of longitudinal end effects by two-dimensional calculations [10, 49]. It has been suggested to use the end effect factors of linear induction machines with zero frequency as an approximate representation [45]. As already pointed out, the longitudinal end effects could not be included in the 3-D models because of hardware limitations. This leads to the decision of evaluating the longitudinal end effects with the two-dimensional models. It can be done by comparing two-dimensional models with different boundary conditions.

<sup>3</sup>*Russell and Norsworthy* give in their paper analytically calculated expressions for the current-density distribution in screened-rotor induction motors with a thin cylindrical conducting shell situated in the air gap of the motor. These equations are valid for the central (inner) region as well as the overhang region of a conducting shell.

The first type of model was built with only one tooth and anti-periodic boundary conditions (see Figure 3.3a, model E2P). These boundary conditions let the program assume that the length of the model would be infinite with alternating poles. Thus, Model E2P does not take into account any end effects.

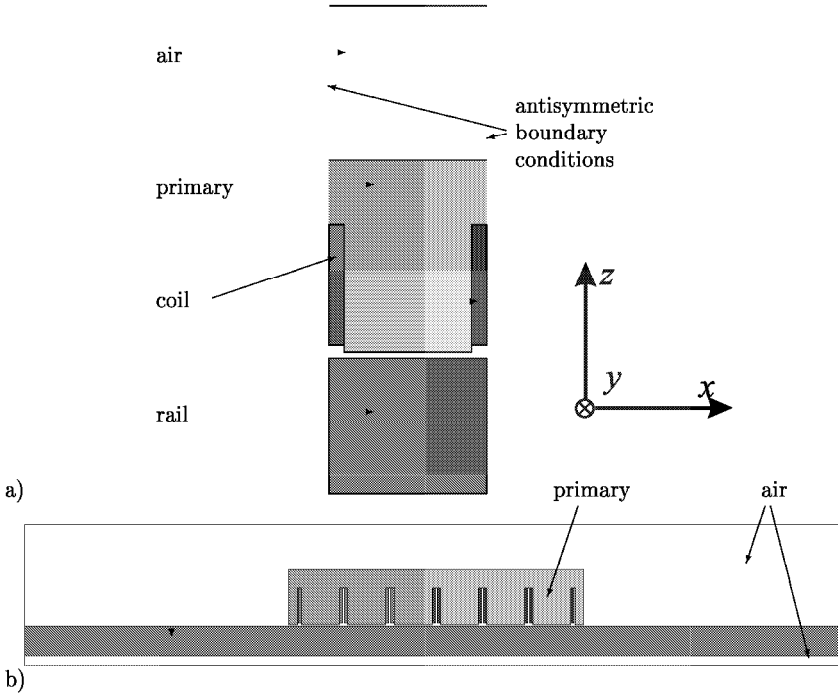


Figure 3.3: Two-dimensional models of the eddy current brake. a) Model E2P with periodic boundary conditions, b) Model E2E with six poles and longitudinal end effects. A plot of the flux lines for model E2E is shown in Figure 1.2 on page 7.

The second type was modeled with the complete geometry, containing the end poles (see Figure 3.3b, model E2E). It takes into account the longitudinal end effects, but transversal end effects are not considered. The rail is modeled long enough to bear the eddy currents of the longitudinal end effects. By comparing the results of both models, the influence of the longitudinal end effects could be separated.

The 2-D problem is solved with the magnetic vector potential formulation. As boundary condition, the magnetic vector potential  $A_m$  is set to zero at the model boundaries. In case of applied velocity  $v$ , the rail is moved relatively to the primary into the positive  $x$ -direction, which has the same effect as moving the primary into the negative  $x$ -direction.

### 3.2.1 Influence of longitudinal end effects on force generation

In order to evaluate the influence of longitudinal end effects, the calculated forces of the two models have been compared. Furthermore, investigations have been made focusing on the distribution of the flux density along the linear machine [44].

The force curves of model E2P and E2E are shown in Figure 3.4 and Figure 3.5. The geometric parameters are chosen according to Figure 3.1. The excitation was chosen according to [2] with a number of ampere-turns per slot of 67 kA. The conductivity of the rail was chosen as  $\kappa_{rail} = 5 \cdot 10^6$  S/m, whereas the primary part is considered to have zero conductivity (although the primary iron is not laminated) because of the DC excitation.

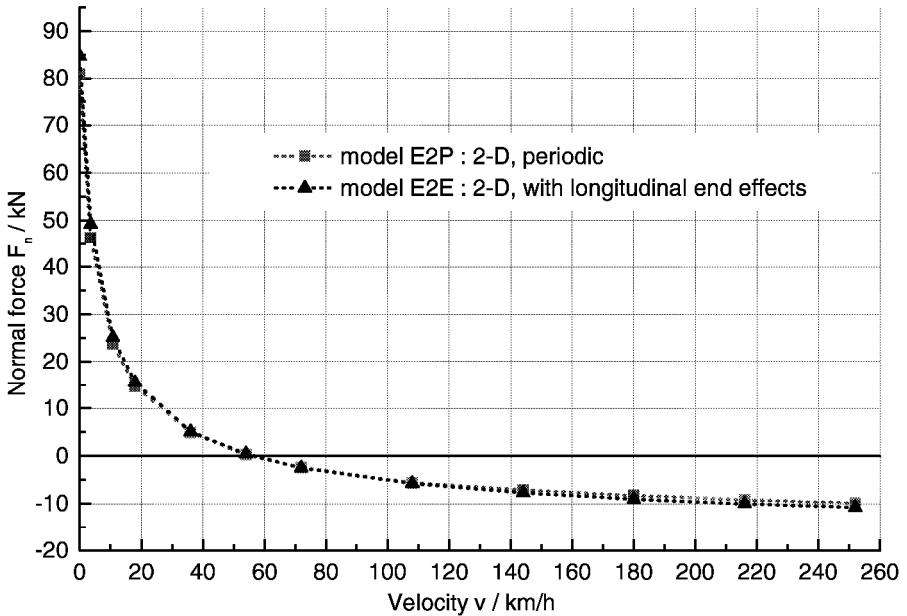


Figure 3.4: Normal force obtained from the two-dimensional models E2P and E2E. Positive values are attracting, negative are levitation forces.  $A \cdot J = 69250$  A/cm  $\cdot$  A/mm<sup>2</sup>

The normal force starts with a high value at standstill and then decreases very rapidly with increasing velocity of the primary part. It is remarkable, that the 2-D results present a levitation force at velocities higher than 50 km/h due to the strong interaction of eddy currents and the air gap field. Therefore also the braking forces are calculated too high with model E2P and E2E. The phenomenon of levitation is investigated in detail below.

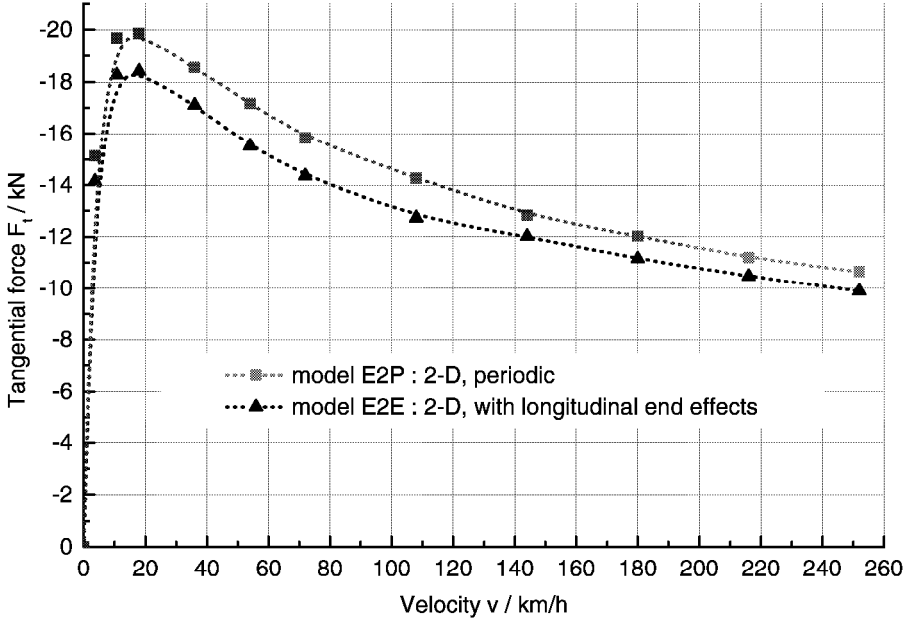


Figure 3.5: Tangential force obtained from the two-dimensional models E2P and E2E. Negative values imply braking forces.  $A \cdot J = 69250 \text{ A/cm} \cdot \text{A/mm}^2$

Due to the zero frequency of the primary excitation, the eddy current brake can only obtain braking tangential forces. It has to be pointed out that the extremely high braking forces at low velocities are an effect of the two-dimensional calculation.

### 3.2.2 Flux density characteristics

Since the attractive force depends on the difference of the flux density squares (see (1.37)), it is useful to take a look at those flux densities. Figure 3.6 shows the normal component of the flux density ( $B_n$ ) in the middle of the air gap along two poles of model E2P $\mu 1.5$  (equal to model E2P, only with constant permeability) at  $v = 18 \text{ km/h}$  and  $v = 144 \text{ km/h}$  with an excitation of  $67 \text{ kA}$  ampere-turns per slot. The longitudinal component ( $B_l$ ) is shown in Figure 3.7. For this comparison, the relative permeability of the rail is considered constant at a low saturated value of  $\mu_r = 1.5$ .



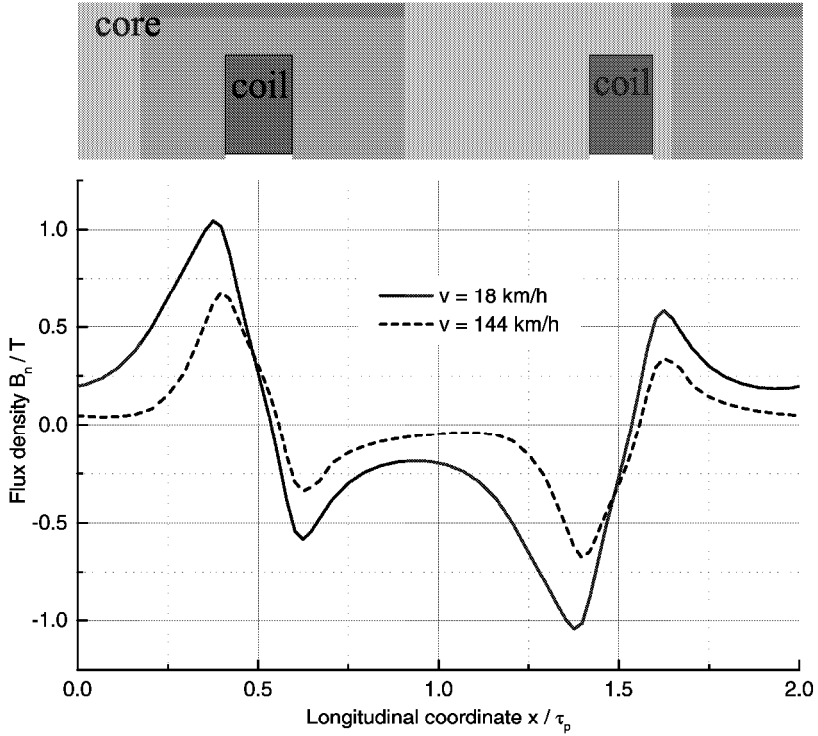


Figure 3.6: Normal component of flux density  $B_n$  of model E2P $\mu$ 1.5 along two poles on the secondary surface for different velocities.  $A \cdot J = 69250$  A/cm  $\cdot$  A/mm<sup>2</sup>

With increasing velocity, the longitudinal component of the flux density increases, whereas the normal component decreases. According to (1.37), this leads to a polarity reversal of the attractive force, which can be observed in Figure 3.4 for the 2-D models.

In Figure 3.8, the flux lines are shown for model E2P $\mu$ 1.5 at  $v = 18$  km/h and  $v = 144$  km/h.

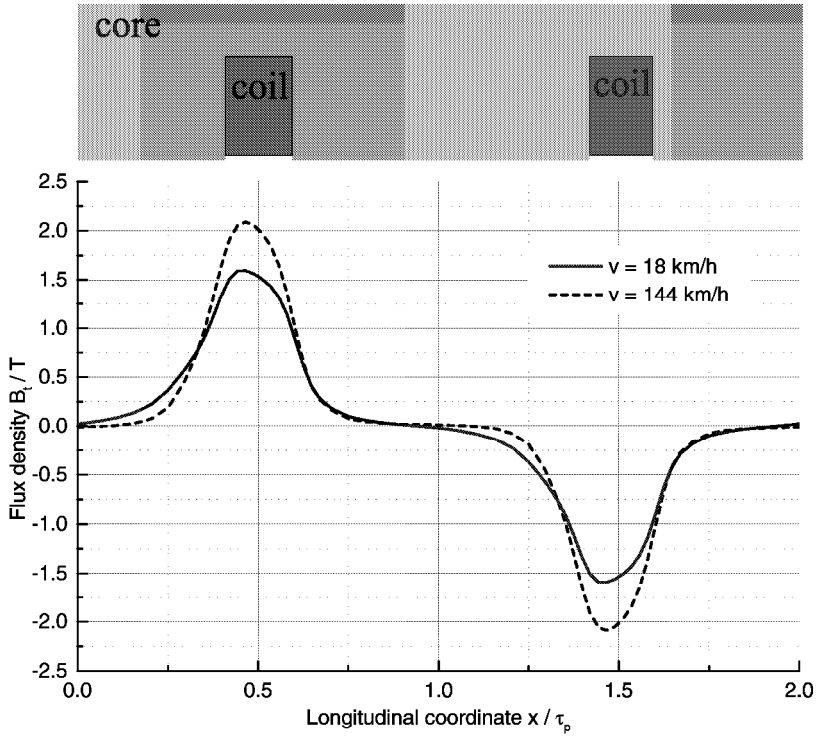


Figure 3.7: Longitudinal component of flux density  $B_t$  of model E2P $\mu$ 1.5 along two poles on the secondary surface for different velocities.  $A \cdot J = 69250$  A/cm  $\cdot$  A/mm<sup>2</sup>

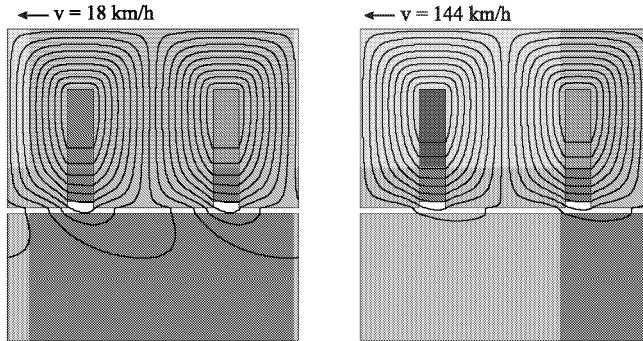


Figure 3.8: Flux lines of model E2P $\mu$ 1.5 for two poles at  $v = 18$  km/h and  $v = 144$  km/h.

### 3.2.3 Longitudinal end effect factor

The longitudinal end effect can be separated by figuring out the percentage of difference between the two force characteristics of model E2P and E2E (see Figure 3.4 and 3.5). The percentage of difference is shown in Figure 3.9 depending on the velocity of the primary. The end effect factor for the tangential force component  $k_{FtE}$  is calculated using (3.1) and the end effect factor for the normal force component  $k_{FnE}$  using (3.2).

$$k_{FtE} = \frac{F_{tEE}}{F_{tPE}} \quad (3.1)$$

$$k_{FnE} = \frac{F_{nEE}}{F_{nPE}} \quad (3.2)$$

$F_{tEE}$  is the tangential force component of model E2E,  $F_{tPE}$  the tangential force component of model E2P,  $F_{nEE}$  the normal force component of model E2E and  $F_{nPE}$  is the normal force component of model E2P.

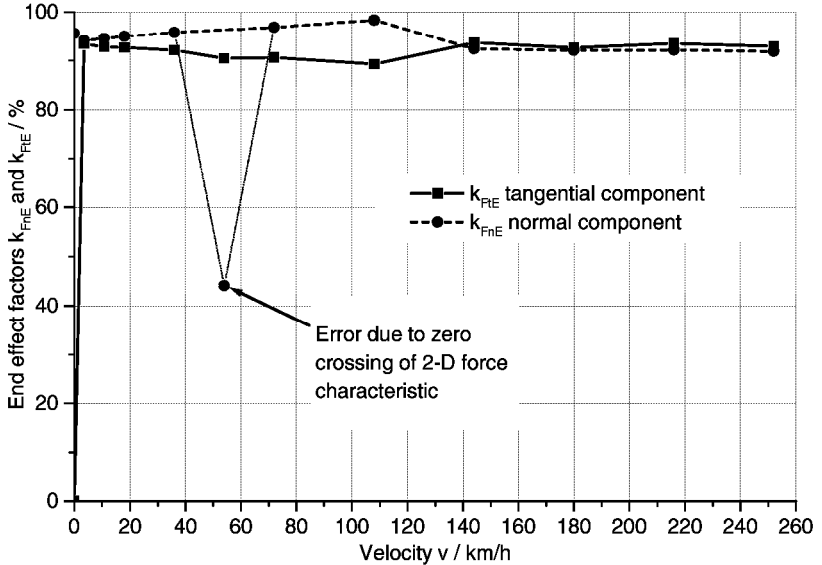


Figure 3.9: Longitudinal end effect factors of the linear eddy current brake on normal and tangential forces. Mean values are 92% for  $k_{FtE}$  and 95% for  $k_{FnE}$ .

The normal component of the end effect factor shows an exposed point at 54 km/h. This is due to the forces being near to zero and thus leading to a higher relative difference between

model E2P and model E2E. This extreme point has been neglected and fitted to the general behaviour shown in Figure 3.9. The influence of the longitudinal end effect differs for low velocities up to 10 % between normal and tangential direction. For velocities higher than 140 km/h it is nearly the same for both directions.

### 3.3 Numerical 3-D calculation of an eddy current brake

#### 3.3.1 Three-dimensional modeling

Models E3PR and E3P (see Figure 3.10) for three-dimensional field calculation are solved with the magnetic scalar potential formulation for non-conducting regions (primary) and the magnetic vector potential formulation for eddy current regions (rail). The 3-D model E3PR is based on the 2-D model E2P. A region of air is surrounding the solid parts. The magnetic scalar potential  $V$  is set to zero at the outside air boundaries.

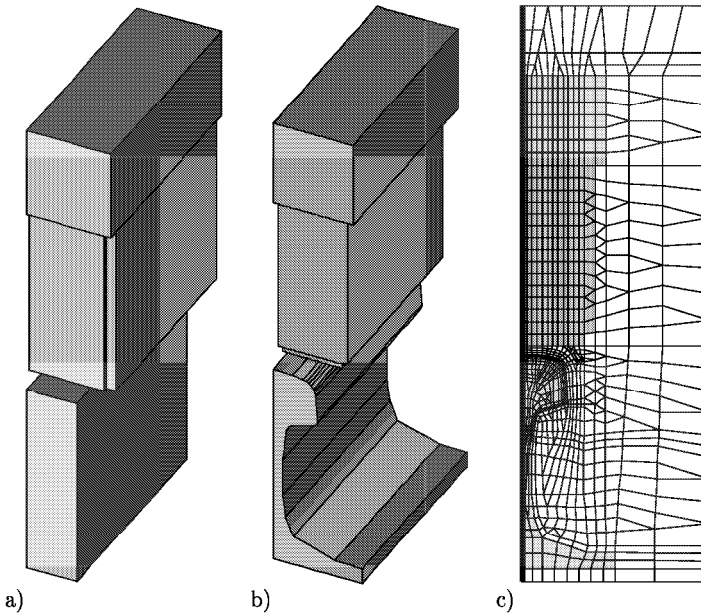


Figure 3.10: Three-dimensional models. a) model E3PR with rectangular rail, b) model E3P with correct rail shape, c) mesh of model E3P.

In order to reduce the solving time and to increase the probability of convergence, the models consist only of one magnetic pole with anti-periodic boundaries on both sides. Since the eddy current brake is centered over the rail, it is possible to model only one half of the pole and to apply tangential flux boundary conditions on the symmetry plane. These models do not consider the longitudinal end effects, but they can show the influence of the transversal end effects including longitudinal eddy currents.

The solving process of the 3-D model with moving parts and non-linear material properties tends to lose stability, especially at high velocities. In order to regain stability, a solution at lower speed  $v$  is used as an initial vector for higher speeds [50]. The mesh has to be adequately fine near the surface of the moving rail. The element height should be less than one third of the penetration depth  $\delta_p$  which can be calculated using (3.3).

$$\delta_p = \sqrt{\frac{1}{\pi \frac{v}{2\tau_p} \mu \kappa}} \quad (3.3)$$

Model E3P takes into account the real shape of the rail. Due to the round shape, the base plane mesh consists of quadrilateral and triangular elements. The difference in shape and size slows down the solving process and complicates the convergence. In order to make the solution unique, the normal component of the vector potential  $A_m$  has been set to zero on  $A_m\psi$  interfaces<sup>4</sup> according to [51]. This ensures, that the system is well conditioned.

### 3.3.2 Results of force calculation

The results of the force calculation of model E3PR and E3P are shown in Figure 3.11. The applied geometrical and electrical parameters are equal to those, which have been used for the two-dimensional calculations (see Table B.2).

The normal forces obtained from the 3-D models are almost coincident. The values are positive for all velocities. The braking forces are obviously depending on the shape of the secondary. Using a rectangular shaped secondary leads to higher forces than those obtained from the rail shape. It can be explained by looking at the eddy currents and the flux in the air gap, which will be done in the following sections.

<sup>4</sup>An  $A_m\psi$  interface is an interface between a region modeled with  $A_m$  and a region modeled with  $\psi$ . By default, in *MEGA* a conductor region is modeled with  $A_m$  and a nonconductor region with  $\psi$ . However, a nonconductor region can also be modeled with  $A_m$ .

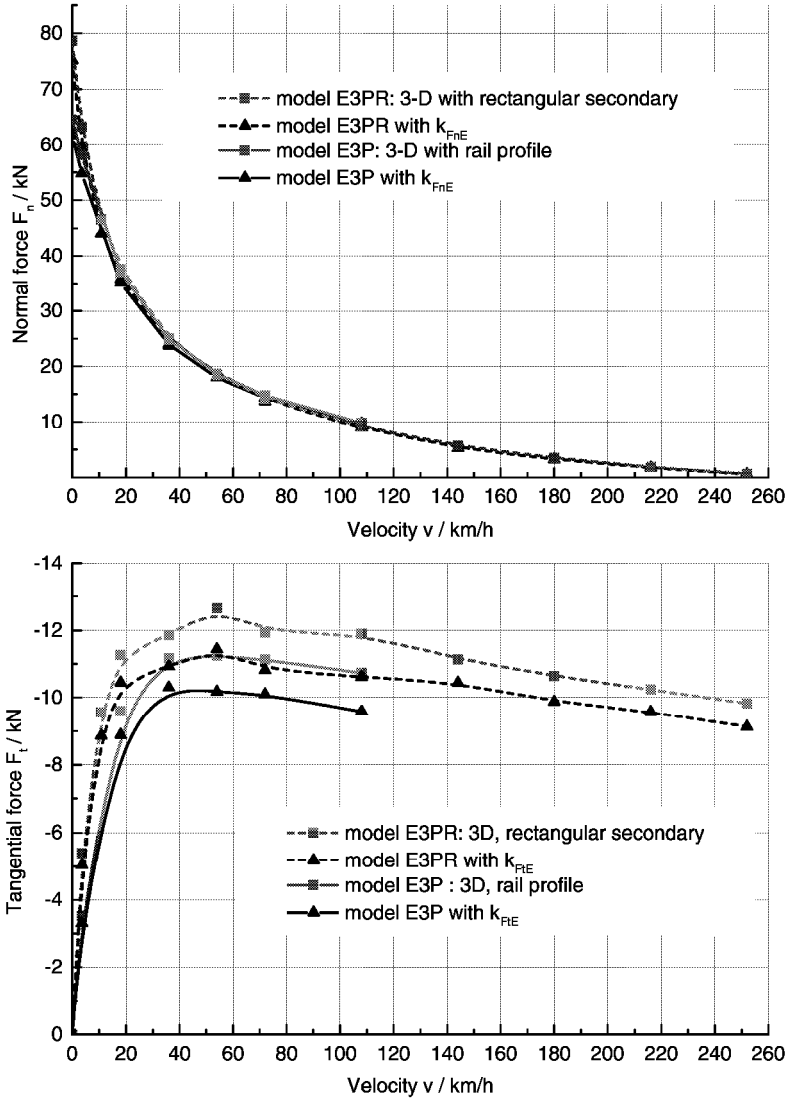


Figure 3.11: Normal (attractive) and tangential force obtained by 3-D calculation of the eddy current brake. Both curves of the normal force are almost coincident. Model E3P has convergence problems for velocities higher than 108 km/h. Therefore, results for higher velocities do not exist. Both force characteristics are plotted without and with applied longitudinal and tangential end effect factor ( $k_{FnE}$  and  $k_{PtE}$ ).  $A \cdot J = 69250 \text{ A/cm} \cdot \text{A/mm}^2$

### 3.3.3 Flux density and eddy current distribution

The normal component of flux density along the  $y$ -axis (width of the machine) is shown in Figure 3.12. Here, the two models E3PR and E3P are compared. One can see, that the curve from model E3P has a lower mean value of normal flux density than model E3PR due to the rail shape of the secondary.

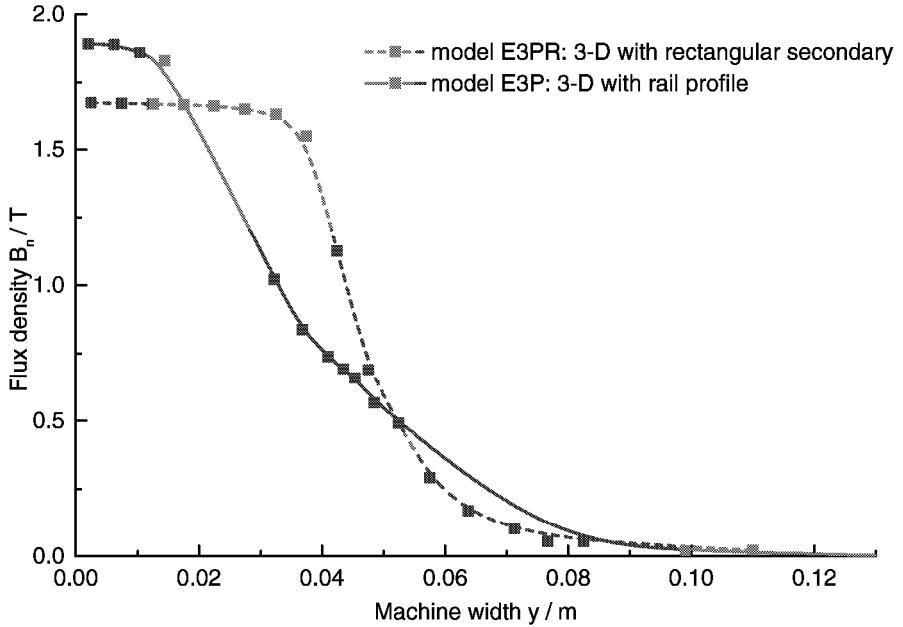


Figure 3.12: Normal component of flux density  $B_n$  of model E3PR and E3P along the  $y$ -axis on the secondary surface.  $A \cdot J = 69250 \text{ A/cm} \cdot \text{A/mm}^2$

For illustrating this effect, the same comparison is made for a vector plot of the flux density at the middle of a tooth in the  $y$ - $z$ -plane shown in Figure 3.13.

Contrary to the two-dimensional models, the normal component of the flux density in the air gap is bigger than the tangential component (see Figure 3.14). This is due to the transversal end effects.

Figure 3.14 shows the distribution of flux density in the symmetry plane of the secondary surface at the air gap of model E3PR and E3P at a velocity of 18 km/h and 108 km/h. Since the tangential force component can be calculated using (3.4), model E3PR obtains higher tangential forces than model E3P due to the higher tangential component of the flux density.

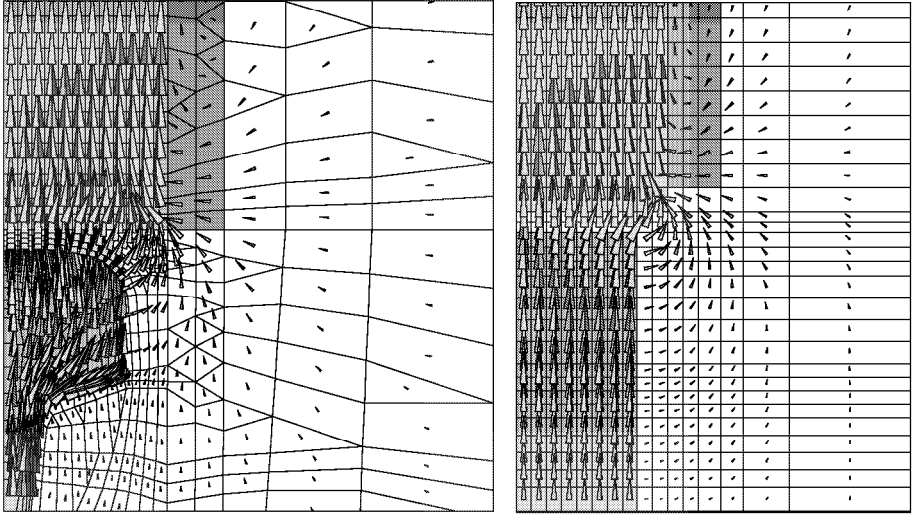


Figure 3.13: Vector plot of flux density  $B$  of model E3P and E3PR for the  $y$ - $z$ -plane at the middle of a tooth.  $A \cdot J = 69250 \text{ A/cm} \cdot \text{A/mm}^2$

$$F_t = \int \frac{B_n \cdot B_t}{\mu_0} dA \quad (3.4)$$

The eddy current distribution in the cut through the secondary of model E3P is drawn for a velocity of 3.6 km/h and 36 km/h in Figure 3.15. The influence of the velocity can easily be seen at the distortion of the current-density in the rail. The higher the velocity between primary and secondary, the bigger the distortion will be. The primary part does not contain any eddy currents. This is due to the DC excitation.



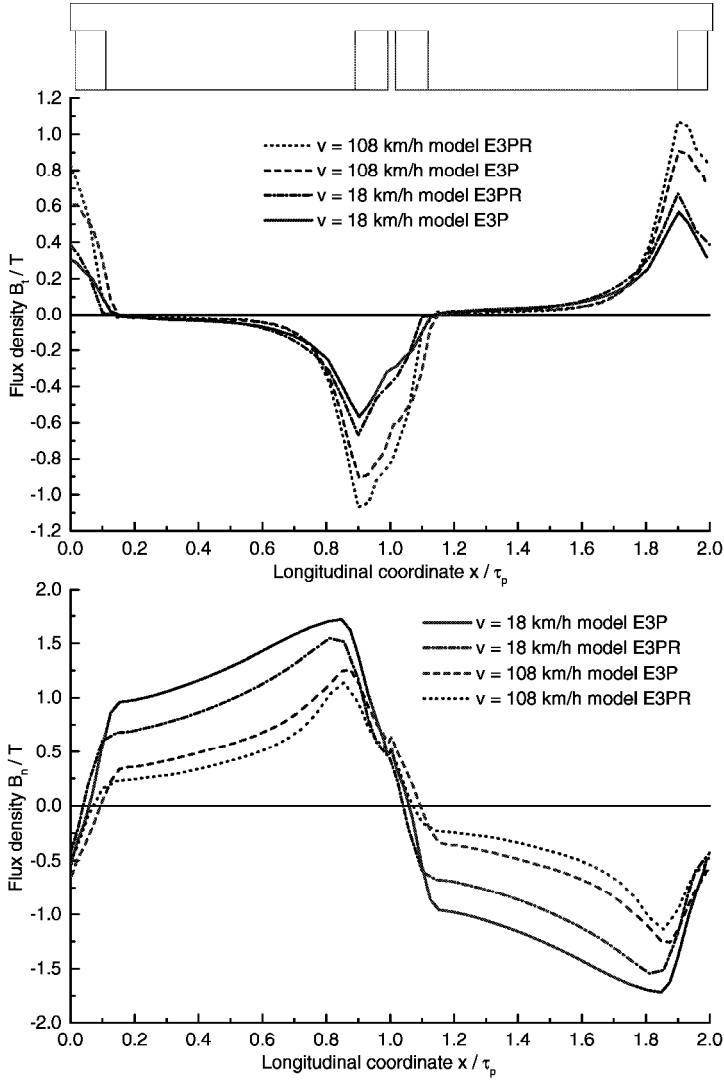


Figure 3.14: Longitudinal and normal component of flux density of model E3PR and E3P along two poles on the secondary surface for different velocities. For the longitudinal component, model E3P obtains lower flux density values than model E3PR. The flux density decreases with decreasing velocity. For the normal component, model E3PR obtains lower flux density values than model E3P. The flux density decreases with increasing velocity.

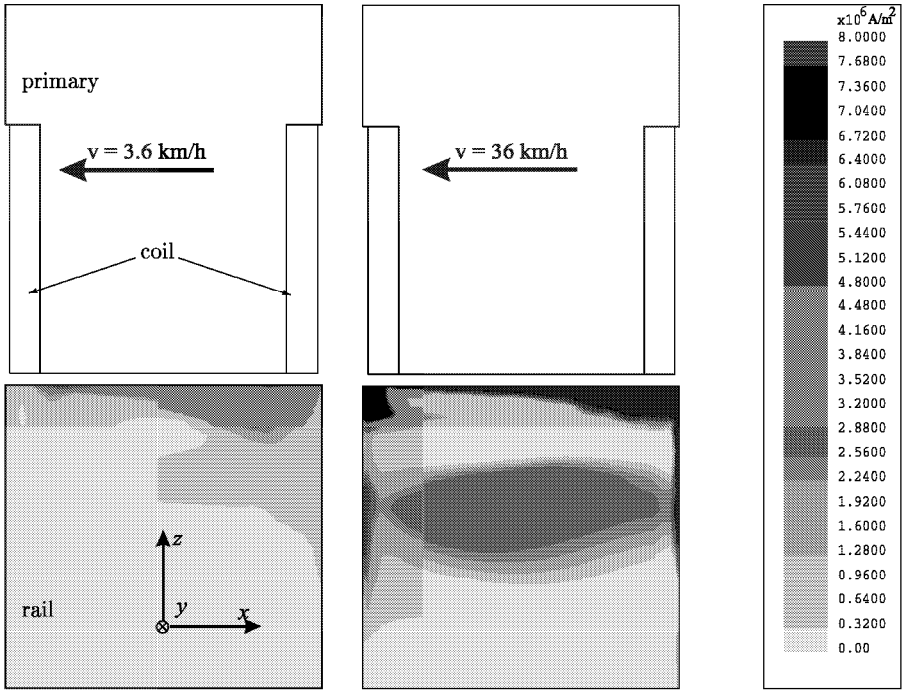


Figure 3.15: Eddy current-density distribution along the cut through the secondary of model E3P (one pole) at  $v = 3.6 \text{ km/h}$  (left) and  $36 \text{ km/h}$  (right).  $A \cdot J = 69250 \text{ A/cm} \cdot \text{A/mm}^2$

### 3.4 Comparison of calculated and measured eddy current brake

The measured results of forces at velocities higher than zero are taken from [2]. Figure 3.16 shows the measured forces of the eddy current brake.

#### 3.4.1 Comparison of force characteristics

The results of the force calculations from model E2P to E3P have been collected in Figure 3.17. Also included in the graphs are the measurement and the force curve obtained by multiplying the forces of model E3P with the end effect factors from chapter 3.2.

The 2-D results are not even near to the measurement. This is mainly a result of the missing transversal end effects. The 3-D results are much closer to the measurement. The difference between the computed and measured curves is up to 15% at moderate velocities.

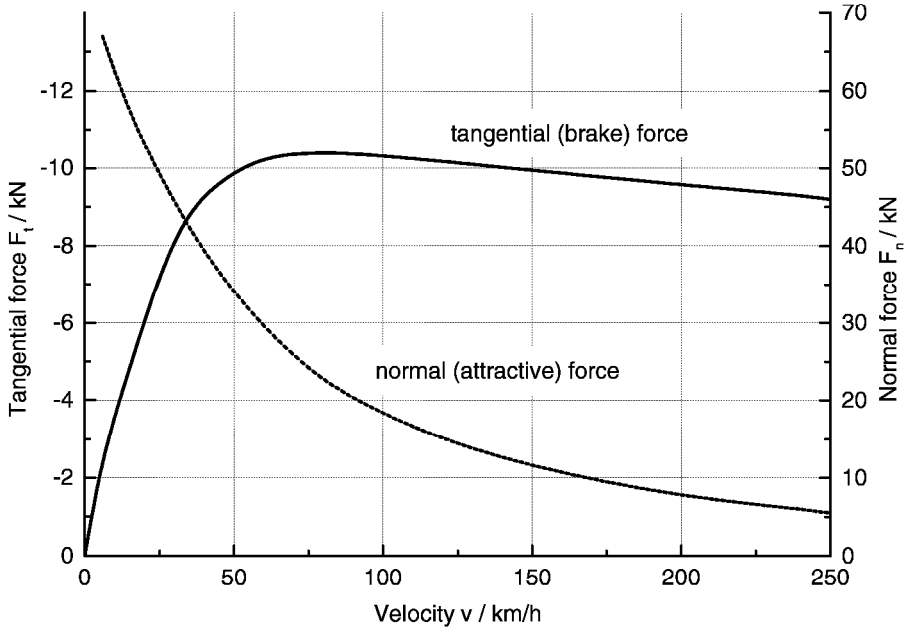


Figure 3.16: Measured forces of the six-pole eddy current brake [2]. The force was measured at an excitation of 67 kA ampere-turns per slot.  $A \cdot J = 69250 \text{ A/cm} \cdot \text{A/mm}^2$

The calculated braking force coincides better with the measurement than the attractive force. Still, the results of model E3P and the measurement differ up to 60%. In order to overcome the differences between the measured and calculated forces, the conductivity of the rail was varied. This led to a conductivity value of  $2.5 \cdot 10^6 \text{ S/m}$ .

The measured and the calculated forces according to model E3P $\kappa_{2.5}$  are in good coincidence. This model is based on model E3P, whereas the conductivity of the rail was changed<sup>5</sup> to  $\kappa_{\text{rail}} = 2.5 \cdot 10^6 \text{ S/m}$  and the end effect factor has been applied. The influence of the conductivity will be investigated in more detail in chapter 4.6.

<sup>5</sup>The influence of conductivity variation and the realistic values will be considered in detail in chapter 4.6.2

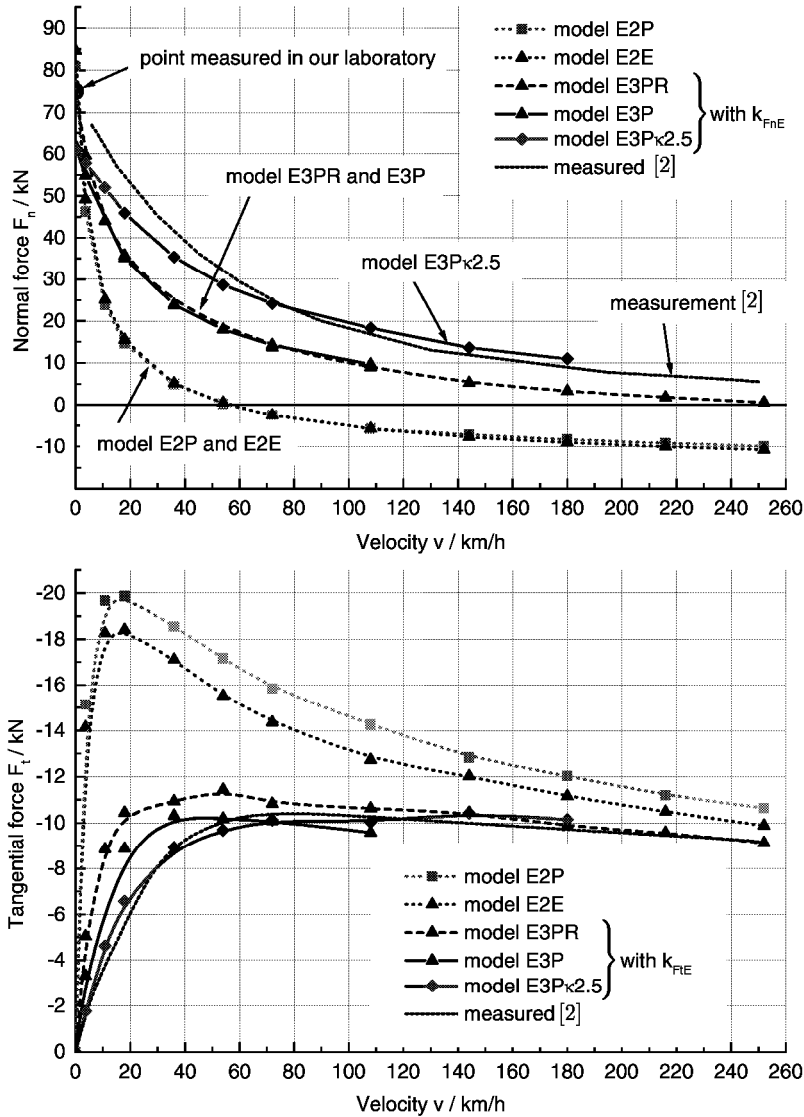


Figure 3.17: Normal and tangential force of the eddy current brake. Comparison of calculated and measured results. Models E3PR, E3P and E3P $\kappa$ 2.5 are not shown for the full velocity range due to convergence problems of the numerical calculation.  $A \cdot J = 69250 \text{ A/cm} \cdot \text{A/mm}^2$

### 3.4.2 Comparison of flux density characteristics

For low velocities, there is still a significant difference between computation and measurement of the normal and tangential force components, especially for the models E3PR and E3P. One explanation for that difference is a non-constant air gap at the measurement. The eddy current brake is slightly bent at moderate velocities. The effect of that bend is a differing air gap along the machine in moving direction. It is well known, that the attractive force of an electrical machine will increase with decreasing air gap [21] due to the increase of flux density. This is illustrated in Figure 3.18, where the flux density at different air gaps is shown as a comparison of calculation and measurement.

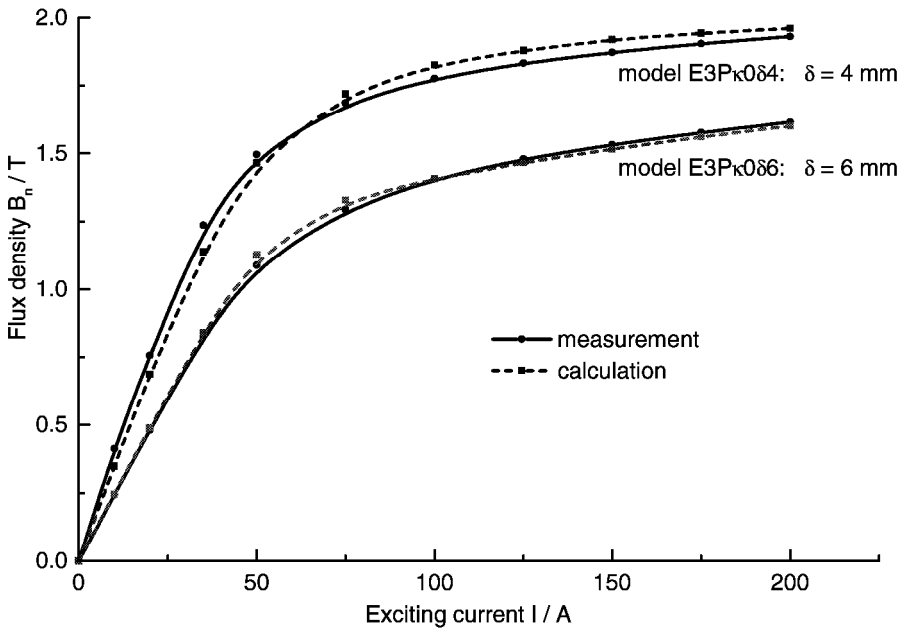


Figure 3.18: Normal component of flux density in the air gap at the middle of an inner pole of the eddy current brake. 3-D calculations are compared with measurements at different air gaps (4 and 6 mm).

In order to validate the calculations of the flux density distribution along the  $x$ -axis, a measurement of the flux density at standstill was made. In the FE model E3P, the conductivity of the primary part and the rail has been set to zero. This speeds up the calculation and is valid, because at zero velocity there will be no eddy currents flowing in the rail. The measurement was carried out at our lab using a *Hall* probe (see chapter 5). The air gap was chosen to be

9 mm and the number of ampere-turns per coil is as low as 3.3 kA to avoid overheating during measurement. The comparison of measured and calculated flux density at one pole, vertically and horizontally centered in the air gap is shown in Figure 3.19.

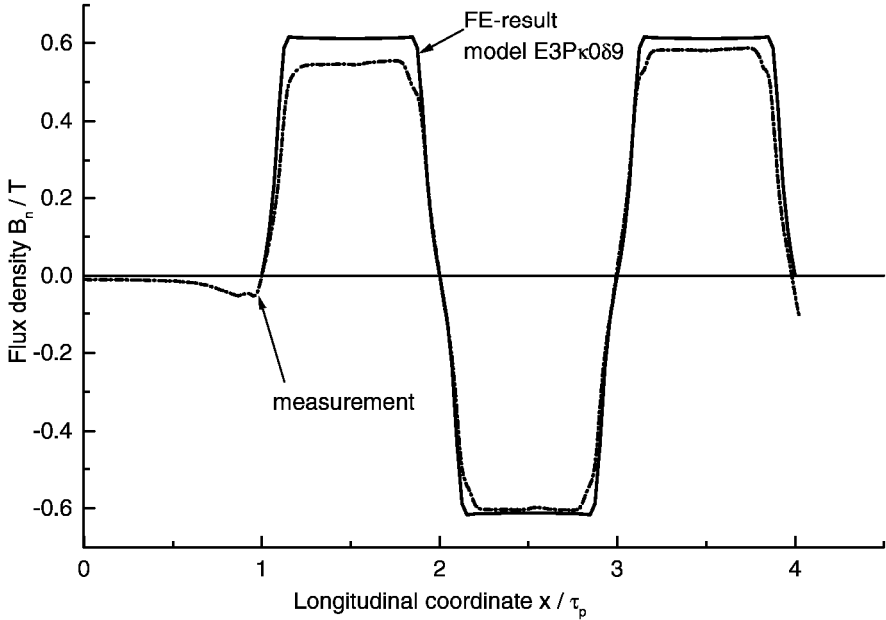


Figure 3.19: Comparison of computed and measured normal component of flux density. The *Hall* probe was placed horizontally and vertically centered in the air gap on one pole of the linear eddy current brake at standstill. The FE result has been derived by a periodic model of one pole (E3P $\kappa0\delta9$ ) and has been extended by duplication to fit the measured range of longitudinal coordinate.  $A \cdot J = 673 \text{ A/cm} \cdot \text{A/mm}^2$

The differences between measurement and computed results arise (apart from measurement accuracy) due to the following reasons:

1. The geometrical dimensions of the FE model lie within a tolerance of  $\pm 1 \text{ mm}$ , which is 0.6 % of the pole pitch  $\tau_p$ , as compared with the real device. This causes the slightly different pole width in Figure 3.19.
2. The longitudinal end effects can not be taken into account with the 3-D model due to hardware limitations. Therefore, a periodic model has been used.
3. The holes in the primary yoke, in which the coils are connected are disturbing the flux. These holes have not been modeled.

### 3.5 Concluding remarks to the calculation of the linear eddy current brake

In this chapter, a linear eddy current brake (ECB) has been calculated with different FE-models and compared with measurements. It was tried to include the influence of end effects, even if it has not been possible to include longitudinal and transversal end effects in the same model.

Although some of the FE-models look simple, the modeling effort is quite big. The 2-D models have been optimized for each velocity to keep the numerical error as small as possible. For the 3-D models, this would have been too time consuming. Thus, an appropriate element size has been chosen depending on the estimated penetration depth of the flux into the materials. The results of the FE calculations have been checked using the flux density distribution in the whole model. If the flux density distribution did not look realistic, the model has been refined in the corresponding regions. For high velocities, it has not been possible to stabilize the numerical calculations by refining the mesh. For some models, it has been possible to obtain a solution by using a result from a calculation at a lower velocity as an initial data set (see chapter 3.3.1). In this case, the time needed for the solving process went up from some hours to some days including the solving time for the lower velocity result.

The measurements presented in this chapter were taken from different sources. A prototype of the eddy current brake has been available for measurements at the Institute of Electrical Energy Conversion of the Darmstadt University of Technology. The measurements could only be performed for standstill, because it was not possible to build a rotational test rig or to move the ECB over the rail. This would have been too expensive to realize. The measurement results for velocities higher than zero were taken from [2]. These measurements were performed on a rotational test rig of the company *Knorr-Bremse*.

The thermal load ( $A \cdot J = 69250 \text{ A/cm} \cdot \text{A/mm}^2$ ) of the eddy current brake is very high. This can not be reached without forced cooling in continuous operation. The operating times are only up to 1 minute at the maximum excitation with a time to cool down of 10 minutes before re-operating [2]. To allow continuous operation, the thermal load would have to be drastically reduced.

The results in this chapter show, that the applied methods to investigate the eddy current brake obtain reasonable results. Thus, the same methods will be applied to the investigation of a linear induction machine. Here, the expected error should be low.

# Chapter 4

## Numerical calculation of a linear induction machine

### 4.1 Determination of initial conditions

The design of the linear machine underlies some restrictions and cannot be chosen freely (see chapter 2). Therefore, some constraints have to be denominated.

- The linear machine has to fit into the maximum available space. Thus, it would be good to choose a design with a minimum space required for end turns and a maximum space on active iron.
- The power supply is located on the locomotive. For this reason either a converter has to be chosen which is already operating with power reserve, or the newly designed converter has to fit into the restricted space on the locomotive [52].
- The maximum normal force (added to the weight of the loco) should not exceed the limit of mechanical stress on the railway track. Depending on the track, the limit is a weight of 18 000 kg - 25 000 kg per wheel set, which is corresponding to a normal force of 177 kN - 245 kN [36].

#### 4.1.1 Evaluation of winding concepts

In order to obtain a space saving winding, there are mainly three possibilities available.

- A: Two phases with  $m = 2$   $q = 1$   $\frac{w}{\tau_p} = 1$
- B: Three phases with  $m = 3$   $q = \frac{1}{2}$   $\frac{w}{\tau_p} = \frac{2}{3}$
- C: Any combination as a yoke winding

The first two possibilities will be discussed in this section, whereas the third possibility has been investigated separately and is presented in chapter 4.3.

For concept A, the sketch of the distributed coils in the primary slots is shown in Figure 4.1.



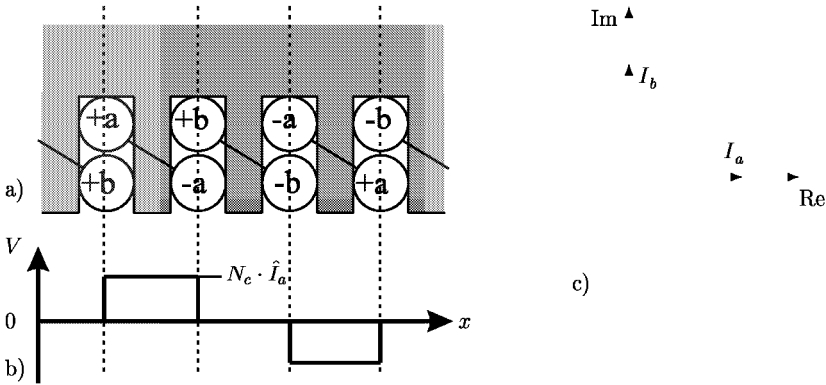


Figure 4.1: a) Sketch of the primary winding of the two-phase concept A. b) For the m.m.f. distribution ( $V$ ), the slot width has been neglected. c) The current phasors for the applied time instant are shown on the right.

Phases a and b have to be supplied by currents with a phase shift of 90 degree. The excited m.m.f. will be symmetrical. Either a special two-phase transformer or a two-phase inverter is needed for the power supply.

The sketch of distributed coils for the three-phase concept B with fractional slot winding is shown in Figure 4.2.

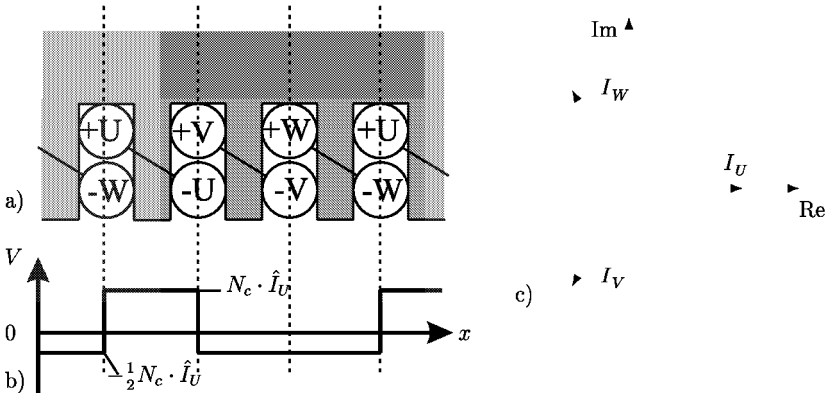


Figure 4.2: a) Sketch of the primary winding of concept B. b) For the m.m.f. distribution ( $V$ ), the slot width has been neglected. c) The current phasors for the applied time instant are shown on the right.

The symmetrical three-phase current system can be generated by a three-phase standard inverter or a three-phase transformer. The excited m.m.f. will not be symmetrical. Therefore, a detailed investigation on the m.m.f. harmonics is shown in Table 4.1. The winding factors are calculated using Equations (1.8), (1.12) and (1.13). The ordinal number of space harmonics is only listed up to  $\nu = 5$ . There will be more space harmonics with higher ordinal number, but their influence can be neglected for this evaluation due to their low impact on the e.m.f. with a factor of  $1/\nu$ .

Table 4.1: Winding factors for the space harmonics of concept A and B.

ordinal number of space harmonics $\nu$	A: $m = 2$ distribution factor $k_{d\nu}$	$q = 1$ pitch factor $k_{p\nu}$	$\frac{w}{\tau_p} = \frac{1}{2}$ relative amplitude $k_{w\nu}/\nu$	B: $m = 3$ distribution factor $k_{d\nu}$	$q = \frac{1}{2}$ pitch factor $k_{p\nu}$	$\frac{w}{\tau_p} = \frac{2}{3}$ relative amplitude $k_{w\nu}/\nu$
1	1	0.707	0.707	1	0.866	0.866
2	-	-	-	1	-0.866	0.433
3	1	0.707	0.24	-	-	-
4	-	-	-	1	-0.866	0.216
5	1	-0.707	0.14	1	0.866	0.173

Concept B yields a larger fundamental winding factor than concept A, but also more space harmonics with partially larger amplitudes. Concept B has been chosen for the investigation because the three phase induction machine fits best into the already existing electric circuit on the locomotive. The converters for the driving motors may be used.

#### 4.1.2 Prerequisites for the machine design

Non-linear magnetization  $B(H)$  of the iron parts has to be taken into account. The  $B(H)$ -curves for the primary and secondary part are shown in Figure 4.3.

The primary part is assumed to consist of a cobalt iron alloy with a high saturation polarization (2.35 T) and low losses at very high flux densities ( $p_{2.0} = 1.8 \text{ W/kg}$ )<sup>1</sup> [53]. This material has been chosen to reach the maximum performance of the linear machine. But as it is very expensive, it would not be used for a commercial production of the linear machine.

The secondary part is the traction rail, which is the same as introduced in chapter 3. Therefore, the same magnetization curve has been applied.

<sup>1</sup> $p_{2.0} = 1.8 \text{ W/kg}$  means, that the iron losses at a flux density of 2 T and 50 Hz frequency would be 1.8 W per kg mass.

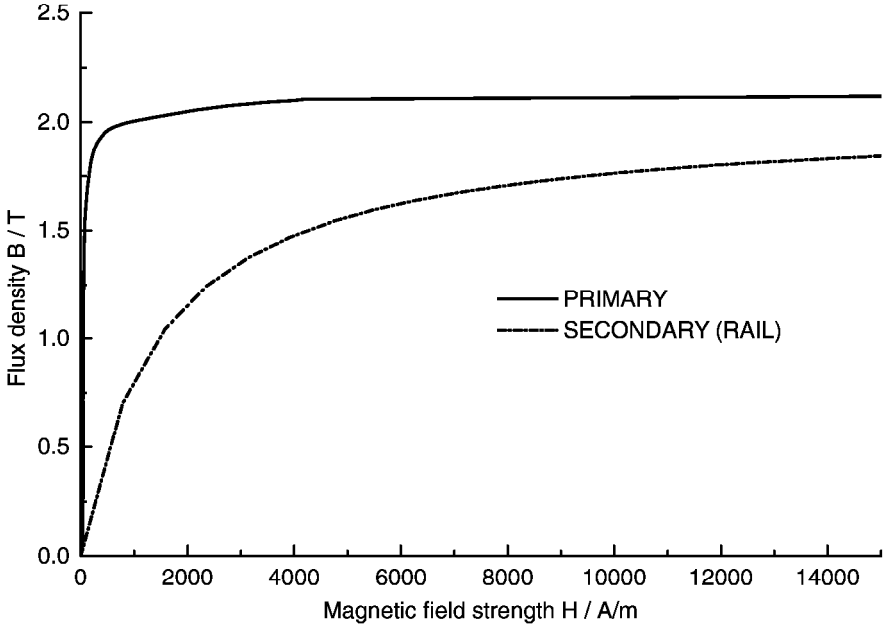


Figure 4.3:  $B(H)$  curves for calculation of the asynchronous linear machine. Primary: *Vacoflux* [53], secondary: rail steel [11].

## 4.2 Calculation of a linear induction machine with fractional slot winding

The fractional slot winding is often chosen as a tool to reduce cogging torque e.g. in permanent magnet machines (see chapter 1.1.3). In this case, the fractional slot winding has been chosen mainly because it needs the least space for manufacturing the coils for a three-phase winding, especially considering the winding overhangs.

### 4.2.1 Geometrical considerations

A coil geometry with extremely small end turns and no crossings can be achieved by a fractional slot winding with the number of slots per pole and phase ( $q$ ) equal to  $1/2$ .

The electrical and geometrical parameters of the linear machine have been chosen as listed in Table 4.2.

Investigations have been made concerning the optimum of the pole pitch for different numbers of poles with a fractional slot winding (see Figure 4.4 and Figure 4.5 [54]).

Table 4.2: Parameters of the design with fractional slot winding.

Symbol	Value	Unit	Name
$f_s$	104.2	Hz	Primary frequency
$p$	4		Number of pole pairs
$N_c$	22		Number of turns per coil
$m$	3		Number of phases
$q$	1/2		Slots per pole and phase
$v_{syn}$	120	km/h	Synchronous speed
$\delta$	6.5	mm	Air gap
$\tau_p$	159	mm	Pole pitch
$l_{Fe}$	96	mm	Primary width
$w/\tau_p$	2/3		Chording factor
$w$	106	mm	Equivalent coil span
$A$	2062	A/cm	Current-sheet

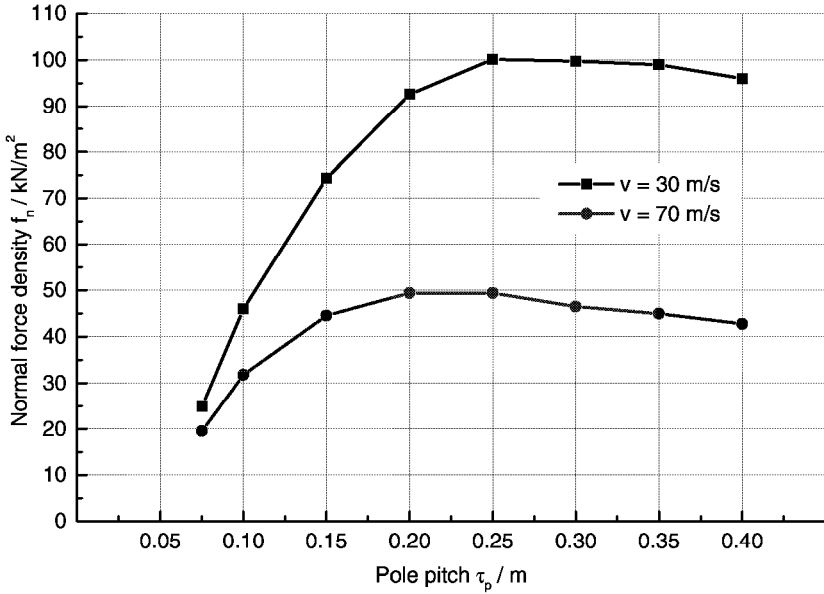


Figure 4.4: Maximum normal (attractive) force density obtained for different pole pitches [54]. Calculations are based on periodic 2-D models. Forces are related to the rail-facing surface of the machine. The thermal load has been fixed on a constant low value of  $A \cdot J = 5400 \text{ A/cm} \cdot \text{A/mm}^2$ .

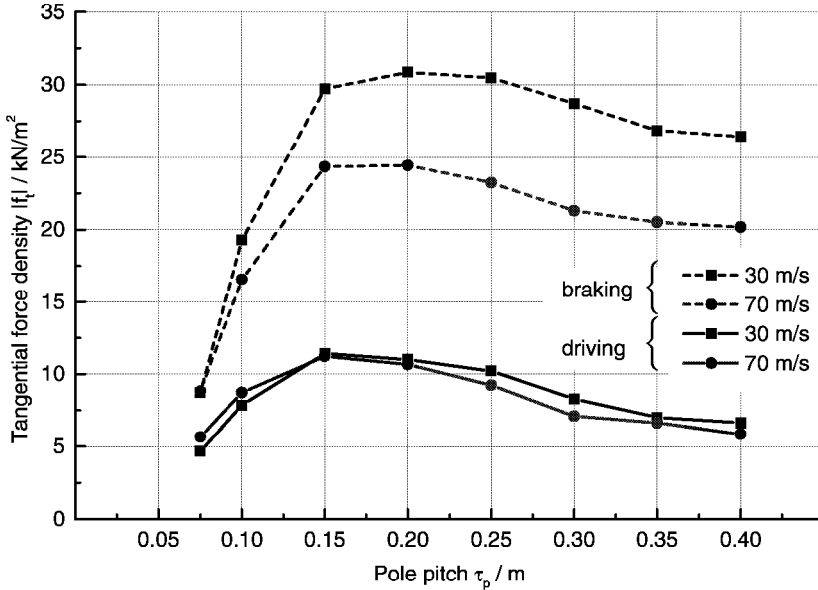


Figure 4.5: Maximum tangential force density obtained for different pole pitches [54]. Calculations are based on periodic 2-D models. Forces are related to the rail-facing surface of the machine. The thermal load has been fixed on a constant low value of  $A \cdot J = 5400 \text{ A/cm} \cdot \text{A/mm}^2$ .

The objective of [54] has been to optimize the pole pitch of a linear induction machine with the given space restrictions in order to obtain the highest possible forces. The optimization has been carried out using the FE program *MEGA* with 2-D periodic models. To avoid the influence of saturation effects, the ampere-turns per coil were kept on a low value of 5000 A, which gave a thermal load of  $5400 \text{ A/m} \cdot \text{A/m}^2$ .

The general tendency is that the obtained forces increase with increasing pole pitch as shown in Figure 4.4 and 4.5. Later on, the enormously increased pole pitch decreases the forces. This behavior is due to the fixed maximum length of the machine. Therefore, the number of poles has to change from 4 to 2 when the limit of length is reached. So, there is in the end a small machine with only two very large poles. However, the number of poles should not be too small because of the increasing influence of end effects on a linear machine with a decreasing number of poles [12].

The actually chosen pole pitch of 159 mm is a result of numerical and analytical considerations. Originally, the ALIM should be designed for the high speed train *ICE 3*. Its maximum speed is  $v = 330 \text{ km/h}$  [55] and a nominal inverter frequency of  $f = 285 \text{ Hz}$  [52]. To operate the frequency inverter around its nominal point, the pole pitch of the linear machine has been

chosen to be  $\tau_p = 0.16$  m, which is according to the numerical optimization. Later on, the German railway company intended to build a prototype of the ALIM and to operate it in a freight train locomotive. These locomotives usually have a maximum speed of 120 km/h. Therefore, the nominal supply frequency for the calculations has been chosen to 104.2 Hz according to a synchronous velocity of the traveling wave of 120 km/h. Using this synchronous speed and the pole pitch, the frequency is calculated using (4.1).

$$f = \frac{v_{syn}}{2\tau_p} \quad (4.1)$$

The number of pole pairs is given by the pole pitch and the maximum machine length of 1413 mm. The primary width results from the maximum machine width of 250 mm, subtracted by the end turn width and optimized regarding to the width of the rail.

The number of turns is the result of an optimization of the thermal load of the machine together with its cooling conditions and the slot width<sup>2</sup>.

The air gap is chosen according to the demands of the German railway company. They performed trial runs with the eddy current brake. The conclusion was, that the nominal air gap of 6.5 mm is a secure value to avoid mechanical contact between linear machine and rail. Due to the attractive forces, the linear machine is bending slightly and the air gap is reduced to about 4.5 mm in the middle of the actor.

### 4.2.2 Finite Element modeling

In order to figure out the behaviour of the newly designed machine, FE-calculations have been carried out. By analyzing the electrical input (voltage and current at the terminals of coils) and the mechanical output (forces acting on secondary), it is possible to locate losses, the power factor and the apparent power.

A picture of the first design of the ALIM (L3PF) is shown in Figure 4.6. A complete list of used numerical models is given in Appendix B.

The primary currents are impressed in the stator coils. The conductors of the presented machine are assumed to be directly water-cooled with hollow copper conductors<sup>3</sup>. The motor is considered to be infinitely long (modeled with periodical boundary conditions) to keep the number of nodes and mesh elements of the 3-D model within reasonable limits.

Thus, only transversal end effects are taken into account. The mesh of the 3-D model with applied boundary conditions is shown in Figure 4.7.

<sup>2</sup>For more information concerning the analytical optimization of electrical machines, see [16, 17, 21]

<sup>3</sup>The objective was to reach forces similar to the eddy current brake. To realize this aim, a very high current-density ( $> 14$  A/mm<sup>2</sup>) is needed. This might be possible for short-time operation without additional cooling. For continuous operation, the coils have to be water-cooled.

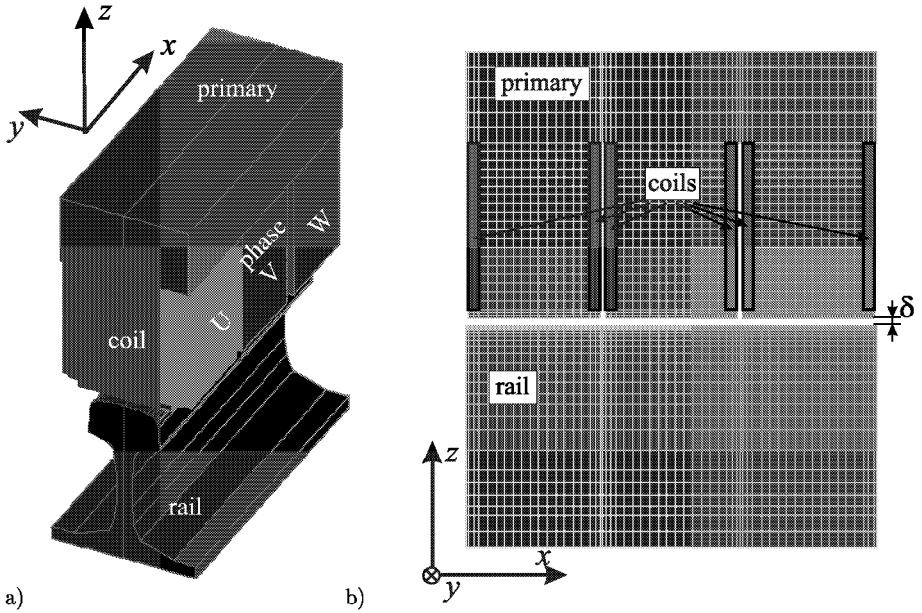


Figure 4.6: First design of the ALIM (L3PF). a) 3-D view of the complete geometry, b) cut view through the symmetry plane.

In order to avoid high eddy currents in the primary yoke, the primary iron is assumed to be ideally laminated (infinitely thin insulated iron sheets). With the used software, it has not been possible to apply an anisotropic conductivity, so the conductivity of the primary is set to zero. The conductivity of the rail is set to  $\kappa_{rail} = 5 \cdot 10^6 \text{ S/m}$  (according to measurements, see chapter 5.3).

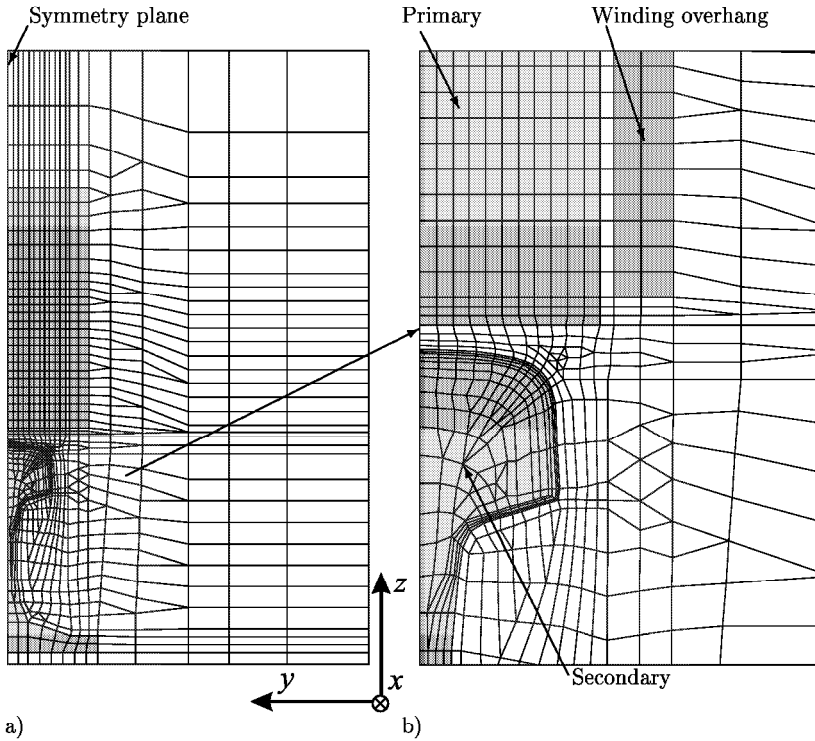


Figure 4.7: Mesh of the three-dimensional model L3PF. a) complete mesh geometry, b) zoom in air gap region.

#### 4.2.3 Results of the force calculations

Figure 4.8 shows the numerically calculated forces for 11 000 ampere-turns per coil impressed current in dependence of the slip  $s$ .

The tangential force of the ALIM with fractional slot winding has basically a behaviour like any other induction machine. The difference is that the characteristic force-slip-curve is shifted to braking force values, so that there is a considerable braking force at the synchronous point. This is due to additional space harmonics arising from the fractional slot winding.

Splitting the primary traveling magnetic field into its harmonic components<sup>4</sup> (see Figure 4.9 for the resulting force components), there will be a second harmonic traveling into the

<sup>4</sup>This has been done with a 2-D analytical model with constant permeability and an impressed current-sheet. A *Fourier* analysis of the m.m.f. has been performed and the flux density components on the rail surface have been calculated using *Maxwell's* equations. With (1.38), the force of each harmonic is calculated and then summarized to obtain the resulting force curve [56].



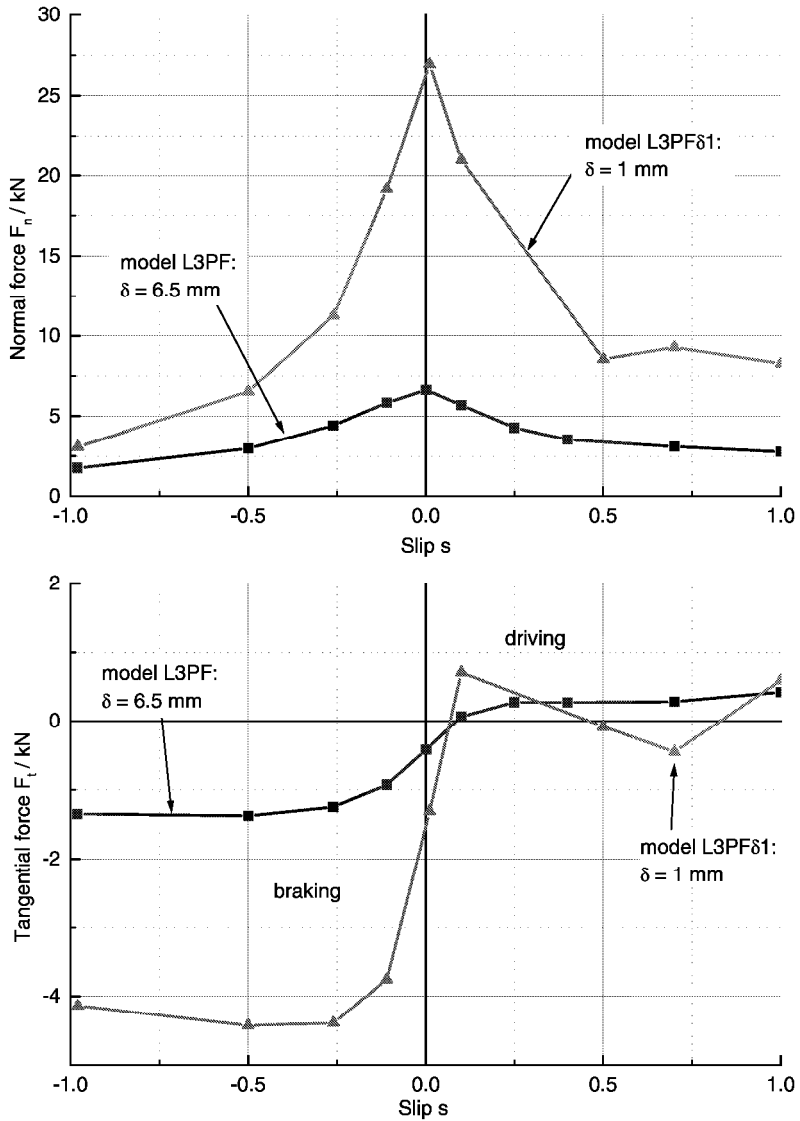


Figure 4.8: Normal and tangential force of the ALIM with fractional slot winding at different air gap heights. The coil excitation equals 11 000 ampere-turns.  $A \cdot J = 29060 \text{ A/cm} \cdot \text{A/mm}^2$

opposite direction and a fourth harmonic traveling into the same direction as the fundamental wave. There are other harmonics as well, but since their amplitude is very small, they will not be considered. It can be seen that mainly the second harmonic contributes to the shift of the fundamental.

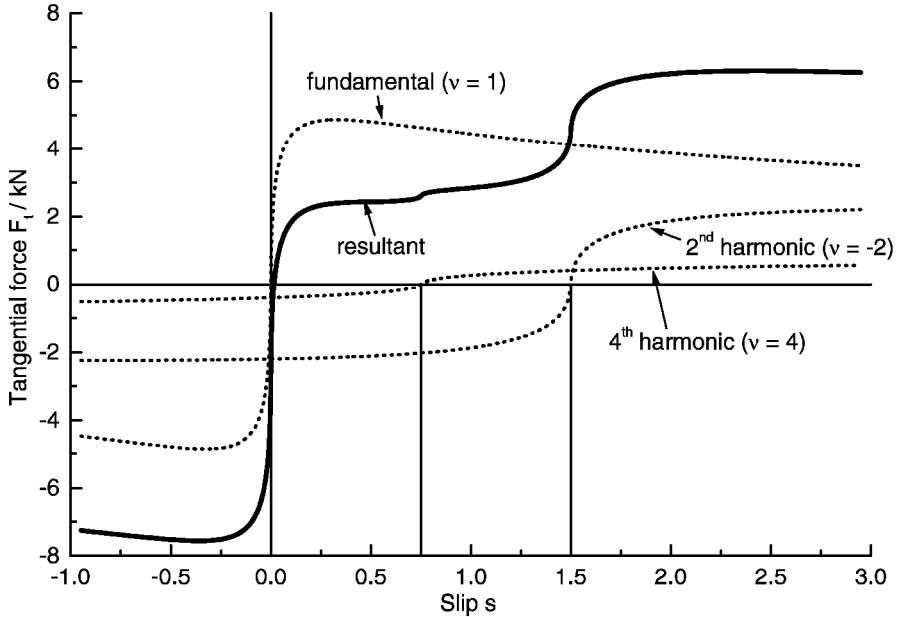


Figure 4.9: Analytically calculated main components of the tangential force of the ALIM with fractional slot winding due to 1st, 2nd and 4th field harmonic [56]. The electrical parameters are listed in Table 4.2.

The normal force component is only weakly influenced by higher space harmonics. Still, it is not symmetrical to the synchronous point. At slip values between 0.5 and 1, the influence of the second and fourth harmonic can be seen. Comparing the result of model L3PF $\delta$ 1 in Figure 4.8 with the resulting force curve in Figure 4.9, it is obvious, that the numerical calculation takes into account all harmonics of the traveling magnetic field.

#### 4.2.4 Flux density characteristics

The space harmonics with higher ordinal number  $\nu > 1$  in the air gap are not only depending on the primary winding, but also on the air gap itself. Two-dimensional models only differing in air gap height have been investigated focusing on the distribution of flux density at the surface of the secondary. The results of this investigation at a velocity of 36 km/h (according to a slip of 70%) are shown in Figure 4.10. There has also been carried out a *Fourier* analysis on the flux density distribution along the pole pitch to separate the space harmonics. The peak values together with the order of harmonics are also shown in Figure 4.10.

One can see that the amplitude of the 4th harmonic at small air gaps is about twice as big as the value of the flux density amplitude of the fundamental wave.

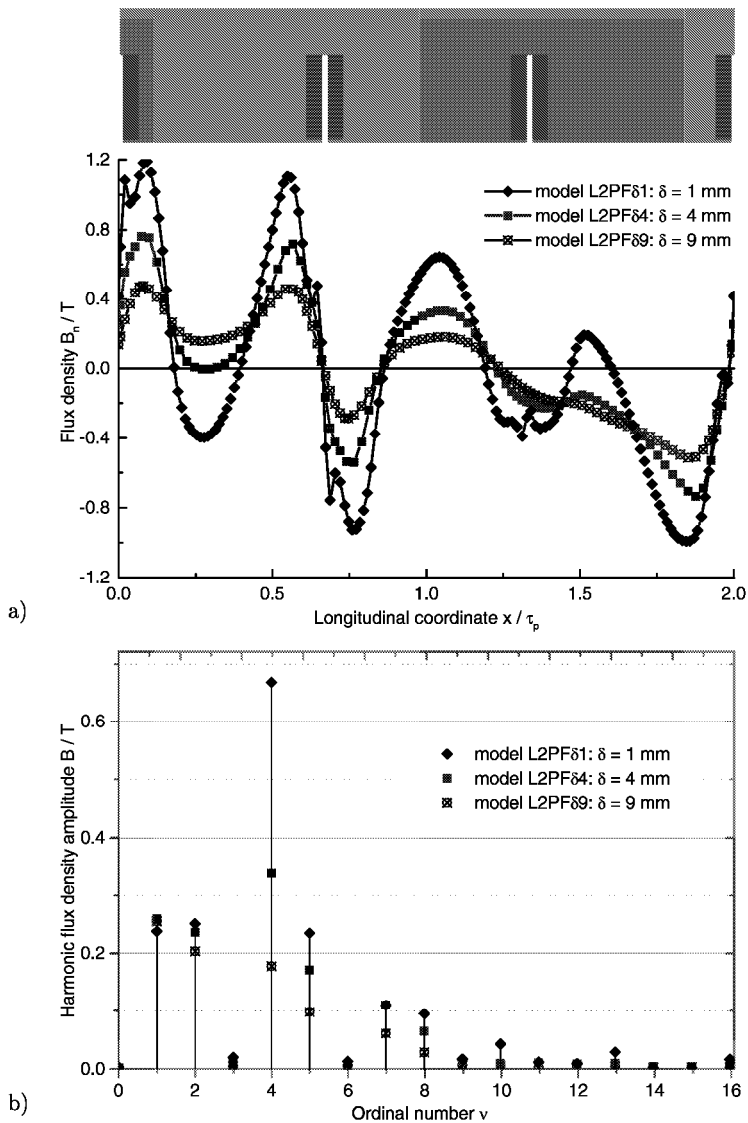


Figure 4.10: a) Flux density distribution and b) harmonics of flux density at the rail surface for different air gaps. The coil excitation equals 11 000 ampere-turns.  $v = 36$  km/h.

### 4.3 Calculation of a linear induction machine with integer slot yoke winding

Using the fractional slot winding, the additional space harmonics with even ordinal number ( $\nu = -2; 4; -8; 10; \dots$ ) make useful thrust force characteristics impossible. This should be overcome with the yoke winding.

The yoke winding is originated in the toothed-ring winding invented by *Gramme* in 1870 [57]. Its construction is simple, enabling any pole-pitch by supplying the appropriate slot currents [58]. However, the stray losses are bigger than those of a normal winding.

The normal winding has two sides of a coil embedded in a slot and thus contributing to the force generation. With the yoke winding, only one side of the coil is located in a slot, whereas the other side lies on the back of the yoke, closing the loop.

The advantage of the yoke winding to provide freely choosable pole pitches with small winding overhangs comes along with the disadvantage of higher stray losses and a bigger quantity of copper needed, compared to a normal winding of the same kind.

#### 4.3.1 Choice of the winding

The geometric parameters of a polyphase winding are related to each other as shown in (1.11). With the number of phases equal to 3, the number of slots per pole and phase, the number of slots and the number of poles are free to choose.

In order to decrease the influence of the longitudinal end effects, the number of poles should be big. But the number of slots cannot be too big, because there must be still some iron left to guide the flux.

With a number of slots per pole and phase of 1 and a number of slots equal to 12, a reasonable solution seems to be found. The pole pitch has been adapted to obtain 8 poles on a maximum machine-length of 1413 mm, including two end teeth. The coils are not chorded, because this would lead to an undesirable reduction of flux.

The whole geometry for one pole of the yoke winding is shown in Figure 4.11a. For simplicity reasons, the coils are designed with constant width in the slot and on the yoke. In reality, the coils would be optimized to reach a small lateral winding overhang, shown in Figure 4.12. To visualize the difference between yoke winding and fractional slot winding, the latter design is shown in Figure 4.11b.

Table 4.3 demonstrates the coils scheme for a two-layer winding with three phases and one slot per pole and phase. Since no chording is applied, the two layers will be shown in the following figures as one layer.

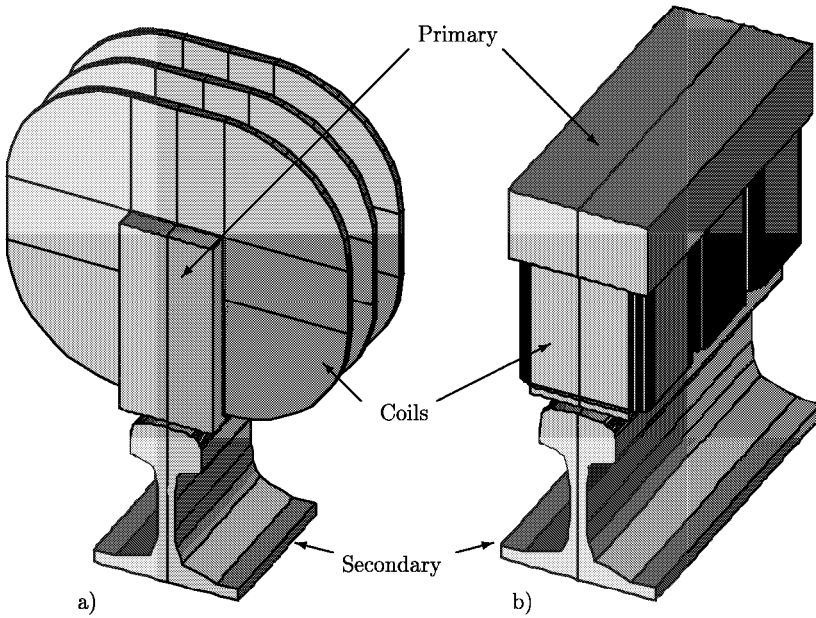


Figure 4.11: 3-D models with coils, primary part and secondary part (rail). a) yoke winding model, one pole, b) fractional slot winding model, two poles.

Table 4.3: Two-layer winding diagram for the yoke winding,  $m=3$ ,  $q=1$ ,  $w/\tau_p=1$

layer 1	+U	-W	+V	-U	+W	-V
layer 2	+U	-W	+V	-U	+W	-V

In addition to the comparison of the yoke winding and the fractional slot winding, the influence of slot closure on the forces has been investigated. The basic geometry with open and semi-closed slots can be seen in Figure 4.13. With open slots, a third variant of design can be investigated, which is shown in Figure 4.13 c). The coils are occupying the whole space of the slots.

To keep this design comparable with the others, the same current sheet and current-density have been applied. Therefore, the number of turns has been increased to  $N_c = 13$  and the current has been reduced to  $I = 420$  A.

The parameters of the investigated machine are listed in Table 4.4.

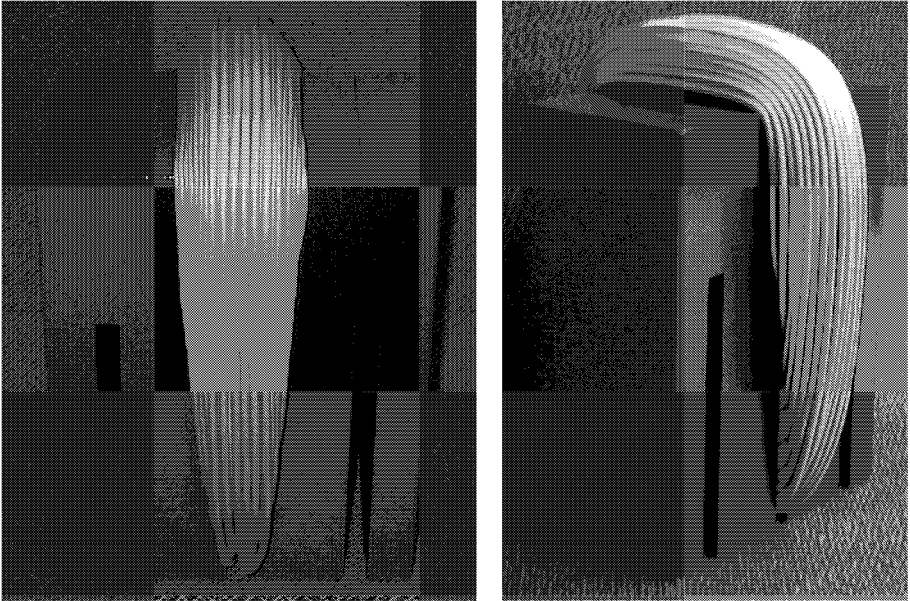


Figure 4.12: Wooden model of the yoke winding. One pole with only one coil wound to the inner slot. Left: front view; right: side view.

Table 4.4: Parameters of the linear machine with yoke winding.

Symbol	Value	Unit	Name
$A$	2062	A/cm	Current-sheet
$f_s$	104.2	Hz	Primary frequency
$I$	500	A	Primary current
$l_{Fe}$	96	mm	Primary width
$m$	3	-	Number of phases
$N_c$	11	-	Number of turns per coil
$p$	4	-	Number of pole pairs
$q$	1	-	Slots per pole and phase
$v_{syn}$	120	km/h	Synchronous speed
$w$	106	mm	Equivalent coil span
$\delta$	6.5	mm	Air gap
$\tau_p$	159	mm	Pole pitch

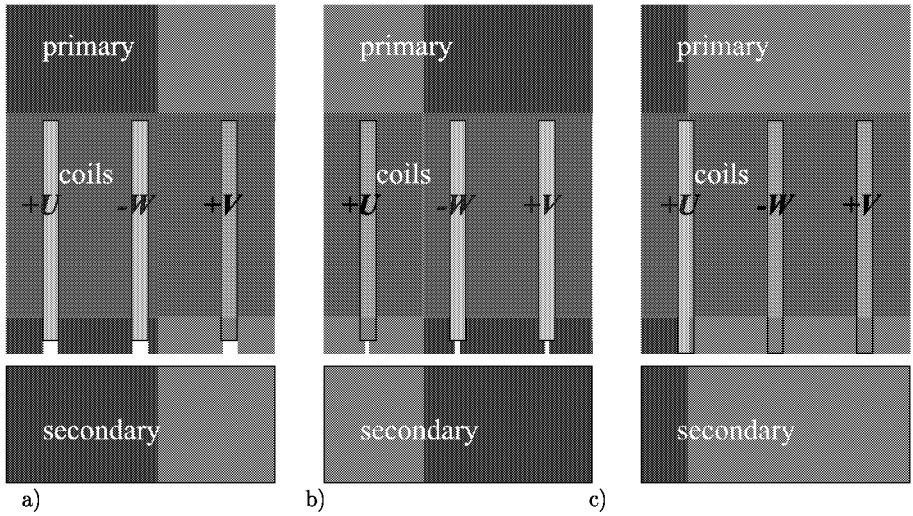


Figure 4.13: Basic geometry of the investigated machines (integer slot yoke winding) with applied winding diagram for one pole: a) open slots (model L3PY0), b) semi-closed slots (model L3PY), c) increased coil height (model L3PYI). Return coil side is neglected.



### 4.3.2 Finite Element modeling

The base-plane mesh of the investigated approaches is shown in Figure 4.14. The mesh is refined at the air gap and on the surface of the rail. The scalar potential on the boundary of the model is set to zero, whereas the symmetry plane is defined on the left border of Figure 4.14. One pole has been modeled using coils with impressed currents.

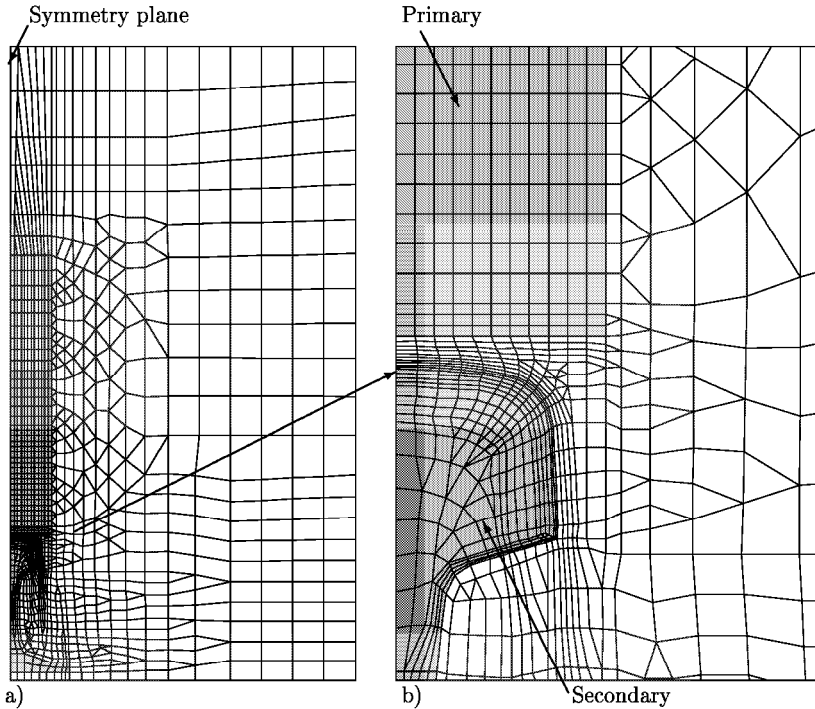


Figure 4.14: Base plane of the FE-model L3PY for the yoke winding. a) Full model, b) Zoom of air gap region.

Symmetric and periodic boundary conditions have been applied on the models to reduce computation time. Due to the use of periodic boundary conditions, longitudinal end effects have not been taken into account. Non-linear magnetizing curves have been applied for the primary [53] and the secondary part [11] and are shown in Figure 4.3. For the primary a special sheet with very high permeability was chosen to keep the magnetizing current as low as possible.

The calculation results for the linear induction machine with yoke winding are given in chapter 4.5 along with the comparison between fractional slot winding and integer slot yoke winding for the linear induction machine.

## 4.4 Evaluation of longitudinal end effects by two-dimensional calculations

There have been many approaches in the recent literature to estimate the influence of the longitudinal end effect of linear machines by analytical calculations [59, 60, 61]. The longitudinal end effect is mostly split into two effects [62]. One is the effect of the entry wave, which is distorting the flux density in the air gap near the front end of the linear machine (related to the movement). The other is the exit wave, which is acting mainly at the rear end of the linear machine. The longitudinal end effect results in a force reduction due to the impact on the flux density distribution. In this chapter, an attempt is made to find a factor expressing the impact of the longitudinal end effects on the force generation. This factor should then be applied on the three-dimensional calculations of forces in the following chapters.

### 4.4.1 Flux density characteristics

The separation of end effects will be performed by means of an example with two different slip values ( $s = 0$  and  $s = -1$ ). First, the flux lines are shown in Figure 4.15. In Figure 4.16 and Figure 4.17, the normal and the tangential component of the flux density in the middle of the air gap of the two-dimensional models are shown. Two different models at two different velocities are presented. One of them is modeled with longitudinal end effects (L2EF), while the other is modeled with periodic boundary conditions (L2PF).

At synchronous speed ( $s = 0$ ), the end effect can clearly be seen as the difference between the two characteristics of the normal component of the flux density. At  $s = -1$ , there is hardly any difference between the two curves. To separate the end effect, the two curves have to be subtracted. The result is a mixture of entry and exit wave, which is shown in Figure 4.18. The tangential flux density component does not show a distinctive difference between the different curves.

The end effect flux density has a characteristic as shown in [13, 63]. The entry wave starts at the left side and decreases with an exponential function to the right side. It penetrates almost the whole length of the linear machine. The exit wave starts at the right side and dies out quite fast. It penetrates about two poles at the exit end of the machine. According to [64], the pole pitch of the entry wave is expressed by (4.2).

$$\tau_{ps} = (1 - s)\tau_p \quad (4.2)$$

At zero slip, the end effect curve is more distinctive than at  $s = -1$ . The characteristic of the flux density at negative slip is already distorted. So, the additional distortion by the end effect is not as significant as the distortion at the synchronous point.

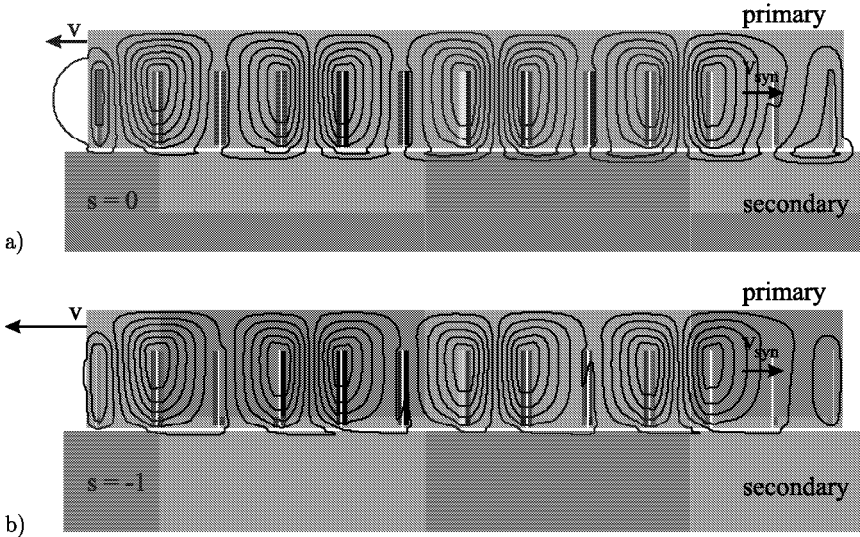


Figure 4.15: Flux lines of the fractional slot winding model L2EF. a)  $s = 0$ , the traveling magnetic field is as fast as the moving primary. This is similar to a DC excitation at zero velocity. b)  $s = -1$ , the traveling magnetic field is slower than the moving primary. This leads to a distortion of the flux lines and a decrease of the penetration depth in the secondary.

The tangential flux density component does not show any typical end effect behavior. There is a difference between the periodic results and the end effect results, but it can neither be separated in entry and exit wave, nor does it show any decay. Moreover, it seems almost constant over the machine length and is only depending on the slip.

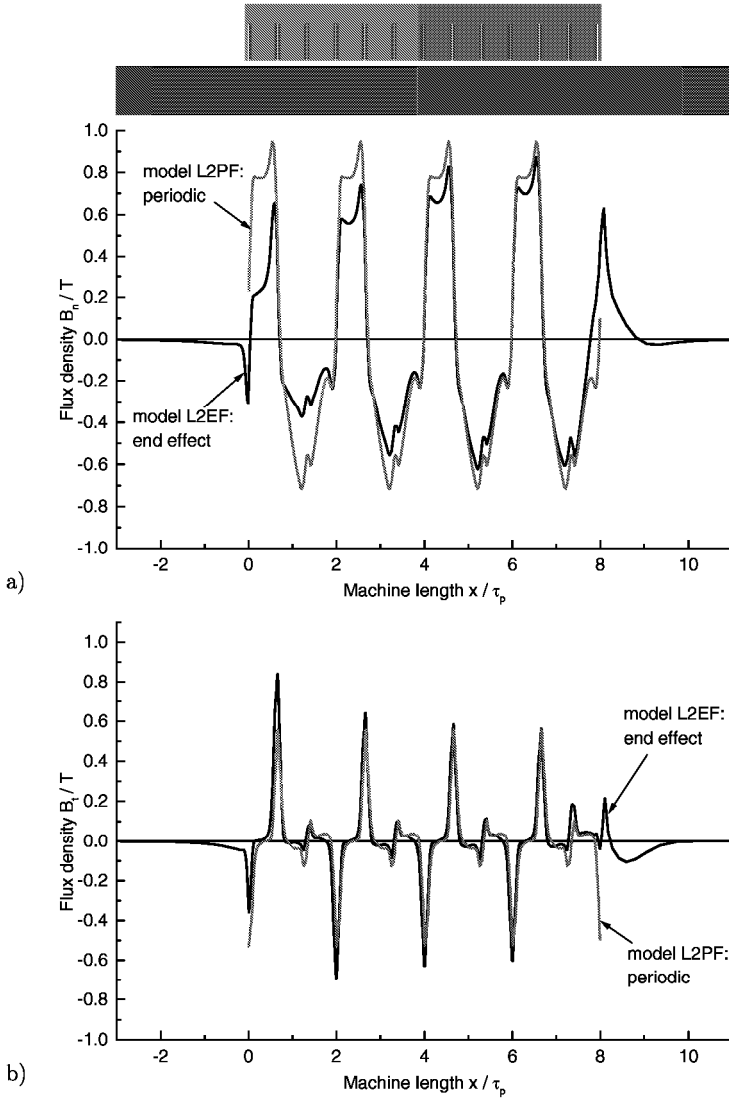


Figure 4.16: Normal and tangential component of flux density in the middle of the air gap of the two-dimensional models L2EF and L2PF. The end effect model L2EF is compared with the periodic model L2PF. The comparison is made for the slip value  $s = 0$ .

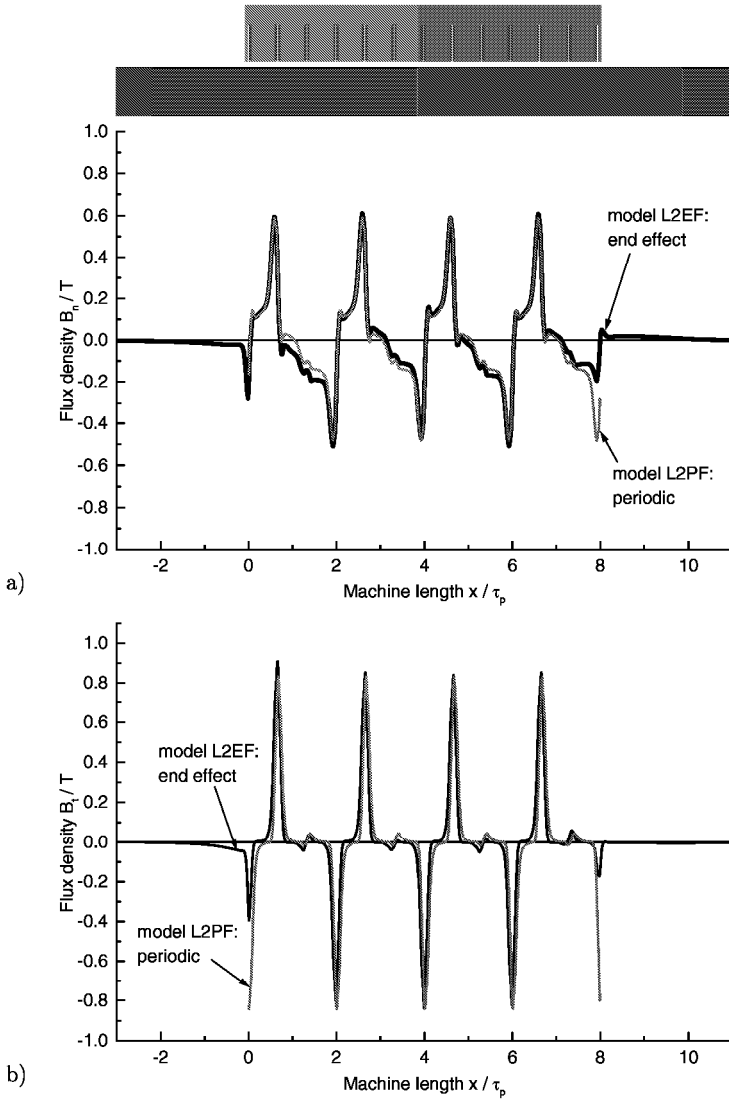


Figure 4.17: Normal and tangential component of flux density in the middle of the air gap of the two-dimensional models L2EF and L2PF. The end effect model L2EF is compared with the periodic model L2PF. The comparison is made for the slip value  $s = -1$ .

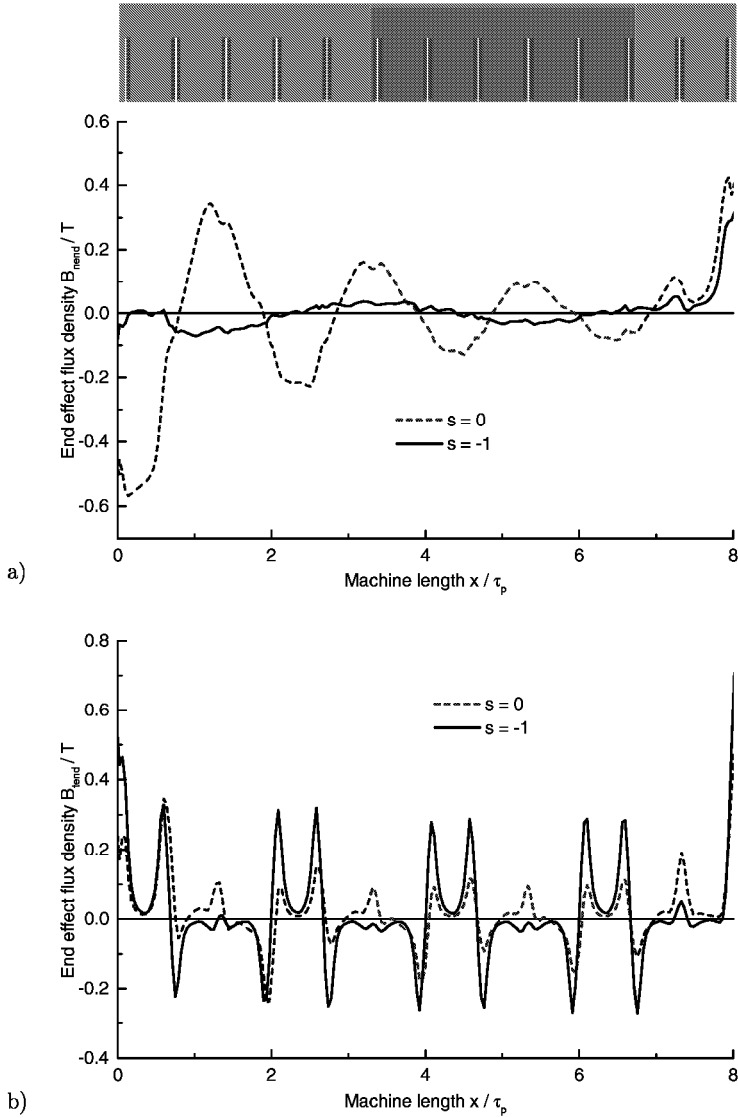


Figure 4.18: Normal and tangential end effect component of flux density. The curves are derived by subtracting the flux density characteristics of Figure 4.16 and Figure 4.17.

#### 4.4.2 Influence of longitudinal end effects on force generation

For the estimation of the end effect influence on the force characteristics, the two-dimensional models L2EF and L2PF have been calculated at different slip. The results are shown in Figure 4.19.

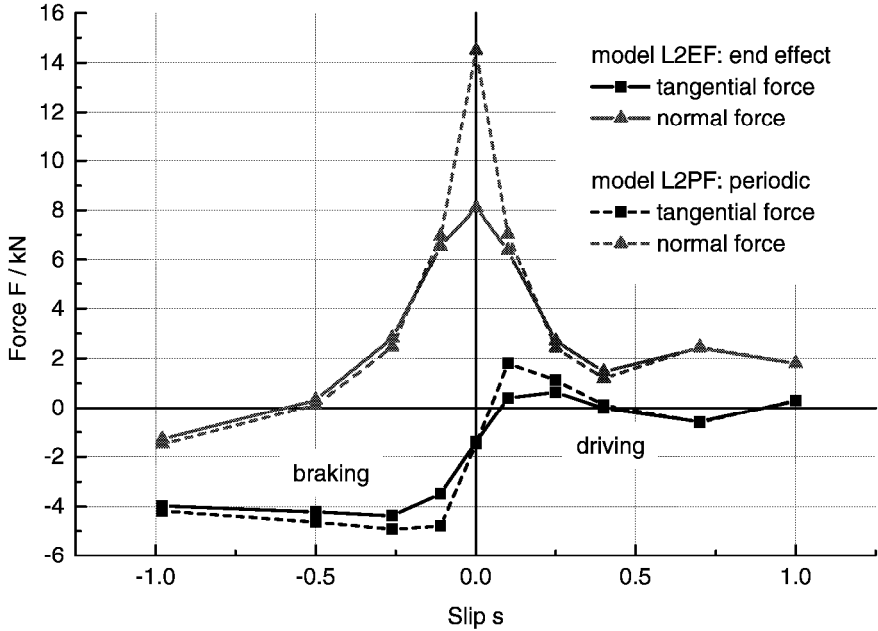


Figure 4.19: Normal and tangential force characteristics. The end effect model L2EF is compared with the periodic model L2PF.

The end effect has the biggest influence on the normal component of the force at zero slip. This is due to the dependence of the normal force on the squares of the flux density components (see (1.37)).

The tangential force component does not show any end effect influence for zero slip. This can also be explained by the flux densities (see (1.38)). The normal component of flux density shows a big end effect at zero slip, whereas the tangential component does not show an end effect at all.

For the normal force, this means that the end effect influence acting on the flux density is squared, because the normal force depends on the square subtraction of the flux densities. The tangential force depends on the product of the flux densities and therefore does not show an influence at zero slip.

### 4.4.3 Longitudinal end effect factor

Corresponding to chapter 3.2.3 it has been tried to find a factor expressing the influence of the longitudinal end effects on the force generation. The end effect factor for the tangential force component  $k_{FtL}$  is calculated using 4.3 and the end effect factor for the normal force component  $k_{FnL}$  using 4.4. Therefore, the forces have been compared according to (4.3) and (4.4).

$$k_{FtL} = \frac{F_{tEL}}{F_{tPL}} \quad (4.3)$$

$$k_{FnL} = \frac{F_{nEL}}{F_{nPL}} \quad (4.4)$$

$F_{tEL}$  is the tangential force component of model L2EF,  $F_{tPL}$  the tangential force component of model L2PF,  $F_{nEL}$  the normal force component of model L2EF and  $F_{nPL}$  is the normal force component of model L2PF. The end effect factors are shown in Figure 4.20.

There are three extreme points, where an error is caused by the zero crossing of the 2-D force curves. Unlike the end effect factors of the linear eddy current brake, this characteristic does not have a clear tendency. Therefore, it is supposed to use the normal end effect factor only for zero slip and to use the tangential end effect factor for all slip values. The two extreme points have been removed by linear interpolation.



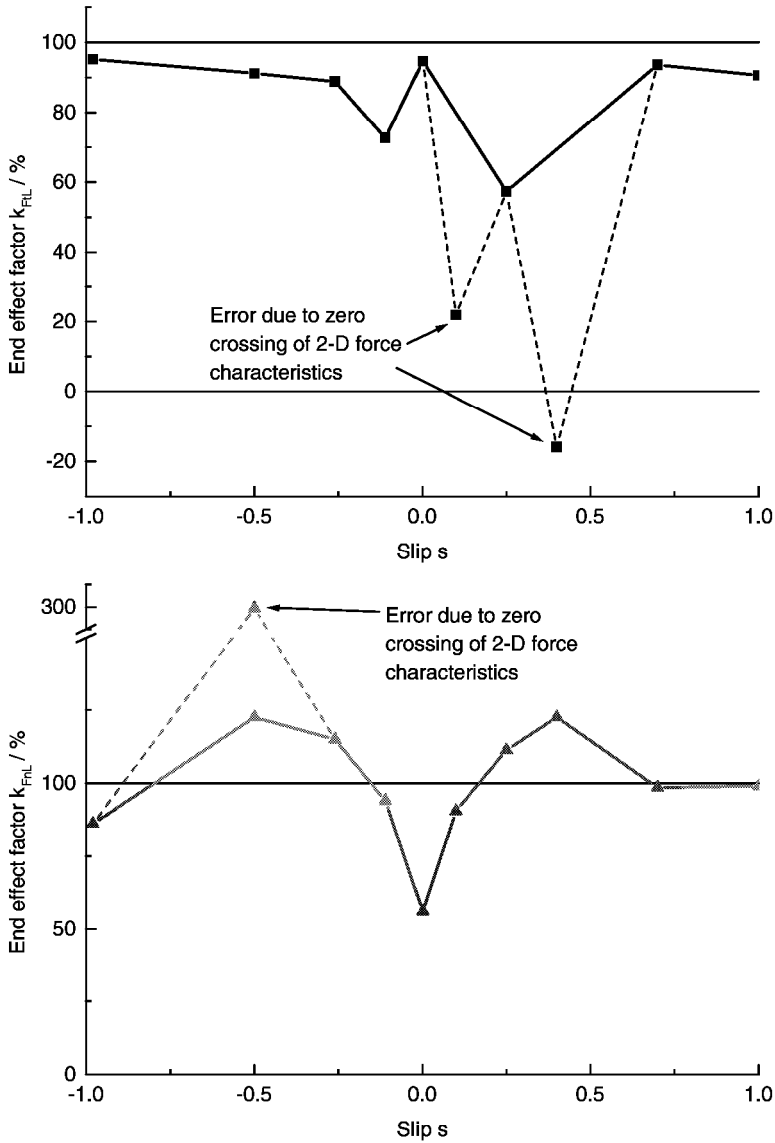


Figure 4.20: Longitudinal end effect factors of the linear induction machine on normal and tangential forces. Mean values are 86% for  $k_{FL}$  and 99% for  $k_{FnL}$ .

## 4.5 Comparison of linear induction machine with fractional slot and integer slot yoke winding

### 4.5.1 Analytical calculation of the coil resistance

The high current-sheet of 2062 A/cm at 14.1 A/mm<sup>2</sup> current-density allows only short time operation of several minutes at natural cooling conditions. Therefore, the coils are considered to be directly water cooled.

The resistance of the coils is calculated analytically based on a wire geometry shown in Figure 4.21. The parameters of the coils are listed in Table 4.5.

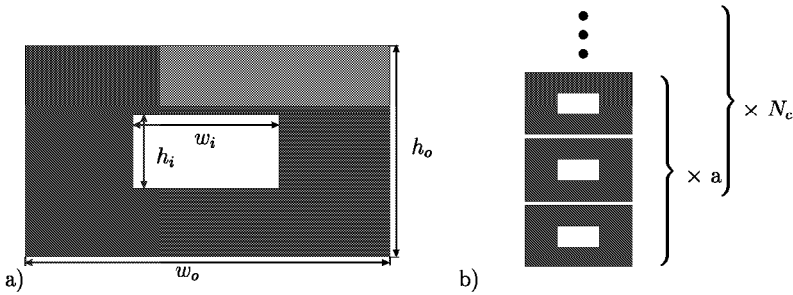


Figure 4.21: Geometry of the water cooled wire. The number of parallel wires is expressed by  $a$  and the number of turns by  $N_c$ . a) Structure of one coil. b) The black dots are indicating that the parallel wires are repeated  $N_c$  times to form the coil.

The penetration depth [21] of the current in the coils is calculated using (3.3) with the parameters shown in Table 4.4, yielding a value of 8 mm. The second order skin effect is shown in Figure 4.22.

Eddy current losses in the winding overhangs due to the stray field are neglected.

The shown geometry of water-cooled wires is a simplification for the analytical calculation. In reality, such hollow conductors would not be built due to an immense pressure drop<sup>5</sup> of the water in the range of 100 000 N/m<sup>2</sup>. The coils would rather be built with cooling ducts between groups of wires, according to [22].

<sup>5</sup>This has been estimated using procedures shown in [21] with a velocity of the cooling water of 2 m/s.

Table 4.5: Parameters of the water cooled coils for the yoke winding model (Values according to best case, see chapter 1.1.4).

Symbol	Value	Unit	Name
$a$	3	-	Number of parallel wires
$b_c$	7.9	mm	Width of active copper in the slot
$b_s$	10	mm	Width of the slot
$h_i$	1	mm	Height of cooling duct
$h_o$	3.5	mm	Height of conductor
$k$	5.64	-	Average of second order skin effect factor in the slot
$k$	1.63	-	Average of second order skin effect factor for the coil
$k_{r2}$	1..14.5	-	Second order skin effect factor per conductor
$k_{r1}$	1.0003	-	First order skin effect factor
$l_c$	702	mm	Average length of one turn
$p_p$	$1..N_c \cdot a$	-	Parameter
$R_0$	4.42	m $\Omega$	DC resistance per slot
$R_s$	6.89	m $\Omega$	AC resistance per slot
$w_i$	2	mm	Width of cooling duct
$w_o$	3.95	mm	Width of conductor
$\delta_p$	8	mm	Penetration depth at 104.2 Hz
$\eta$	-0.5	-	First order skin effect parameter
$\kappa$	$49.25 \cdot 10^6$	1/ $\Omega$ m	Average conductivity of copper (56°C)
$\mu$	$4 \cdot \pi \cdot 10^{-7}$	Vs/Am	Permeability of copper
$\nu_h$	0.877	-	Hollow conductor coefficient
$\xi$	0.491	-	Reduced conductor height
$\xi^*$	0.443	-	Reduced conductor height
$\pi$	3.14159	-	Pi
$\varphi(\xi)$	1.005	-	Skin effect function
$\varphi(\xi^*)$	0.019	-	Skin effect function
$\psi(\xi)$	1.003	-	Skin effect function
$\psi(\xi^*)$	0.013	-	Skin effect function

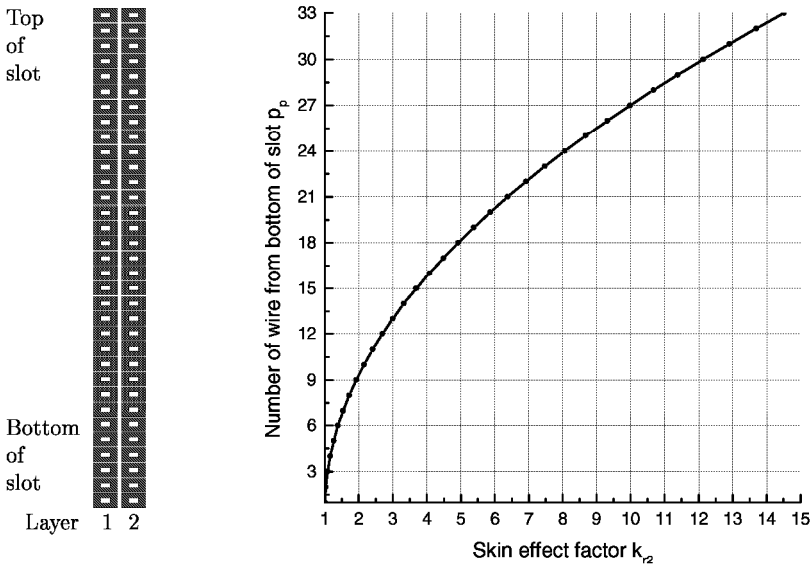


Figure 4.22: Sketch of wires in one slot with calculated second order skin effect factor for each wire.

#### 4.5.2 Results of the force calculations

In Figure 4.23, the three slot designs of Figure 4.13 are compared concerning attractive, tractive and braking forces at constant current in the primary winding. The forces are always related to one linear machine with eight poles.

Comparing open (L3PYO) and semi-closed (L3PY) slots, the open slot version yields higher forces. The model with increased coil height (L3PYI) generates the highest forces. But attention has to be drawn to the influence of the vertical field at the slot opening [65]. The air gap flux penetrates the slot at the opening as a vertical field. The vertical field will induce additional eddy currents in the conductors lying close to the slot opening, thus increasing the losses in these conductors. This effect is not investigated in this thesis.

Figure 4.24 shows the comparison between the integer slot yoke winding (L3PY) and the fractional slot winding (L3PF) design. The semi-closed slot version has been chosen as an example. The other two designs (open slots and increased coil height) show a comparable behaviour.

For low slip values, the attractive forces for semi-closed slots obtained by the yoke winding are up to 24% higher than those of the fractional slot winding. Increasing the slip, the difference

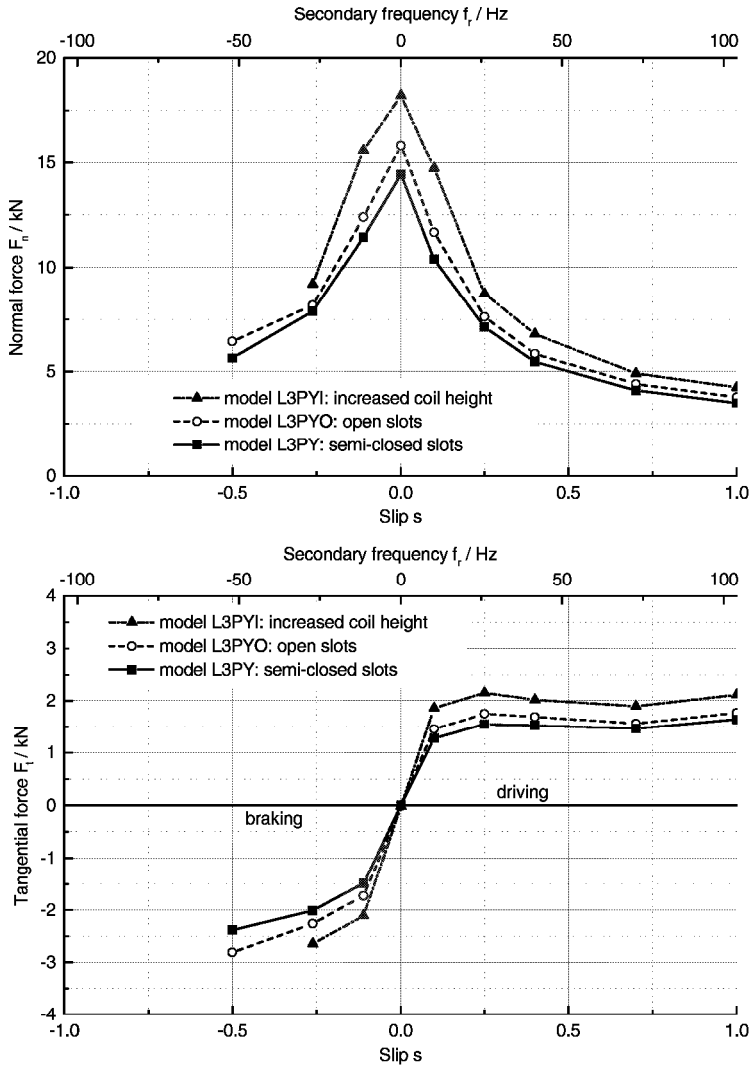


Figure 4.23: Normal (attractive) and tangential force of a linear induction machine with integer slot yoke winding. Comparison of different slot geometries. Missing data points at slip values  $s < -0.5$  are due to convergence problems of the FE calculations.  $A \cdot J = 29060 \text{ A/cm} \cdot \text{A/mm}^2$ ,  $v_{syn} = 120 \text{ km/h}$ .

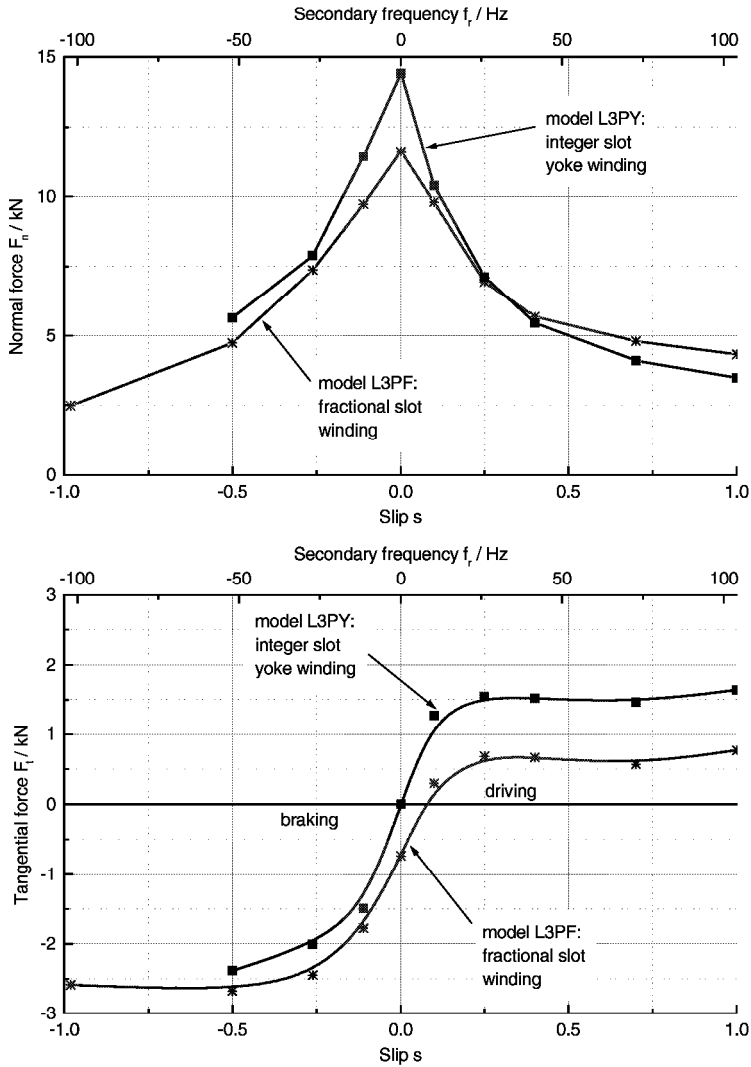


Figure 4.24: Normal (attractive) and tangential force of a linear induction machine with semi-closed slots. Comparison of integer slot yoke winding (L3PY) and fractional slot winding (L3PF). Missing data points at slip values  $s < -0.5$  are due to convergence problems of the FE calculations.  $A \cdot J = 29060 \text{ A/cm} \cdot \text{A/mm}^2$ ,  $v_{syn} = 120 \text{ km/h}$ .

decreases. For slips higher than 0.3, the attractive forces of the fractional slot winding are even higher compared to the yoke winding.

The difference between the two designs on the tangential force is mainly due to the missing 2nd and 4th harmonic for the yoke winding (see chapter 4.5.5). This gives a characteristic curve of the yoke winding which has nearly no tangential force components at zero slip. So, the driving force reaches 157% of the fractional slot winding forces, while the braking component reaches only 82% due to the missing braking effect of the 2nd and 4th harmonic.

The values showing the increase of forces for the investigated coil and slot geometries are listed in Table 4.6.

Table 4.6: Percentage of force increase/decrease for the linear induction machine with yoke winding compared to the fractional slot winding.

Force component	attracting	braking	driving
Open slots	26%	-21%	249%
Semi-closed slots	24%	-18%	157%
Increased coil height	37%	-13%	312%

### 4.5.3 Additional tractive effort

The additional tractive effort of the linear induction machine can be calculated with (4.5), where  $\sum F$  is the tractive effort,  $Q$  is the vertical force due to the weight of the locomotive and  $f_x$  is the adhesion coefficient between rail and wheel.

$$\sum F = (Q + F_n) \cdot f_x + F_t \quad (4.5)$$

The maximum transferable mechanical force of the locomotive equals  $Q \cdot f_x$ . Choosing the German locomotive *BR152*, the weight force including the linear induction machine with a fixation structure and an additional converter amounts about 900 kN. The increased tractive effort of the different ALIM designs for dry ( $f_x = 0.33$ ) and wet ( $f_x = 0.15$ ) weather conditions is listed in Table 4.7. The values are based on a maximum mechanical force without the linear machine of 297 kN for dry and 135 kN for wet conditions.

A proposal of the German railway company was to reduce the weight of the locomotive in order to reach a weight force of 844 kN including all additional components. This could be realized by building a new locomotive using light materials. For this case, the increase of mechanical forces with different ALIM designs is listed in Table 4.8.

Table 4.7: Increase of mechanical forces with different ALIM designs (Figure 4.11 and Figure 4.13) for the locomotive *BR152*.

Type of winding	model	slot and coil geometry	dry rail $f_x = 0.33$		wet rail $f_x = 0.15$	
			driving	braking	driving	braking
Integer slot	L3PYO	open	7.1%	7.8%	9.5%	10.6%
yoke	L3PY	semi-closed	6.3%	7.1%	8.4%	9.6%
winding	L3PYI	increased coil height	9%	9.8%	12%	13.2%
Fractional	L3PFO	open	5.1%	7.7%	5.5%	11.9%
slot	L3PF	semi-closed	4.8%	6.7%	5.2%	10.5%
winding	L3PFI	increased coil height	5.5%	8.3%	6%	12.7%
Forces without linear machine (100 %)			297 kN		135 kN	

Table 4.8: Increase of mechanical forces with different ALIM designs (Figure 4.11 and Figure 4.13) for the locomotive *BR152* with reduced weight.

Type of winding	model	slot and coil geometry	dry rail $f_x = 0.33$		wet rail $f_x = 0.15$	
			driving	braking	driving	braking
Integer slot	L3PYO	open	7.6%	8.3%	10%	11.3%
yoke	L3PY	semi-closed	6.7%	7.5%	8.9%	10%
winding	L3PYI	increased coil height	9.6%	10.4%	12.8%	14%
Fractional	L3PFO	open	5.4%	8.2%	5.8%	12.6%
slot	L3PF	semi-closed	5%	7.1%	5.5%	11.2%
winding	L3PFI	increased coil height	5.9%	8.8%	6.3%	13.5%
Forces without linear machine (100 %)			278 kN		127 kN	

#### 4.5.4 Flux density characteristics

A *Fourier* analysis of the flux density in the symmetry plane in the air gap on the surface of the secondary part has been carried out. The flux density is shown in Figure 4.25 for the yoke winding and in Figure 4.26 for the fractional slot winding. The result of the *Fourier* analysis is shown in Figure 4.27 for the yoke winding and the fractional slot winding.

The open slot model turns out to have higher flux density amplitudes than the semi-closed slot model. This is confirmed by the *Fourier* analysis. Figure 4.27 shows the slightly higher first harmonic and fifth harmonic of the open slot model compared to the semi-closed slot model of the yoke winding. The yoke winding yields a higher fundamental and no harmonics of even order compared to the fractional slot winding. Especially the 2nd and 4th harmonic are missing.

The vector plot of the flux density at the slot opening is shown in Figure 4.28 for the open slot model L3PYO and the semi-closed slot model L3PY at the symmetry plane  $y = 0$ .

The increased stray flux in the semi-closed slot model can be seen by means of the bigger vectors at the tooth tip and slot opening region.



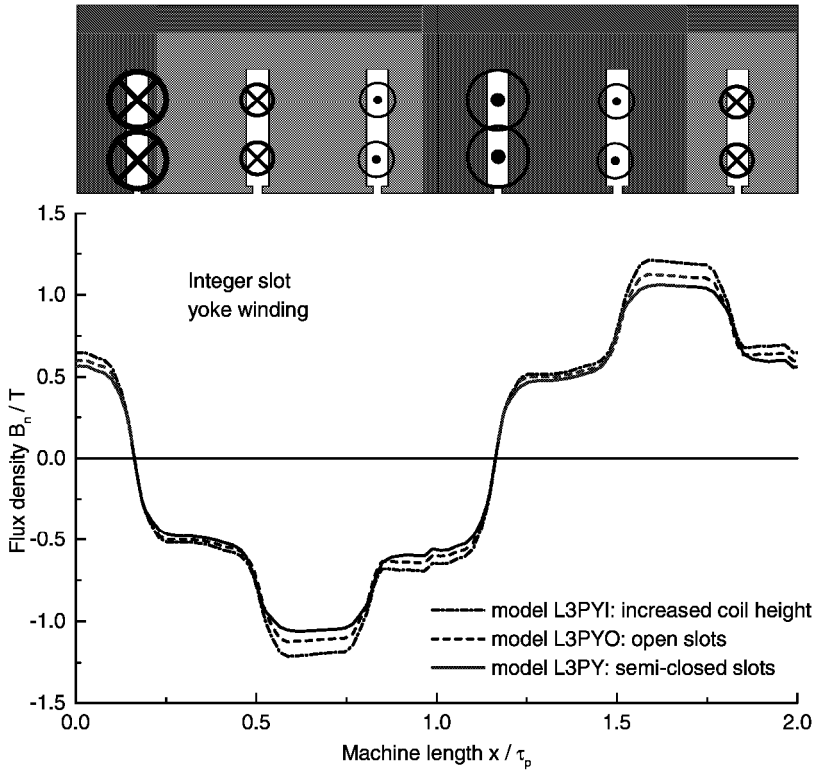


Figure 4.25: Flux density in the symmetry plane in the air gap on the surface of the secondary at no-load ( $s=0$ ). Two poles of the integer slot yoke winding. The present current distribution in the slots is shown above.  $A \cdot J = 29060 \text{ A/cm} \cdot \text{A/mm}^2$ ,  $\delta = 6.5 \text{ mm}$ .

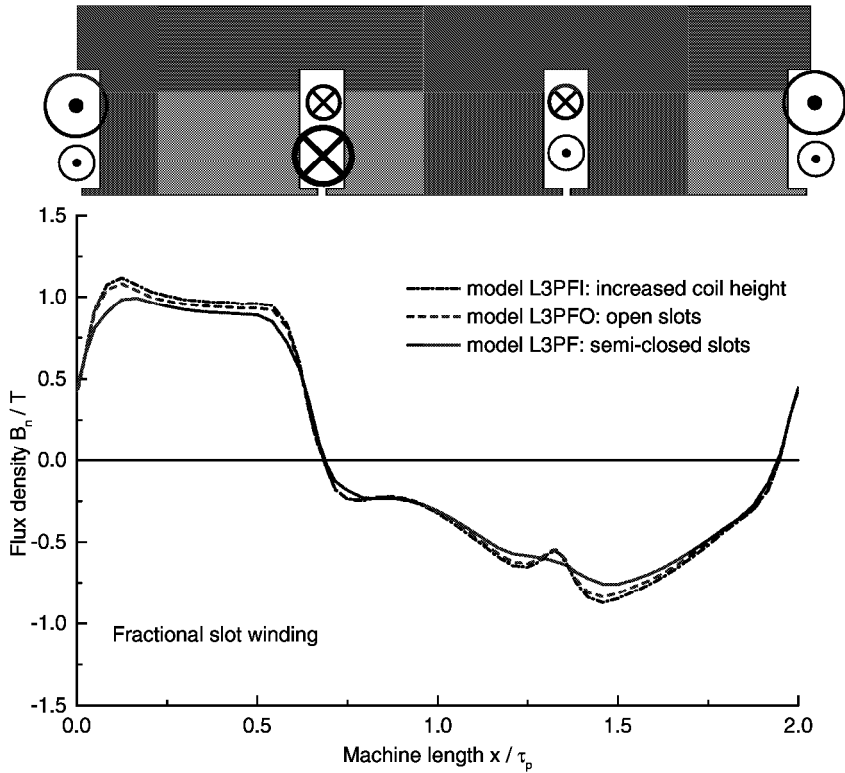


Figure 4.26: Flux density in the symmetry plane in the air gap on the surface of the secondary at no-load ( $s=0$ ). Two poles of the fractional slot winding. The present current distribution in the slots is shown above.  $A \cdot J = 29060 \text{ A/cm} \cdot \text{A/mm}^2$ ,  $\delta = 6.5 \text{ mm}$ .

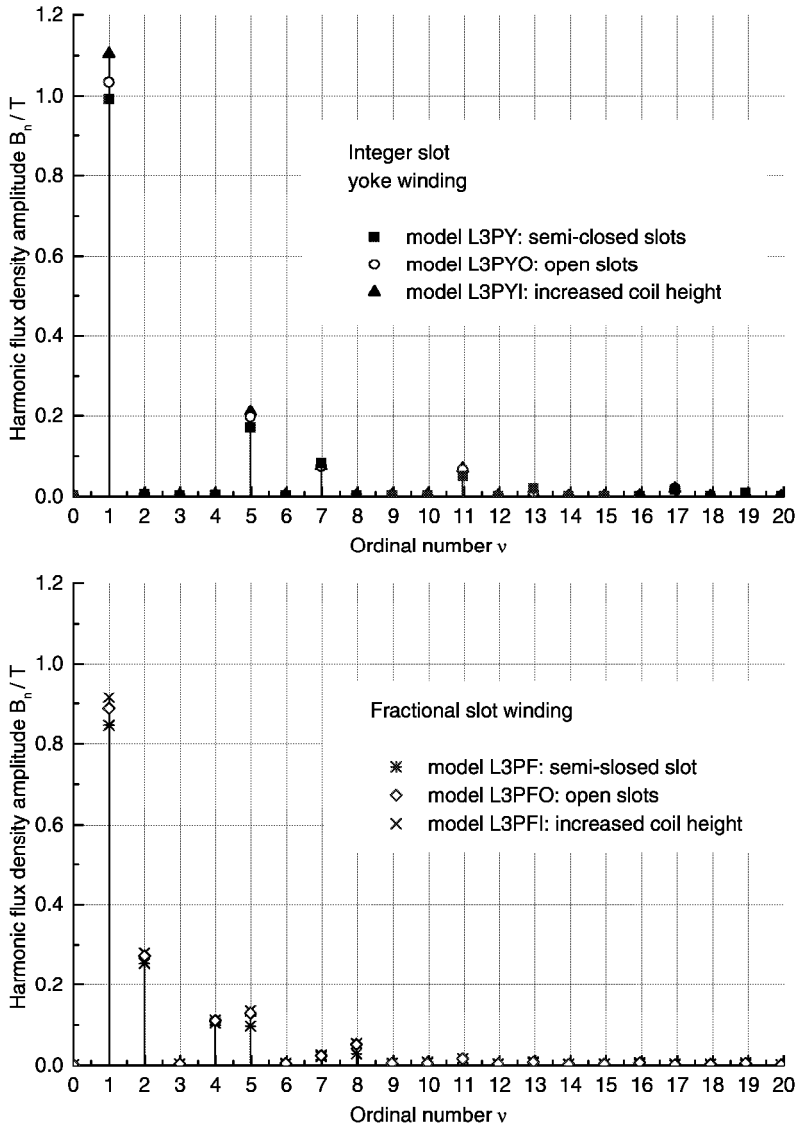


Figure 4.27: Space harmonics of the flux density for the integer slot yoke winding and the fractional slot winding. Data is taken from Figure 4.25 and Figure 4.26.

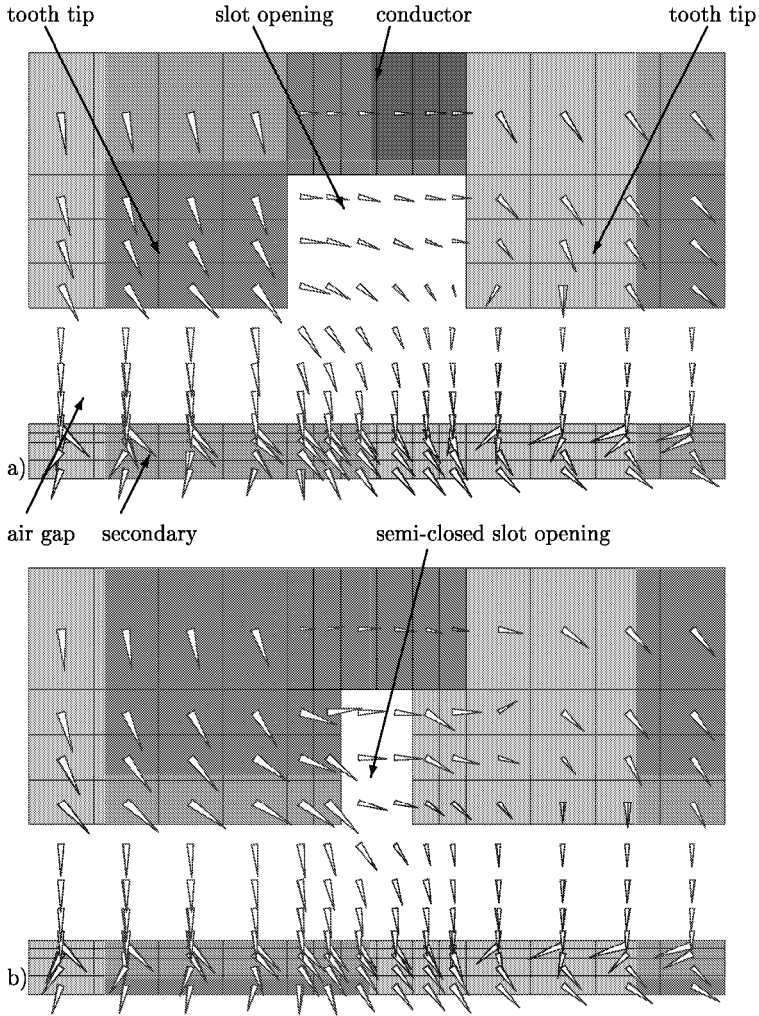


Figure 4.28: Vector plot of the flux density for a) the open slot model L3PYO and b) the semi-closed slot model L3PY at synchronous speed for the same scale and a thermal load of  $A \cdot J = 29060 \text{ A/cm} \cdot \text{A/mm}^2$ . The vector plot is presented for the symmetry plane  $y = 0$ .

### 4.5.5 Power calculation

The electric air gap power  $P_\delta$  has been calculated using coil currents and voltages derived from FE calculations<sup>6</sup>. In the primary part of the FE models, the ohmic load losses of the coils have not been taken into account. Constant losses and additional losses of the primary have been neglected, since the iron core is laminated and it has not been possible to model an anisotropic conductivity. Therefore, the electric input power at the coils of the FE models equals the air gap power.

The power dissipation of the primary winding (ohmic load losses  $P_{cus}$ ) is a constant value which has been calculated analytically. The real input power can be calculated using (4.6), when iron losses  $P_{Fes}$  are neglected.

$$P_{in} = P_\delta + P_{cus} \quad (4.6)$$

Figure 4.29 shows the active and reactive input power in dependence of the slip  $s$  for the eight-pole yoke winding and the fractional slot winding machine.

The reactive power  $Q$  does not change significantly with the change of slot openings. This effect is due to the high coil inductance because of the deep slots (see Figure 4.13).

The input power  $P_{in}$  shows a characteristic curve, similar to the tangential force curve  $F_t$ . Comparing the mechanical power term with the air gap power, it can be pointed out, that the slot closure decreases the power dissipation in the secondary  $P_d$  (4.7) (see Figure 4.30) due to the smaller higher order harmonics of flux density in the air gap. This power dissipation derives from eddy currents<sup>7</sup> in the rail.

$$P_d = P_\delta - P_{mec} = P_{LLr} + P_{Fer} + P_{cur} \quad (4.7)$$

It is also possible to determine the power dissipation in the rail out of the Finite Element models. For low velocities, the values derived from the FE calculations are corresponding to the values calculated with (4.7). For higher velocities, they are not any more in agreement. This is due to the constant mesh of the rail for all velocities. The mesh would have to be refined especially in the rail to obtain an agreement even for high velocity solutions. This was not possible due to hardware limitations.

<sup>6</sup>For the 3-D models, the coils have been modeled independently from the mesh as current forced wire wound coils with ports. When the problem is solved, the current (input) and the voltage can be seen as complex numbers at these ports. This gives the possibility of separating active and reactive power according to (1.27)-(1.29).

<sup>7</sup>In this case, the secondary load losses  $P_{cur}$  are the eddy current losses in the rail due to the missing conductors. The friction and total windage losses are not taken into account.

The fractional slot winding machine causes a higher power dissipation in the secondary compared to the yoke winding machine. This is due to the second and fourth harmonic of the flux density, inducing additional eddy currents in the rail. On the other hand, the yoke winding with its big amount of inactive copper mass causes about 40 kW higher ohmic losses.

The power factor for both winding concepts is shown in Figure 4.31.

It is only shown for the driving slip range. In braking operation, the power factor tends to approach negative values because of the negative input power (regenerative braking).

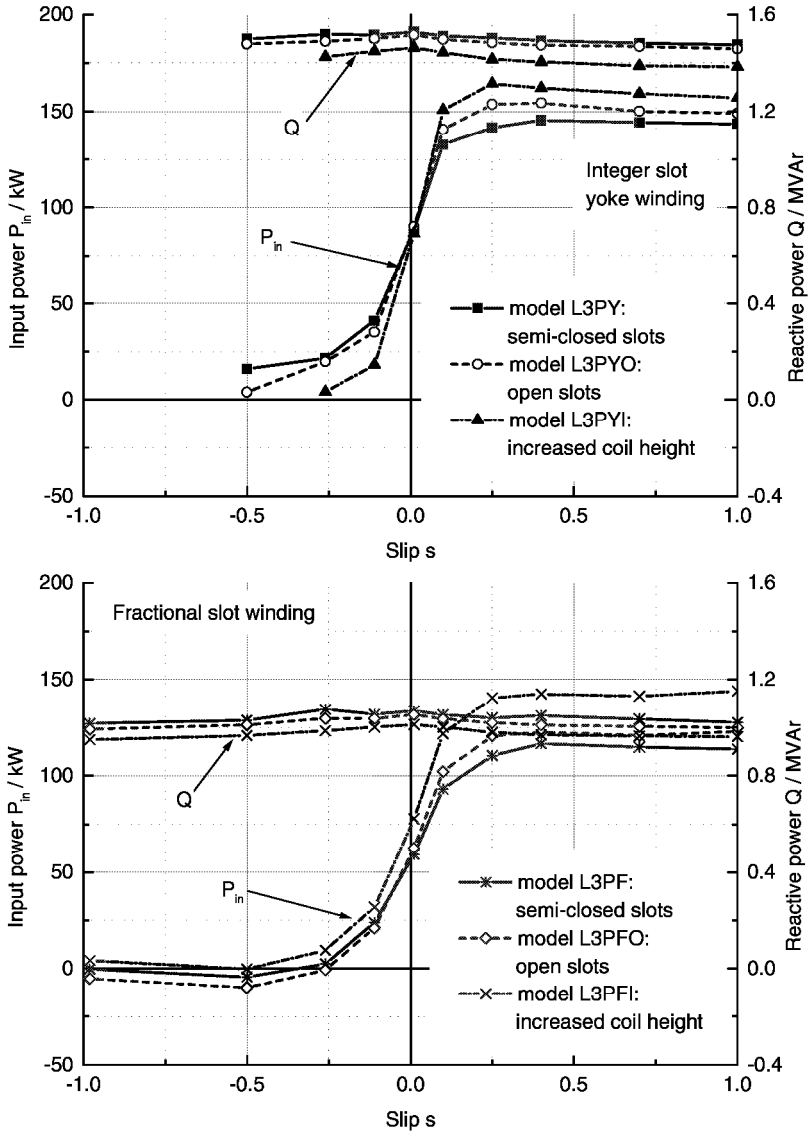


Figure 4.29: Active and reactive input power of one ALIM. Integer slot yoke winding and fractional slot winding. Excitation and parameters according to Table 4.2.  $A \cdot J = 29060 \text{ A/cm} \cdot \text{A/mm}^2$

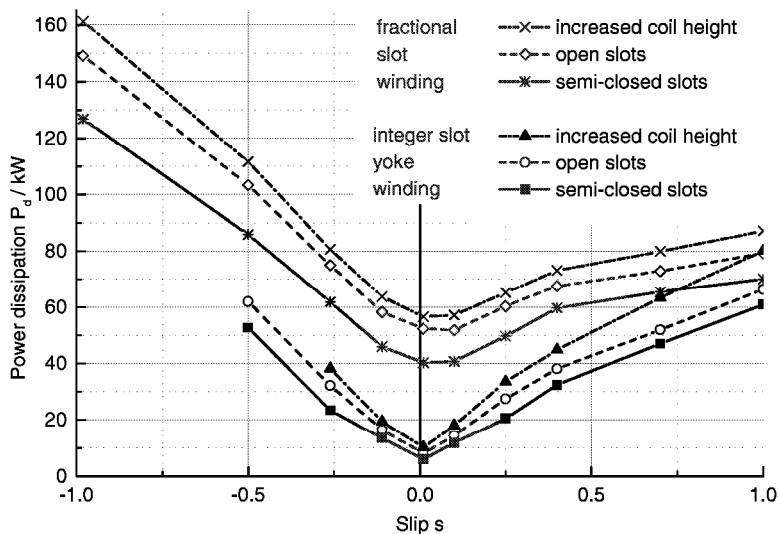


Figure 4.30: Active power losses of one ALIM in the secondary. Comparison of integer slot yoke winding and fractional slot winding. Excitation and parameters according to Table 4.2.

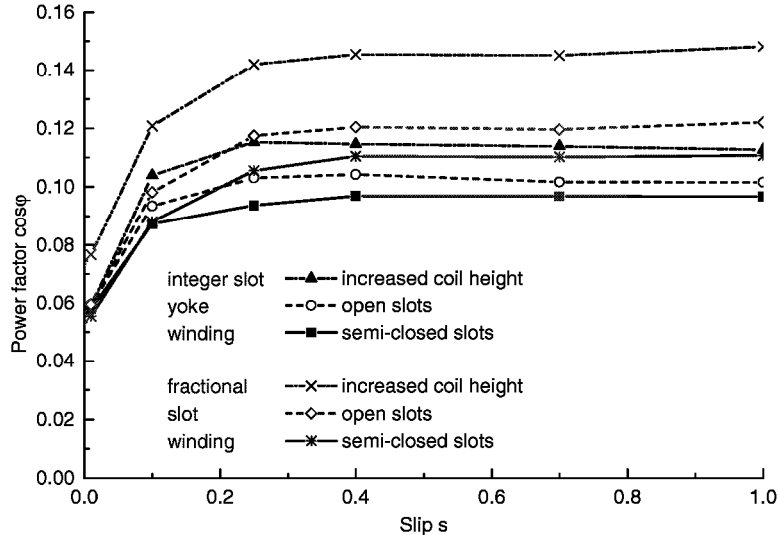


Figure 4.31: Power factor of one ALIM in the secondary. Comparison of integer slot yoke winding and fractional slot winding. Excitation and parameters according to Table 4.2.



## 4.6 Comparison of calculated and measured linear induction machine

### 4.6.1 Comparison of measurement and calculation

The previous chapters have shown that the strong space restrictions of the German railways are not allowing to build a linear induction machine to reasonably enhance the tractive effort of existing locomotives. The forces obtained by those machines are too low to be economically reasonable. Therefore, it was considered not to build a prototype of this machine. Nevertheless, for research demands it is essential to carry out measurements in order to validate calculations. For the first part of this thesis, which is the numerical investigation of the eddy current brake, it was rather simple to compare calculated results with measurements. The device has already been built and put into operation. But for the investigated induction machine, there was no possibility of building a prototype. However, there was a chance to use the eddy current brake of the first high speed train prototype called *ICE-V* to adopt it as a linear induction machine.

Because of the number of teeth equal to six, the eddy current brake was suitable for being transformed into an induction machine with a fractional slot winding. The connection between the coils was opened and rearranged to result in a three-phase system according to chapter 5.2.

Measurements are possible only for fixed primary and secondary. Instead of an inverter, the three-phase sinusoidal supply voltages were taken from a generator with variable frequency. Details of the measurements are discussed in chapter 5.2.

Figure 4.32 shows the comparison of measurement and calculation of the normal and tangential force. The eddy current brake has not been laminated in the primary core. Therefore, a huge amount of eddy currents is flowing in the primary iron which causes a very distinctive skin effect. The utilization of the massive core is inefficient because only its outside skin is effective as a flux conductor [66]. If the iron was laminated, the forces would be much higher, as shown in Figure 4.32 for the calculations with model L3PFδ6L.

The skin effect is shown in Figure 4.33 as a gray scale plot of the flux density and the eddy currents in one tooth of the machine

The skin depth can be calculated analytically by (4.8) and has been compared with the one derived from the numerical calculation.

$$\delta_p = \sqrt{\frac{1}{\pi f_s \mu \kappa}} \quad (4.8)$$

The mean value of flux density in the middle of a tooth in the primary part of model L3PFδ6M is shown in Figure 4.34. The skin depth is defined as the length according to a decrease of flux density of  $1/e$ .

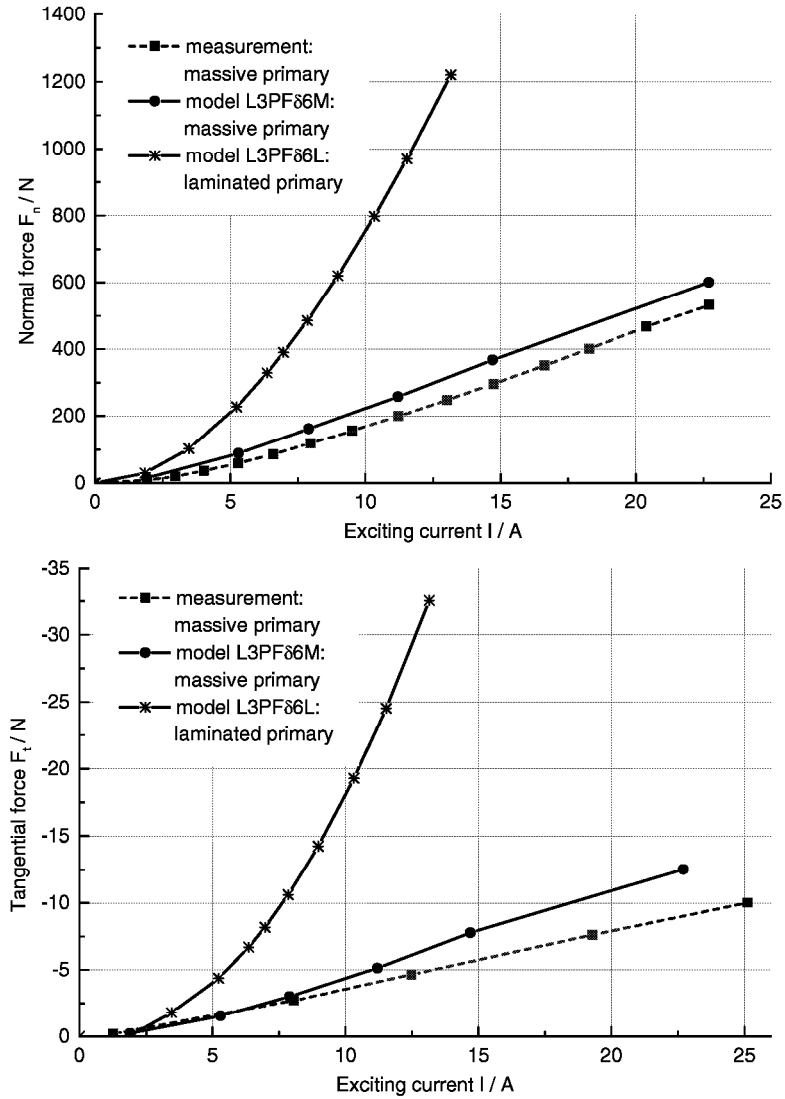


Figure 4.32: Normal (attractive) and tangential force of the linear induction machine. Measurement and calculation results for different excitations at  $f_s = 10$  Hz,  $\delta = 6$  mm,  $\kappa_{prim} = 5 \cdot 10^6$  S/m,  $\kappa_{rail} = 5 \cdot 10^6$  S/m.

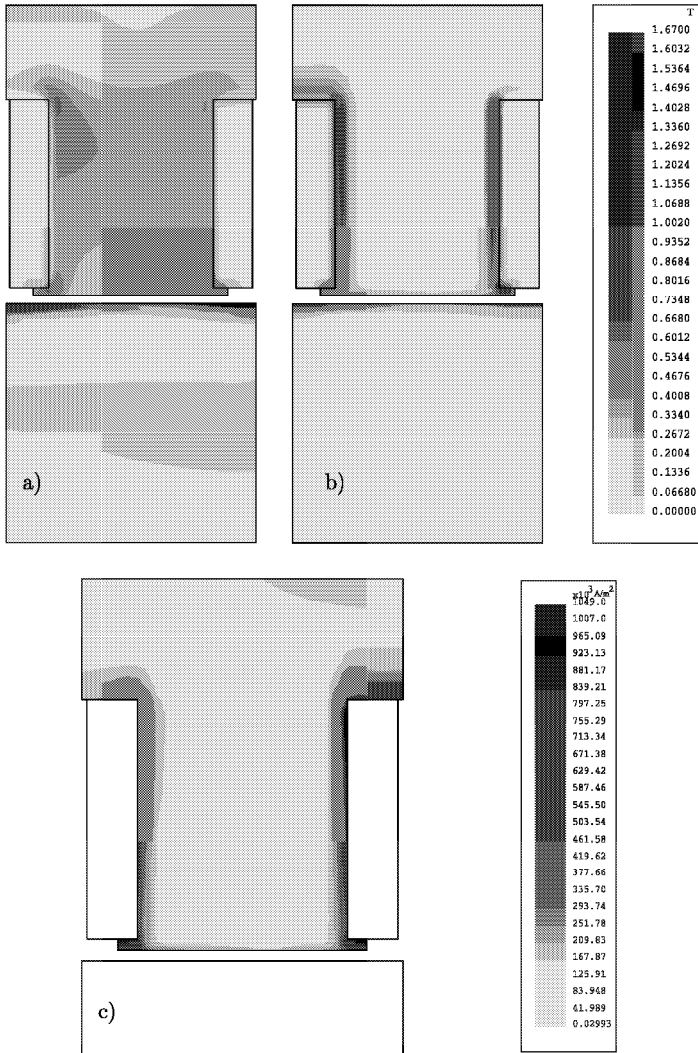


Figure 4.33: Flux density (a+b) and eddy current-density (c) in the symmetry plane of the ALIM with the fractional slot winding. a) primary iron laminated ( $\kappa_{prim} = 0$ , model L3PF $\delta$ 6L), b) and c) primary iron massive ( $\kappa_{prim} = 5 \cdot 10^6 \text{ S/m}$ , model L3PF $\delta$ 6M).  $f_s = 10 \text{ Hz}$ ,  $A \cdot J = 58 \text{ A/cm} \cdot \text{A/mm}^2$ .

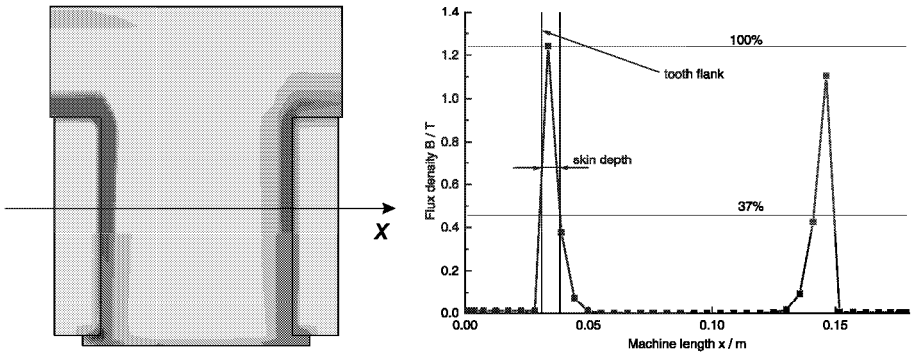


Figure 4.34: Calculation of the skin depth for model L3PFδ6M at  $f=10$  Hz.

The value of skin depth according to the shown characteristic of the flux density is 7.5 mm. If the flux density is expressed with a decaying exponential function as shown in Figure 4.35, there will be a much higher flux density value at the tooth flank. Using this technique, the skin depth is 4.5 mm. For the comparison with the analytical calculation, the relative permeability according to the mean value of the flux density in the range shown in Figure 4.34 and 4.35 is used. Both approaches are listed in Table 4.9.

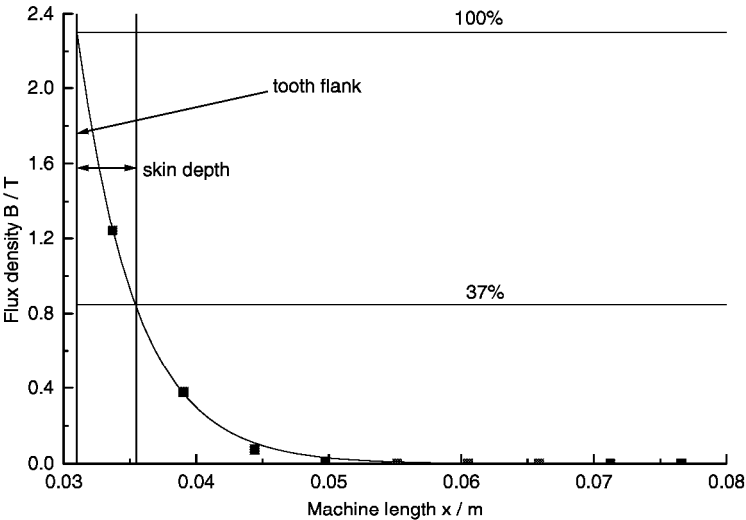


Figure 4.35: Approximation of the flux density as decaying exponential function for model L3PFδ6M at  $f=10$  Hz.

Table 4.9: Skin depth from analytical and numerical calculation.

	$\bar{B}$	$\mu$	$\delta_p$ numerical	$\delta_p$ analytical
Figure 4.34	0.86 T	$1200 \mu_0$	7.5 mm	2.1 mm
Figure 4.35	1.6 T	$300 \mu_0$	4.5 mm	4.1 mm

The flux density in the air gap has been measured at the middle of an inner tooth in the middle of the air gap. The measurement has been compared with the computation result and is shown in Figure 4.36 for  $I = 5.3$  A,  $\delta = 6$  mm,  $\kappa_{prim} = \kappa_{rail} = 5 \cdot 10^6$  S/m.

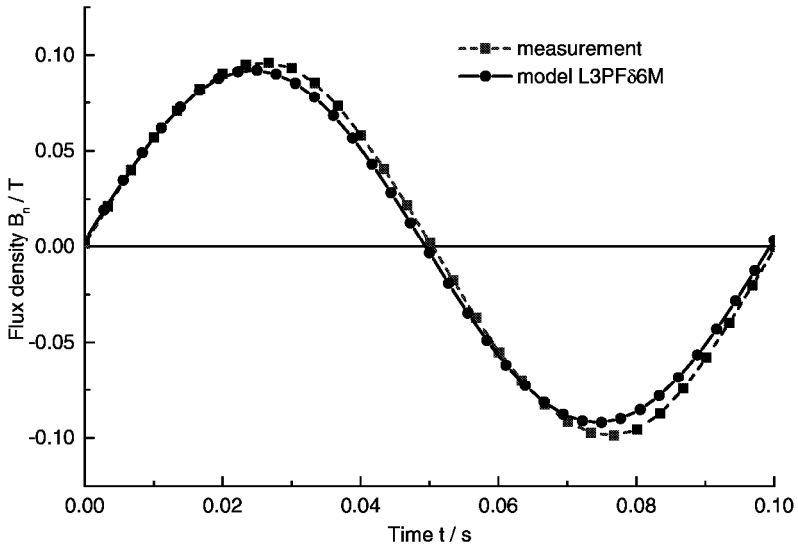


Figure 4.36: Flux density distribution at the primary of the ALIM with the fractional slot winding. For the measurement, the *Hall* probe was fixed in the air gap in the middle of an inner pole. The FE results are taken from the same position. The time shift appears due to a different time instant of measurement and calculation.

The error between measured and calculated values might be included in the choice of material parameters, in the measurement itself or in the Finite Element calculation.

The conductivity of the primary iron is not known. Also the magnetization curves of the primary and the rail are not known exactly. Since the computation of the eddy current brake obtained good results, the magnetization curves might not be the cause of the error. This raises the need to investigate the impact of conductivity variation of the primary on the force generation. This will be shown in the following section. The measurement errors are discussed in chapter 5.

### 4.6.2 Investigation of the impact of conductivity on the calculation results

The conductivity of the iron parts is a sensitive parameter for the calculation. For pure iron, the conductivity has a value of about  $1 \cdot 10^7$  S/m [67]. If there are contaminants in the iron, the conductivity will decrease [68]. It will also decrease when the temperature is increasing. This effect will not be investigated here, because the measurement was performed in a short time (2 s per measurement) with low currents (up to 23 A). This makes it possible to neglect the temperature influence<sup>8</sup>.

The conductivity might decrease to a value of  $1 \cdot 10^6$  S/m if contaminated with Si (Silicon) or Al (Aluminum) [69]. Thus, the range of conductivity variation will be from  $1 \cdot 10^6$  S/m to  $1 \cdot 10^7$  S/m. Figure 4.37 shows the flux density for different conductivities of the primary iron. The conductivity of the rail is  $\kappa_{rail} = 5 \cdot 10^6$  S/m. The impact of conductivity variation on the calculated forces is shown in Figure 4.38.

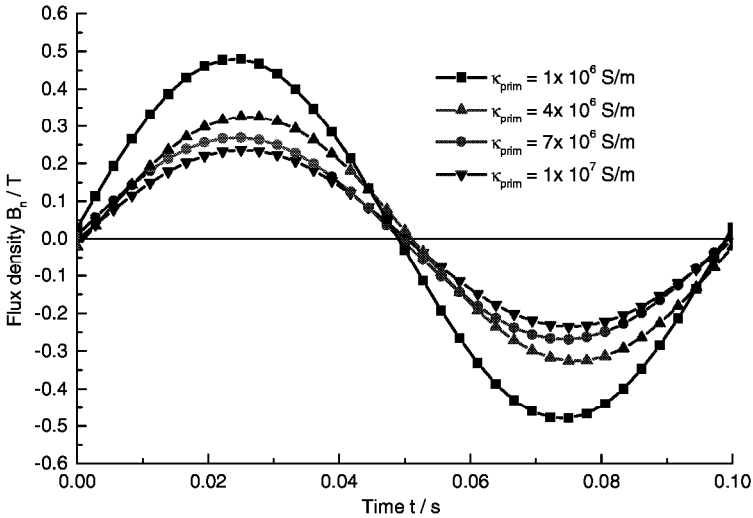


Figure 4.37: Impact of conductivity variation on the flux density in the air gap. The values are derived for a position according to Figure 4.36 in the air gap in the middle of an inner pole. The curves have been calculated with a fixed conductivity of the secondary part  $\kappa_{rail} = 5 \cdot 10^6$  S/m, while the conductivity of the primary part has been varied.  $A \cdot J = 958$  A/cm  $\cdot$  A/mm<sup>2</sup>,  $I = 32$  A,  $\delta = 6$  mm.

<sup>8</sup>There has been a measurement of temperature rise of the linear machine. For a current of 150 A, the temperature rise was 0.3 K/s. Since the temperature rise is proportional to the square of the current, the maximum temperature rise for the actual measurement is estimated to be 0.012 K/s.

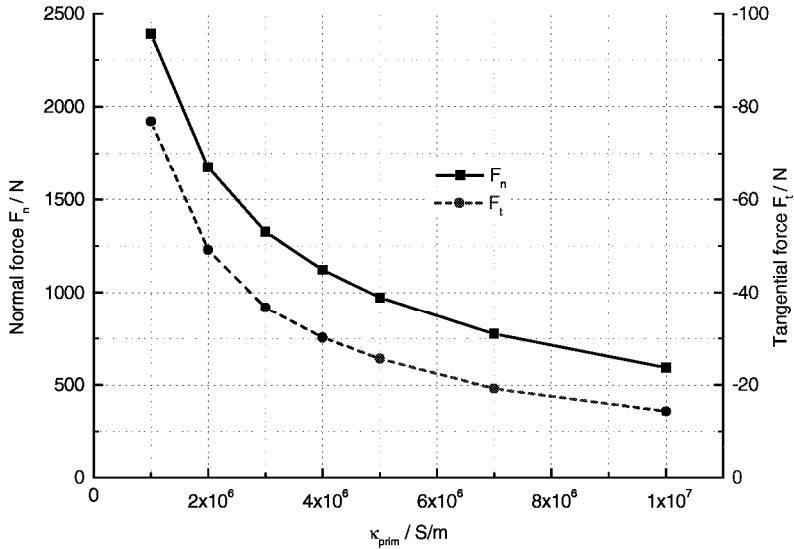


Figure 4.38: Impact of conductivity variation on the calculated forces. The curves have been calculated with a fixed conductivity of the secondary part  $\kappa_{rail} = 5 \cdot 10^6 \text{ S/m}$ , while the conductivity of the primary part has been varied.  $A \cdot J = 958 \text{ A/cm} \cdot \text{A/mm}^2$ ,  $I = 32 \text{ A}$ ,  $\delta = 6 \text{ mm}$ .

Both force components and the flux density are decreasing with increasing conductivity. It is not proposed to increase the conductivity of the primary iron in the FE-models in order to obtain a better coincidence between the measured and calculated forces. This would lead to a bigger difference between the flux densities. Therefore, the optimum coincidence seems to be found and the remaining differences might be explained with the following items:

- The 3-D mesh is too coarse to give an exact result for the skin effects in the primary part.
- The holes in the primary part, where the coils are connected are causing an additional flux concentration in the yoke of the primary part. This is not considered in the calculations. Therefore, the calculated forces are too high (5% in the 2-D model).
- The connection between teeth and yoke might act like an additional air gap on the flux. This would also cause lower measured forces.
- The force transducer does not measure exactly half of the real force. Therefore, the real forces would be slightly bigger (10%) than measured.

## **4.7 Concluding remarks to the calculation of the linear induction machine**

In this chapter, two different designs of the linear induction machine have been presented. First, the fractional slot winding design has been investigated. Its advantage is the compact winding with small winding overhangs and no crossing of phases. Unfortunately, its performance is not as good as expected before. The low obtained forces at high currents, low power factor and the high dissipation power are disadvantageous to an economical application in the railway system. The second design, which is the integer slot yoke winding served as a comparing design for the fractional slot winding. Therefore, its geometrical and electrical parameters have not been optimized to obtain maximum forces, but designed to suit the geometrical parameters and the thermal load of the fractional slot winding design. Compared with the fractional slot winding, the integer slot yoke winding will generate higher forces. If the design is optimized for maximum forces, there might be an additional increase of force generation. But this increase will likely be only some percents of the present results. The slots would have to be redesigned in order to keep the first and second order skin effect as small as possible. This would affect the power dissipation in the primary and the power factor. There might be an increase of both, but this would probably not be sufficient for considering the application in the railway system.



# Chapter 5

## Measurements

In the preceding chapters, measurement results have been shown and compared with numerical calculations. In this chapter, the measurement devices, conditions and problems will be presented.

The measurements were performed for a velocity of  $v = 0$  m/s for primary and secondary part. They were done at the laboratory of the Institute of Electrical Energy Conversion of the University of Technology Darmstadt. For collecting the measurement data, a computer-based measurement software (*DMCLABplus* [70]) was used. The data was transformed for the computer by a measurement transducer.

### 5.1 Measurements with the DC eddy current brake

#### 5.1.1 Experimental set-up of the measurement

The German railway company *DB AG* has provided a DC eddy current brake from the train *ICE-V* for these measurements. Figure 5.1 shows the test rig in the laboratory.

The eddy current brake is fixed on the left side and connected to a force transducer on the right side to measure the attractive force for different air gaps. The normal air gap flux density distribution  $B_n(x)$  was measured with a *Hall* probe.

The air gap can be adjusted on both sides with adjustment mechanisms using bolts like shown in Figure 5.1. The linear machine is centered over the rail.

The electric circuit diagram of the measurement set up with the eddy current brake is shown in Figure 5.2.

The terminals 9 to 12 of the test rig are connected to the *Ward-Leonard* system, which generates a nominal DC current of 418 A and a nominal DC voltage of 230 V. The *Ward-Leonard* system is a set of an induction machine coupled on both sides with two DC machines. The induction machine runs as a motor and produces the mechanical power. The DC machines are connected to a controller, which controls the excitation. Depending on the excitation, the armature generates a variable DC current and voltage. This supply feeds the eddy current

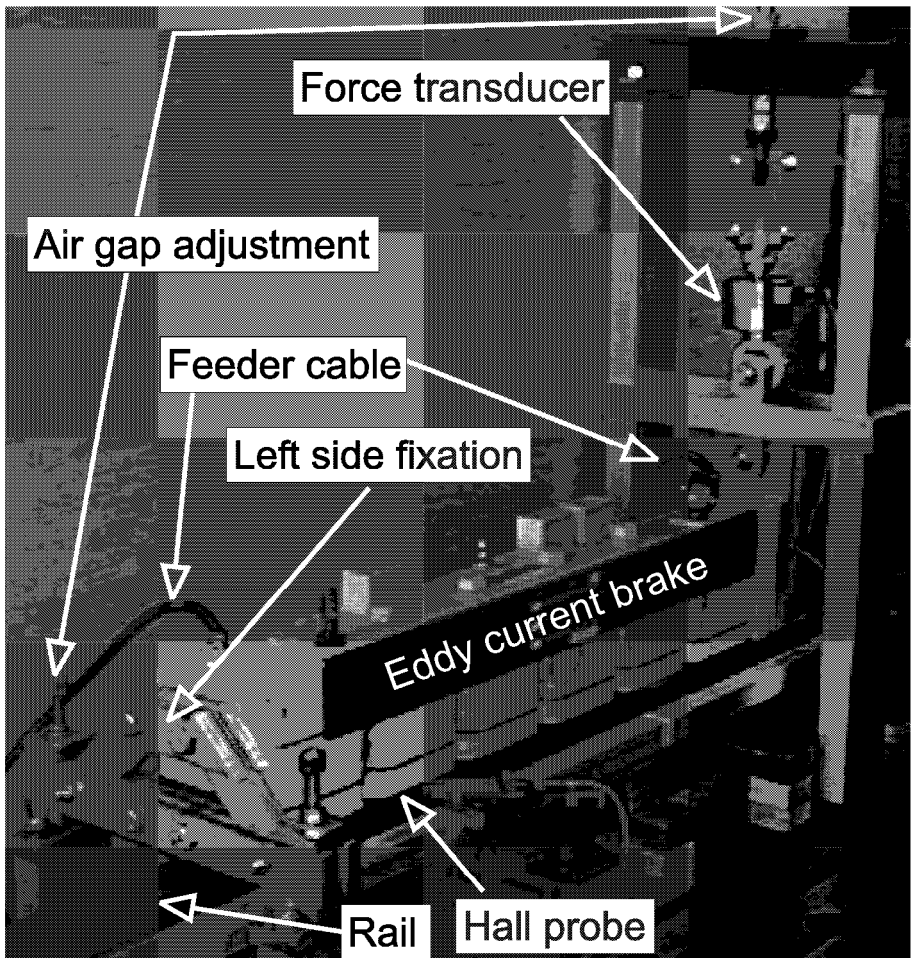


Figure 5.1: Test rig of the eddy current brake. The main components of the test rig are indicated with arrows and descriptions.

brake. For safety aspects, the machine will be disconnected automatically in case of a failure mode (short circuit, voltage drop). Several lamps are indicating the mode of operation. With the setpoint setter at the test rig, the controller is supplied with the setpoint value of supply current for the eddy current brake. The controller controls the field excitation of the *Ward-Leonard* system. To prevent a polarity reversal of the supply voltage at the linear machine, a diode is used.

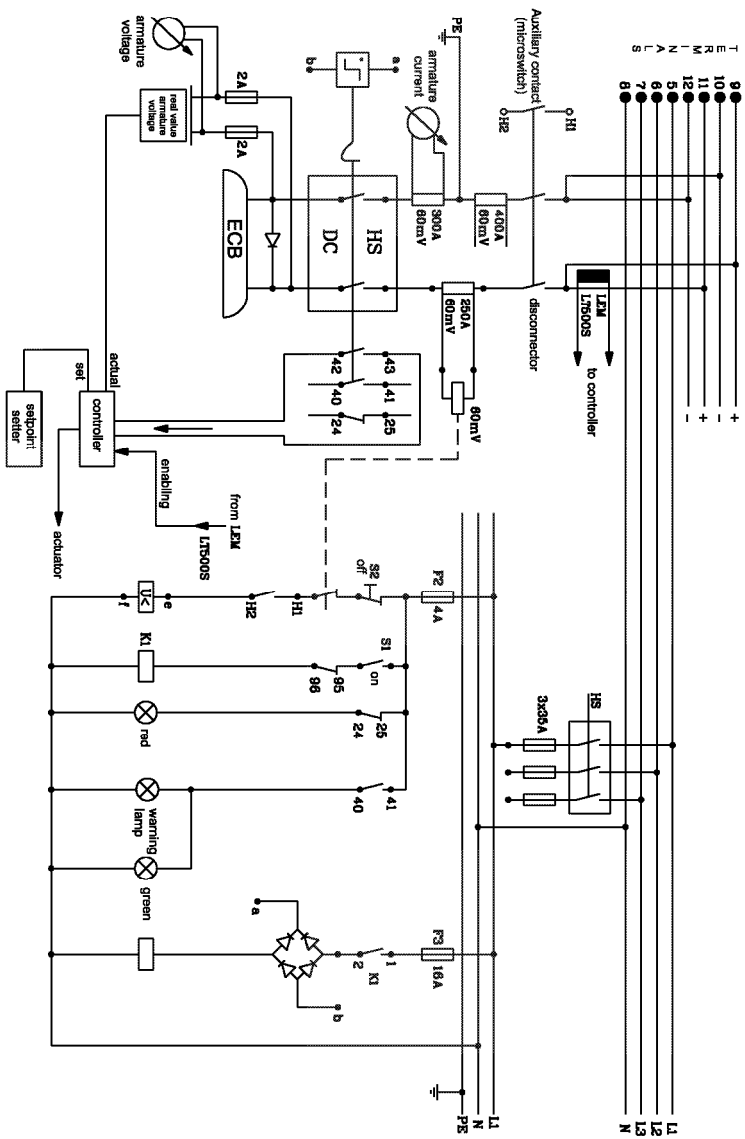


Figure 5.2: Circuit diagram of the eddy current brake (ECB).

### 5.1.2 Measurement results

The measurements were performed with different exciting currents and different air gaps. The temperature has been observed to prevent any overheating damage.

The result of the measurement of normal force for different air gaps and different exciting currents is shown in Figure 5.3. The normal force value is depending on the air gap height. The smaller the air gap, the higher the normal force. The nonlinearity of the iron can be seen at the characteristic curves of the force with increasing current. The nonlinearity can be observed clearly at an air gap height of 6 mm. For very big air gaps, the influence of the primary part properties is reduced. Therefore, the nonlinearity does not appear to be very strong at 18 mm air gap.

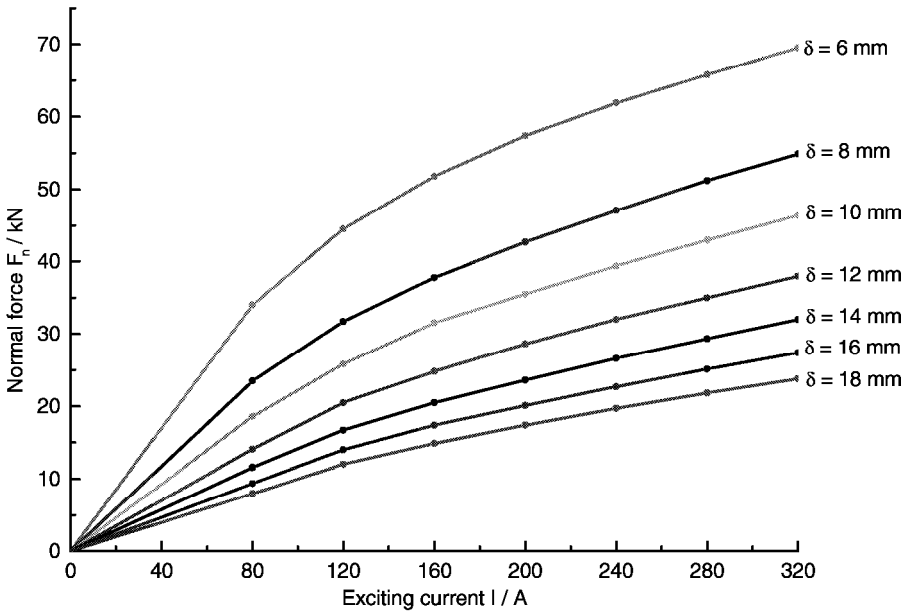


Figure 5.3: Measured normal force of the eddy current brake at different air gap heights and exciting currents. The nonlinearity of the iron can be seen at the characteristic curves of the force with increasing current. The normal force value is depending on the air gap height. The smaller the air gap, the higher the normal force.

The measured flux density distribution is shown in Figure 5.4. Only the first three poles were measured due to the symmetry of the six-pole eddy current brake. The air gap height equals 10 mm and the exciting current has been varied from 10 to 40 A. The iron is not

saturated at the measurement, because the flux density peaks are increasing linear with rising excitation current.

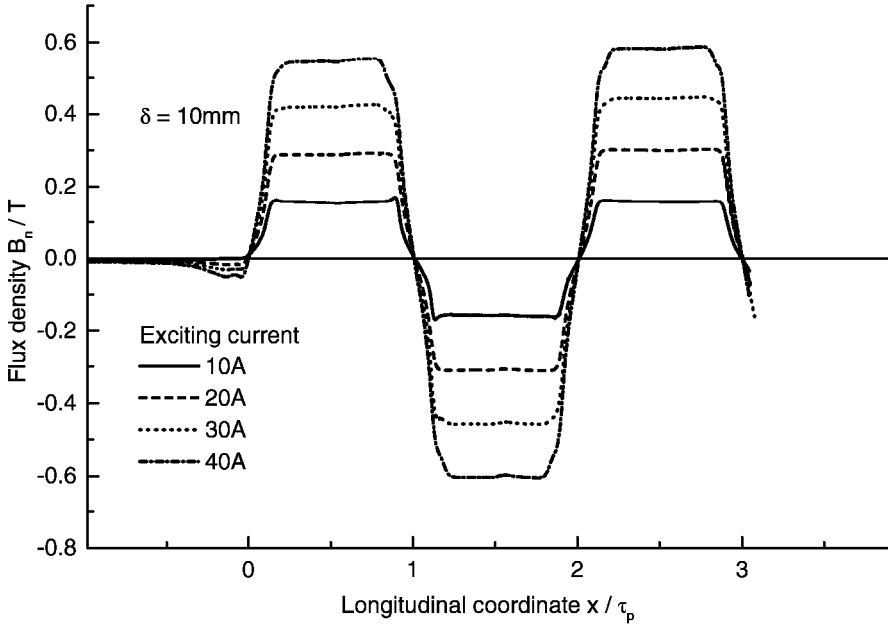


Figure 5.4: Measured flux density distribution of the eddy current brake in the air gap. The air gap height equals 10 mm and the exciting current has been varied from 10 to 40 A. The first pole starts at  $x = 0$ . The small pole at negative  $x$ -values represents an end pole which results from the unexcited iron next to the first pole. Only the first three poles were measured due to the symmetry of the six-pole eddy current brake. The iron is not saturated at the measurement. The flux density peaks rise linear with rising excitation current.

## 5.2 Measurement with the AC linear induction machine

For this kind of measurement it was necessary to have a linear machine which could be connected to a three phase system resulting in an even number of poles. For this requirement, it was possible to use the eddy current brake which has already been tested and which was mounted in the laboratory. Assuming a fractional slot winding with the number of slots per pole and phase of  $q = 1/2$ , the eddy current brake with six poles could be transformed into an AC machine with four poles. Figure 5.5 shows this principle. Thus, a linear induction machine with massive primary has been available for measurements.

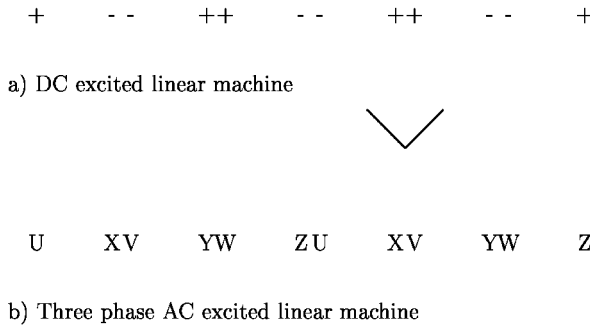


Figure 5.5: Transformation from DC to AC excitation of the eddy current brake. The connections between the coils of the eddy current brake were opened and the coils were connected separately to a three-phase system. The number of poles changed from 6 to 4.

### 5.2.1 Experimental set-up of the measurement

For measuring the forces of the linear induction machine with massive iron, two force transducers were used. One of them was used to measure the normal force and the other to measure the tangential force. The principle of mounting the force transducers is shown in Figure 5.6.

Additionally, three current transformers were used, one for each phase. The whole circuit diagram of the test rig is shown in Figure 5.7, whereas a photograph of the test rig can be seen in Figure 5.8.

The linear machine has been supplied with a three phase current from a wound-rotor induction machine, which generates a three-phase voltage system of variable amplitude and frequency.



Figure 5.6: Principle of mounting the force transducers in the test rig.

According to [19], the rotor frequency of a wound-rotor induction motor can be expressed as

$$f_r = \frac{n_{syn} - n}{n_{syn}} f_s \quad (5.1)$$

where  $n_{syn}$  is the synchronous speed of the magnetic field, given by (5.2),  $n$  is the speed of the rotor,  $p$  the number of pole pairs of the induction machine and  $f_s$  the electrical frequency of the stator.

$$n_{syn} = \frac{f_s}{p} \quad (5.2)$$

The rotor winding of the wound-rotor induction machine was connected via sliprings to the test rig to supply a three-phase current in the winding of the primary of the ALIM. By changing the rotor speed, the frequency of the ALIM primary current could be regulated. To obtain a constant rotor speed, the induction machine was connected mechanically to a DC machine which was regulated by a controller. The DC machine itself was excited by a constant DC current and the armature was supplied with energy from a regulated *Ward-Leonard* system. The exciting voltage of the wound-rotor induction machine was generated by a rotary regulator.

With the wound-rotor induction machine as generator, the actually supplied current was an excellent sinewave (see chapter 5.2.2).

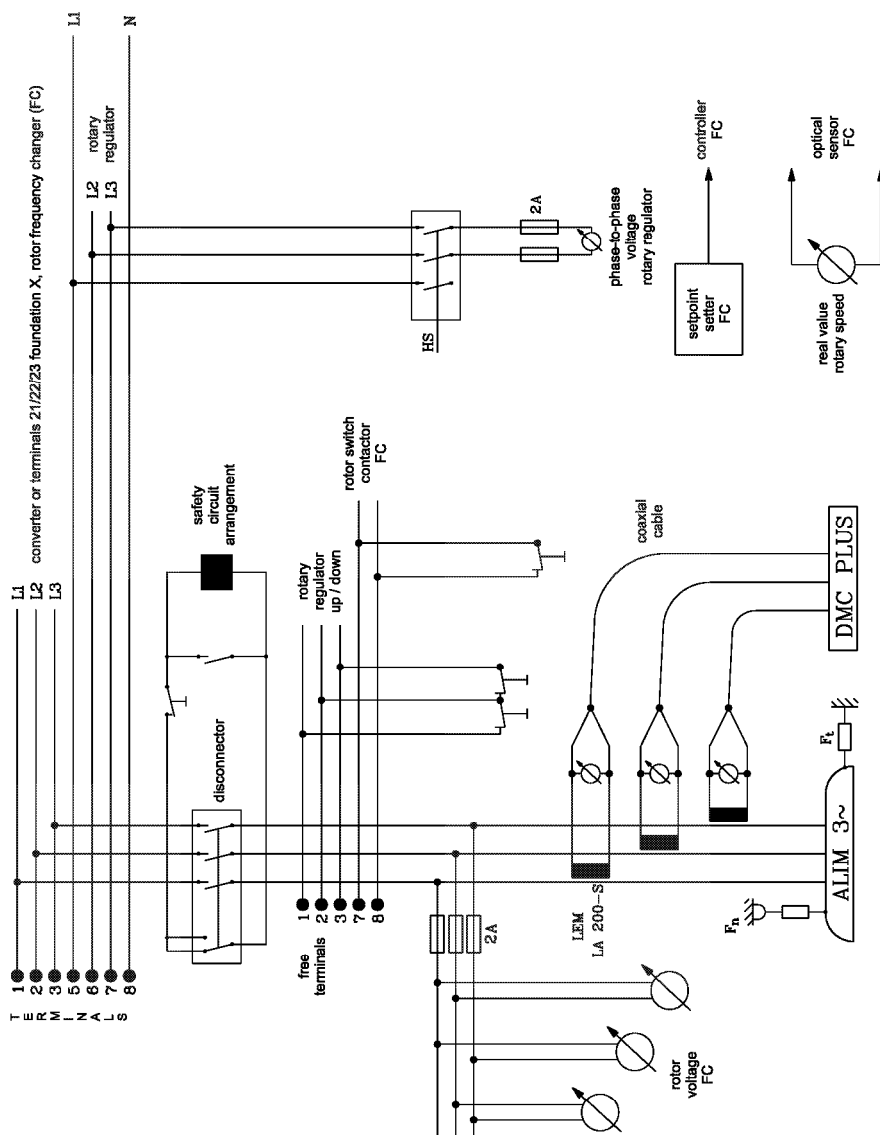


Figure 5.7: Circuit diagram of the ALIM test rig.



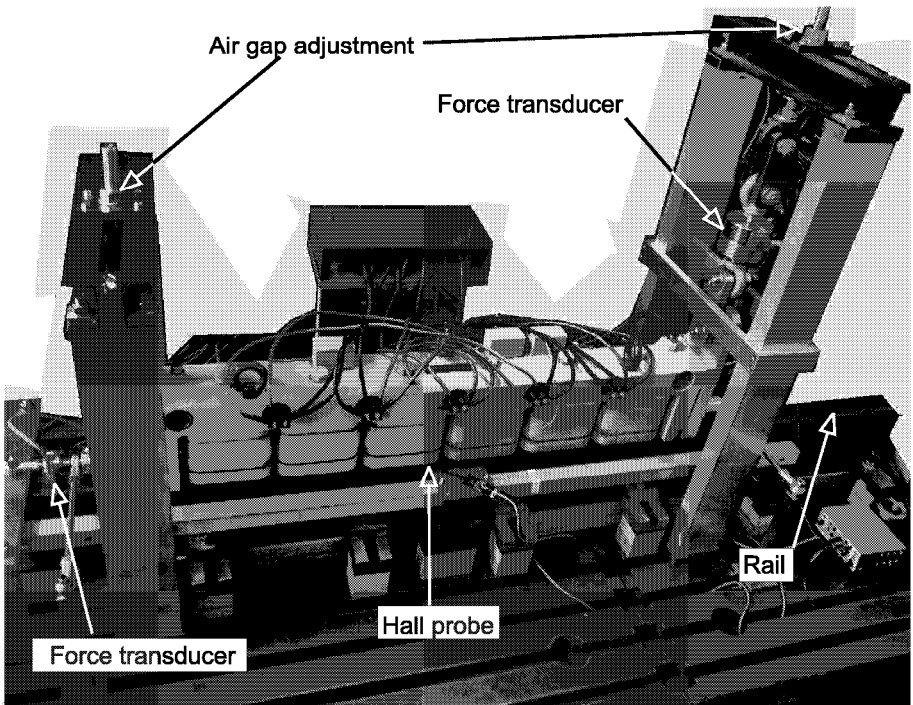


Figure 5.8: Photograph of the ALIM test rig.

### 5.2.2 Measurement results

The measurement was performed at different amplitudes of primary current. One typical excitation is shown in Figure 5.9. There are the three-phase currents with a frequency of 10 Hz.

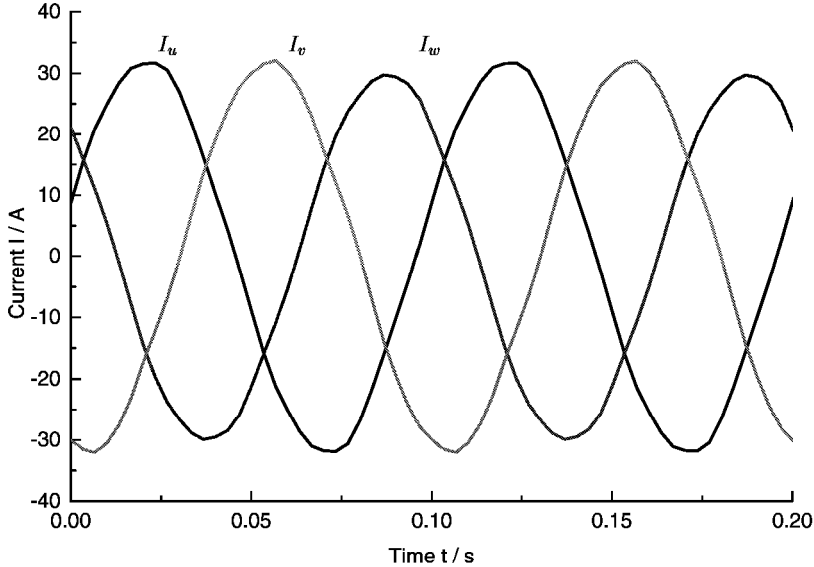


Figure 5.9: Three-phase currents flowing in the winding of the primary of the ALIM.

The forces generated by these currents are shown in Figure 5.10. They are both oscillating around the mean value, which has been taken for the comparison with the calculation.

It is obvious, that the second harmonic is distinct in the normal force component. This will be proven by a *Fourier* analysis.

Looking at the time harmonics of the normal and tangential force components in Figure 5.11, one can see, that the second harmonic with the frequency 20 Hz is the most dominating frequency in both force components.

This is due to the principle of force generation. As shown in (1.37), the normal force component is generated by the flux density squares. This means, that a sinewave is squared as shown in (5.3).

$$\sin^2(\omega t) = \frac{1}{2}(1 - \cos(2\omega t)) \quad (5.3)$$

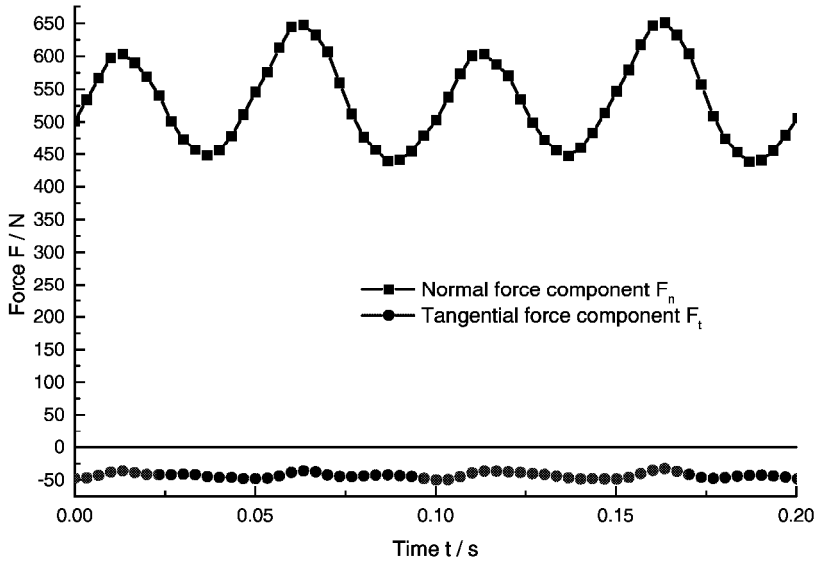


Figure 5.10: Force components of the measurement with the fractional slot winding linear induction machine. The frequency of the three-phase current in the primary winding is 10 Hz. The three-phase current is shown in Figure 5.9.

In totally symmetric rotating machines, this alternating component cannot be measured on the secondary. This is because there is always a counterpart (a pole with the same orientation on the opposite side of the rotor), which is pulling into the opposite direction. For linear machines, there is no counterpart and thus, the second harmonic component must appear.

For the tangential component, there is a multiplication of sinewaves like shown in (5.4).

$$\sin(\omega t) \cdot \sin(\omega t + \varphi) = \frac{1}{2}(\cos \varphi - \cos(2\omega t + \varphi)) \quad (5.4)$$

In a totally symmetric machine, the alternating component of the force is extinct due to the superposition of the three phases. In the measurement, the currents are not exactly symmetrical (see Figure 5.9). This imposes an unsymmetric field and thus the appearance of the harmonics shown in Figure 5.11. The mechanical behaviour of the guiding structure supports the appearance of the higher time harmonics. This could be observed when the linear machine is excited mechanically using a hammer-blow. Then natural frequencies shown in Figure 5.12 appeared.

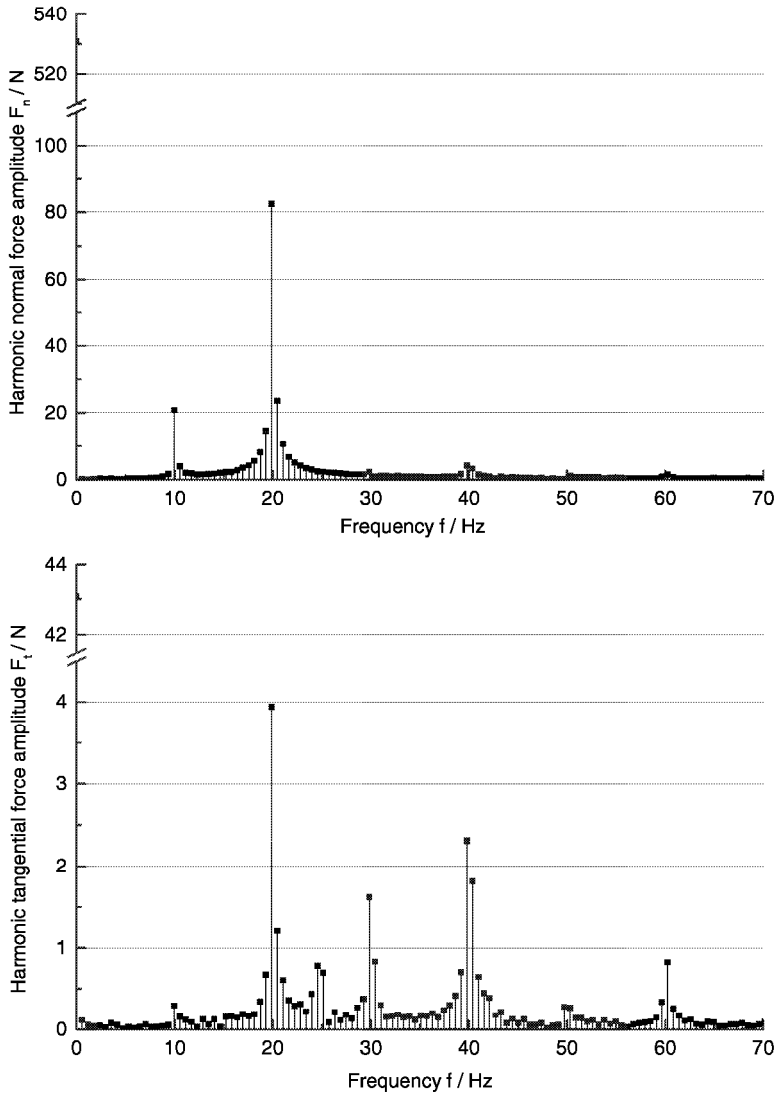


Figure 5.11: Harmonics of the normal and tangential force component of the measurement with the fractional slot winding linear induction machine. The primary frequency is 10 Hz. The three-phase primary current is shown in Figure 5.9.

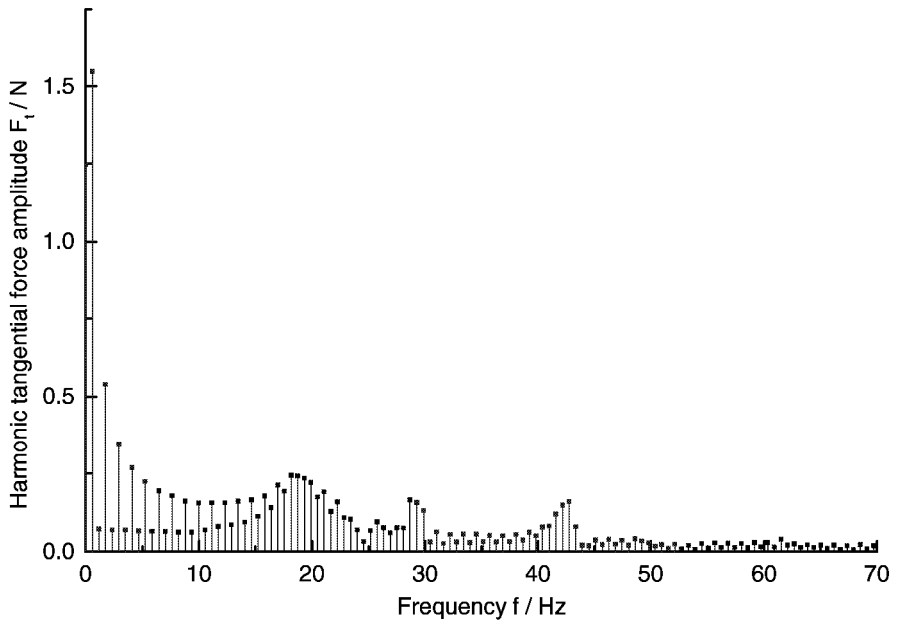


Figure 5.12: Natural frequencies of the tangential force component of the guiding structure of the fractional slot winding linear induction machine test rig. Mechanical excitation with a hammer-blow.

### 5.3 Measurement of the rail conductivity

The conductivity of the magnetically active parts of the linear machine is a vital parameter as shown in chapter 4.6. The conductivity of the primary part of the linear machine could not be measured without destroying the machine. This was not intended and therefore the conductivity of the primary part was not measured. The secondary part, which is the iron rail, has been available for measurements. From a *UIC60* rail head, a small cuboid has been separated with a length of  $l = 100$  mm and a square cross-section with  $A = 100$  mm<sup>2</sup>. The measurement of the conductivity was performed with a *Thomson Bridge*. Figure 5.13 shows the arrangement.

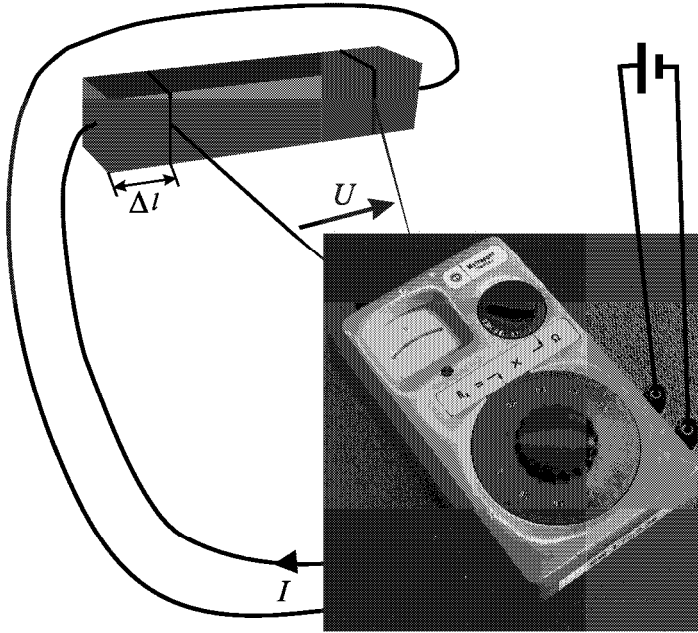


Figure 5.13: Arrangement of the conductivity measurement for a piece of rail.

To avoid errors due to a fringing effect of the current paths in the sample, the voltage measurement was fixed in a distance of  $\Delta l = 10$  mm on both sides. The current supplying conductors were attached directly to the ends of the probe. With this arrangement, it was possible to measure the resistance of the piece of metal within the voltage terminals with a precision of 4 % according to the manufacturer.

The result of the resistance measurement gave a value of  $R = 0.175$  m $\Omega$ . Using (5.5), the conductivity could be calculated to  $\kappa = 4.57 \cdot 10^6$  S/m.

$$\kappa = \frac{l - 2 \Delta l}{R \cdot A} \quad (5.5)$$

Due to the error of the measurement, the resistance value might differ between  $4.39 \cdot 10^6$  S/m and  $4.75 \cdot 10^6$  S/m. The measured value validates the approximate value of rail conductivity of  $5 \cdot 10^6$  S/m which has been chosen for the calculations.

## 5.4 Measurement fault detection

It is impossible to perform measurements without having measurement errors. Possible errors are due to different mechanisms and conditions. In this chapter, the main errors for the performed measurements should be presented. The classification of measurement errors can be based on their cause or on their properties. Here, measurement errors should be classified by their cause, since this classification suits the character of the measurement.

- Methodological errors can arise as a result of an inadequate theory of the phenomena on which the measurement is based and inaccuracy of the relations that are employed to find an estimate of the measurable quantity [71]. Methodological errors could be found in the measurement of the flux density. The error of this measurement is very hard to estimate. It is an addition of methodological, instrumental and personal errors.
- Instrumental errors are caused by the imperfection of measuring instruments. For this measurement, the errors can derive from the force transducers and the measurement transducer for the computer. The maximum error of the force transducers is 2 % according to the manufacturer.
- The individual characteristics of the person performing the measurement give rise to individual errors that are characteristic of that person. In this measurement, personal errors can be excluded. There is a variety of analogous measurement devices which have to be read personally, but they are only for supervising means. The collection of measurement results has been performed with a measurement transducer and a computer-based measurement software and therefore underlies no personal errors.

# Chapter 6

## Summary and Conclusions

Supported by the German railway company *Deutsche Bahn AG* an investigation on the application of linear induction motors for railway systems has been carried out. The main task was to develop a machine with additional features to the braking capability of the eddy current brake which is already in operation with the German high-speed train *ICE 3*. The new booster should be able to get similar braking forces as the eddy current brake and furthermore, it should be possible to obtain attracting, braking and accelerating forces independently from each other and from the train speed. To fulfill these requirements, a frequency inverter is needed to control the mode of operation of the asynchronous machine.

Since the linear induction machine (ALIM) should be mounted on the bogie of existing locomotives, it is necessary to stay within the limits which are demanded by *EBO* [36] regulations. Therefore, the space available for mounting the ALIM is very small. So the design of the ALIM has to take into account the small space by applying special features.

A linear induction machine with different coil and slot geometries has been investigated. The design has been optimized to fit into the bogie of a locomotive. Two different approaches have been compared using the mechanical forces, the flux density distribution including a *Fourier* analysis and the power components.

In order to realize short winding overhangs and to avoid crossing of phases, a fractional slot winding with the number of slots per pole and phase  $q = 1/2$  and an integer slot yoke winding with  $q = 1$  was chosen for investigation.

With the fractional slot winding, a considerable amount of higher space harmonics is generated, which reduces the driving and increases the braking force of the ALIM. Mainly the 2nd and 4th order harmonic contribute to this effect.

The integer slot yoke winding yields higher forces than the fractional slot winding. According to [72], the closing of the slots leads to a higher slot leakage reactance which obviously reduces the forces of the machine. Power dissipation in the secondary as well as force generation is reduced by decreasing the slot opening. An increased coil height is apparently the best design regarding to force generation, but due to the vertical field in the slots, the losses in the top conductors will be higher than presented in this thesis [65].



Using the yoke winding machine, the traction motors of the locomotive *BR152* can be supported with an increased tractive effort of 6 to 12% and an additional braking force of 7 to 13%. There is also the possibility to use the inverters of the drive motors (if the power reserve of the inverters is big enough) and to reduce the weight of the locomotive. In this case, the slip of the linear machine would be fixed by the slip of the drive motors. This would reduce the costs and increase the additional tractive effort and braking force, but it would also remove the independence of the linear machine.

Considering the weight of the linear machine and the fixation structure, the additional converter, the water cooling system and the high active and reactive power, there will be other systems yielding comparable driving and braking forces with fewer costs than the ALIM.

The calculated results show that the large air gap and the restricted space for the primary part reduce the ALIM booster performance drastically, in spite of elaborate cooling conditions. Further, one has to consider the additional mass and costs for the inverter and the cooling pump. So, linear boosters with the rail as secondary have a rather limited force support for electric locomotives under the above mentioned, restrictive boundary conditions.

For an improved design, the following conditions should be reached:

- Increasing the available space for the linear machine, mainly perpendicular to the direction of motion. This would allow a better utilization of the linear machine.
- Decreasing the air gap between linear machine and rail. This could drastically reduce the reactive power consumption. Furthermore, the forces would be increased.
- Improving the electromagnetic properties of the rail. A different magnetization curve would obtain higher flux density values and thus higher forces. A copper cage in the rail profile would lead to a concentration and guidance of the eddy currents. This would reduce interfering forces and would probably also increase the booster performance.

The changes postulated above are not practicable in the German railway system. The available space could only be increased by building new bogies and removing several devices from the track. The air gap could only be decreased by a extremely expensive guidance structure for the linear machine. It would be possible to build a rail with a different magnetization curve and a copper cage, but it would be extremely expensive.

A linear induction machine with the rail as secondary, regardless of the design, is therefore not an economically useful device for the application in existing locomotives. In future, new designed bogies with enough space for a well designed linear machine may yield ALIM solutions with an increased force generation.

# List of Symbols and Abbreviations

SYMBOL	UNIT	NAME
$a$		Number of parallel wires
$A$	A/m	Current-sheet
$A$	m <sup>2</sup>	Cross-section
AC		Alternating current
ALIM		(Asynchronous) linear induction machine
$A_m$	Vs/m	Magnetic vector potential
$A_{mz}$	Vs/m	Magnetic vector potential in $z$ -direction
$b_c$	m	Width of active copper in the slot
$b_s$	m	Width of the slot
$B$	T	Magnetic flux density
$B_n$	T	Normal component of flux density
$B_t$	T	Tangential component of flux density
$d$		Derivative symbol
$D$	As/m <sup>2</sup>	Electric flux density (electric displacement)
DC		Direct current
e.m.f.	V	Electromotive force
$\vec{e}_x$		Unit vector in $x$ -direction
$\vec{e}_y$		Unit vector in $y$ -direction
$\vec{e}_z$		Unit vector in $z$ -direction
$E$	V/m	Electric field (strength)
ECB		Eddy current brake
$E_z$	V/m	Electric field (strength) in $z$ -direction
$f$	Hz	Frequency
$f_n$	N/m <sup>2</sup>	Normal force density
$f_t$	N/m <sup>2</sup>	Tangential force density
$f_x$		Adhesion coefficient
$f_s$	Hz	Primary frequency
$f_r$	Hz	Secondary frequency
$F$	N	Force

FE		Finite Element
$F_n$	N	Normal force component
$F_t$	N	Tangential force component
$g$	m/s <sup>2</sup>	Gravitational constant ( $g = 9.81$ m/s <sup>2</sup> )
$h_i$	m	Height of cooling duct
$h_o$	m	Height of conductor
$H$	A/m	Magnetic field (intensity)
$I$	A	Primary current (r.m.s.) phase value
$\hat{I}$	A	Primary current amplitude
$I^*$	A	Primary current conjugate complex
$I_a$	A	Primary current of phase a
$I_b$	A	Primary current of phase b
$I_U$	A	Primary current of phase U
$I_V$	A	Primary current of phase V
$I_W$	A	Primary current of phase W
$j$		Imaginary unit $j = \sqrt{-1}$
$J$	A/m <sup>2</sup>	Current-density
$k$		Average of second order skin effect factor in the slot
$k$		Average of second order skin effect factor for the coil
$k_{dv}$		Distribution factor
$k_e$		End effect factor
$k_{FtE}$		End effect factor for tangential force component of the ECB
$k_{FnE}$		End effect factor for normal force component of the ECB
$k_{FtL}$		End effect factor for tangential force component of the ALIM
$k_{FnL}$		End effect factor for normal force component of the ALIM
$k_{r1}$		First order skin effect factor
$k_{r2}$		Second order skin effect factor per conductor
$k_{pv}$		Pitch factor
$k_{wv}$		Winding factor
$l$	m	Length
$l_{Fe}$	m	Primary iron length
$l_c$	m	Average length of one turn
$m$		Number of phases
m.m.f.	A	Magnetomotive force
$M$	Nm	Torque
$n$	1/s	Rotational speed
$n$		Denominator of $q$ , if fractional number
$n_{syn}$	1/s	Synchronous rotational speed

$N_c$		Number of turns per coil
$p$		Number of pole pairs
$p_p$		Parameter
$p_{2.0}$	W/kg	Typical power dissipation due to iron losses of a laminated transformer sheet at 2T flux density and 50 Hz frequency
$P_{cu}$	W	Load losses in copper conductors
$P_{cur}$	W	Secondary load losses in copper conductors
$P_{cus}$	W	Primary load losses in copper conductors
$P_d$	W	Total power dissipation in the secondary
$P_f$	W	Friction and total windage losses
$P_{Fe}$	W	Iron losses in magnetically active iron parts
$P_{Fer}$	W	Iron losses in the secondary
$P_{Fes}$	W	Iron losses in the primary
$P_{in}$	W	Input power
$P_{LL}$	W	Additional load losses
$P_{LLr}$	W	Additional load losses in the secondary
$P_{LLs}$	W	Additional load losses in the primary
$P_{mec}$	W	Mechanical power
$P_\delta$	W	Electric air gap power
$q$		Number of slots per pole and phase
$Q$		Number of slots
$Q$	VA	Reactive power
$Q$	N	Weight force
r.m.s.		Root-mean-square
$r$		Integer number
$R$	$\Omega$	Resistance
$R_{Fe}$	$\Omega$	Equivalent core loss resistance
$R_0$	$\Omega$	Conductor resistance per slot at no-load
$R_s$	$\Omega$	Conductor AC resistance per slot
$R_s$	$\Omega$	Resistance of the winding of the primary part (phase value)
$R'_r$	$\Omega$	Conductor resistance of secondary referred to the primary system
$s$		Slip
$s$	m	Length of a section of a curve
$S$	VA	Apparent power
$t$	s	Time
$U$	V	Voltage (r.m.s.)
$U_s$	V	Primary supply voltage (phase value)
$v$	m/s	Speed

$v_{syn}$	m/s	Synchronous linear speed
$V$	A	Magnetomotive force
$V$	V	Electric scalar potential
$w$	m	Equivalent coil span
$w_i$	m	Width of cooling duct
$w_o$	m	Width of conductor
$x$		Displacement direction
$X_h$	$\Omega$	Mutual air gap reactance
$X_s$	$\Omega$	Primary leakage reactance
$X'_r$	$\Omega$	Secondary leakage reactance referred to the primary system
$y$		Displacement direction
$z$		Displacement direction
$z$		Numerator of $q$ , if fractional number
$Z_e$	$\Omega$	End effect impedance
$Z_h$	$\Omega$	Main (vertical branch) impedance
$Z_s$	$\Omega$	Primary winding impedance
$Z'_r$	$\Omega$	Secondary circuit impedance referred to the primary system
$\delta$	m	Air gap length
$\delta_p$	m	Penetration depth, skin depth
$\varepsilon$	As/(Vm)	Permittivity
$\eta$		First order skin effect parameter
$\kappa$	$1/(\Omega \text{ m})$	Conductivity
$\kappa_{prim}$	$1/(\Omega \text{ m})$	Conductivity of the primary part
$\kappa_{rail}$	$1/(\Omega \text{ m})$	Conductivity of the rail
$\mu$	Vs/(Am)	Permeability
$\mu_r$		Relative permeability
$\mu_0$	Vs/(Am)	Permeability of air ( $4 \pi \cdot 10^{-7}$ )
$\nu$		Ordinal number of space harmonics
$\nu_h$		Hollow conductor coefficient
$\xi, \xi^*$		Reduced conductor height
$\pi$		Pi (3.14159)
$\varrho$	As/m <sup>3</sup>	Volume density of charge
$\tau_p$	m	Pole pitch
$\tau_{ps}$	m	Pole pitch of the entry end effect wave
$\varphi$		Skin effect function
$\varphi$	rad	Angle
$\psi$		Skin effect function
$\psi$	A	Total magnetic scalar potential

$\omega$	1/s	Angular speed
$\nabla$		Gradient (nabla) operator ( $\frac{\partial}{\partial x}\vec{e}_x + \frac{\partial}{\partial y}\vec{e}_y + \frac{\partial}{\partial z}\vec{e}_z$ )
$\Delta l$	m	Distance
$\partial$		Partial derivative symbol
2-D		Two-dimensional
3-D		Three-dimensional

## Appendix A

### Material composition of the used rail profiles

Table A.1: Material composition of the used rail profiles [40, 73].

Quality class	Carbon C %	Manganese Mn %	Silicon Si %	Chromium Cr %	Phosphorus P max. %	Sulfur S max. %
700	0.4 - 0.8	0.8 - 1.25	0.05 - 0.35	-	0.05	0.06
900A	0.6 - 0.8	0.8 - 1.3	0.1 - 0.5	-	0.04	0.04
900B	0.55 - 0.75	1.3 - 1.7	0.1 - 0.5	-	0.04	0.04
1100	0.6 - 0.82	0.8 - 1.3	0.3 - 0.9	0.8 - 1.3	-	0.03

# Appendix B

## Finite Element models

Due to the big variety of Finite Element models in this thesis, their main features and the used nomenclature are collected in this chapter. The names for the models have been designed to reflect their features in a simple way:

- The first letter gives the type of machine. An "E" stands for eddy current brake, whereas an "L" stands for linear induction machine.
- The second letter is a number which represents the number of dimensions of the model.
- The third letter symbolizes the scale or boundary condition of the model. Here, an "E" stands for the inclusion of longitudinal end effects, which means that the machine is modeled with its whole length. A "P" symbolizes that the model has periodic boundary conditions, which means that only a periodic part of the machine is modeled.
- For the ALIM, the fourth letter will be either an "F" or a "Y", standing for "F"ractional slot winding and integer slot "Y"oke winding.
- Features which are shared by the majority of models are defined as the standard features and are shown in Table B.1.
- If the model has features differing from the defined standard values, this will be shown by a letter and a number. The letters are " $\kappa$ " for conductivity of the rail, " $\mu$ " for permeability of primary and rail and " $\delta$ " for air gap height.
- For the ALIM, the last letter might be "I" for increased coil height, "O" for open slots, "M" for massive primary and "L" for laminated primary.



In order to illustrate the model names, two different combinations are explained in detail below.

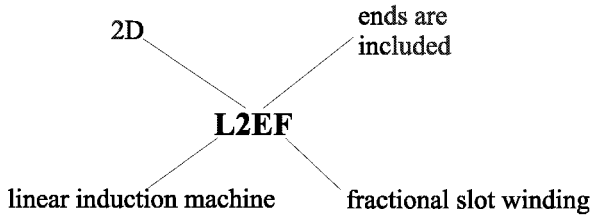
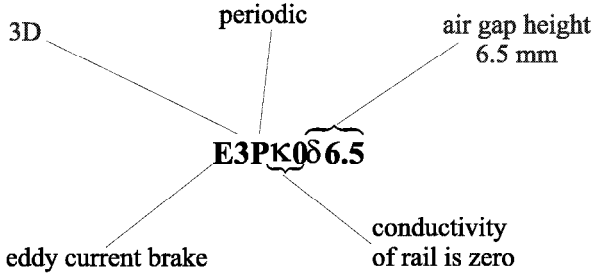


Table B.1: Standard features of the Finite Element models.

Conductivity of primary	$\kappa_{prim} = 0 \text{ S/m}$
Conductivity of rail	$\kappa_{rail} = 5 \cdot 10^6 \text{ S/m}$
Air gap height	$\delta = 6.5 \text{ mm}$
Slot closure	semi-closed
Magnetization	non-linear (ECB: Fig. 3.2, ALIM: Fig. 4.3)
Secondary shape (3-D)	<i>UIC60</i> rail

All different Finite Element models presented in this thesis are listed with their main features and their names in Table B.2

Table B.2: Finite Element models used in the thesis.

Name				E2P	E2E	E3PR				E3P	E3P $\kappa$ 2.5	E2P $\mu$ 1.5	E3P $\kappa$ 0.4	E3P $\kappa$ 0.6	E3P $\kappa$ 0.6.5	E3P $\kappa$ 0.9
Peculiarity							rectangular rail									
Slot design				open slots			open slots			open slots			open slots			
Air gap height $\delta$ / mm				6.5			6.5			6.5			4			
Relative permeability of rail $\mu_{rail}$				non-linear			non-linear			non-linear			1.5			
Relative permeability of primary $\mu_{prim}$				non-linear			non-linear			non-linear			non-linear			
Conductivity of rail $\kappa_{rail}$ / S/m				$5 \cdot 10^6$			$5 \cdot 10^6$			$5 \cdot 10^6$			$2.5 \cdot 10^6$			
Conductivity of primary $\kappa_{prim}$ / S/m				0			0			0			0			
Boundary				per. 180			end			per. 180			per. 0			
Dimensions				2			2			3			3			
Type				ECB			ECB			ECB			ECB			

Table B.2: Finite Element models used in the thesis (continued).

Type	Dimensions	Boundary	$\kappa_{prim} / \text{S/m}$	$\kappa_{rail} / \text{S/m}$	$\mu_{prim}$	$\mu_{rail}$	$\delta / \text{mm}$	Slot design	Peculiarity	Name
ALIM	2	per. 120	0	$5 \cdot 10^6$	non-linear	non-linear	6.5	semi-closed slots	fractional slot winding	L2PF
ALIM	2	end	0	$5 \cdot 10^6$	non-linear	non-linear	6.5	semi-closed slots	fractional slot winding	L2EF
ALIM	3	per. 0	0	$5 \cdot 10^6$	non-linear	non-linear	6.5	semi-closed slots	fractional slot winding	L3PF
ALIM	3	per. 0	0	$5 \cdot 10^6$	non-linear	non-linear	1	semi-closed slots	fractional slot winding	L3PF $\delta$ 1
ALIM	2	per. 0	0	$5 \cdot 10^6$	non-linear	non-linear	4	semi-closed slots	fractional slot winding	L2PF $\delta$ 4
ALIM	2	per. 0	0	$5 \cdot 10^6$	non-linear	non-linear	9	semi-closed slots	fractional slot winding	L2PF $\delta$ 9
ALIM	2	per. 0	0	$5 \cdot 10^6$	non-linear	non-linear	1	semi-closed slots	fractional slot winding	L2PF $\delta$ 1
ALIM	3	per. 180	0	$5 \cdot 10^6$	non-linear	non-linear	6.5	increased coil height	slot winding	L3PY1
ALIM	3	per. 180	0	$5 \cdot 10^6$	non-linear	non-linear	6.5	open slots	yoke winding	L3PYO
ALIM	3	per. 180	0	$5 \cdot 10^6$	non-linear	non-linear	6.5	semi-closed slots	yoke winding	L3PY

Table B.2: Finite Element models used in the thesis (continued).

Name	L3PFO		L3PFI		L3PFδ6M		L3PFδ6L	
Peculiarity	fractional slot winding		fractional slot winding		fractional slot winding		fractional slot winding	
Slot design	open slots		increased coil height		semi-closed slots		semi-closed slots	
$\delta$ / mm	6.5		6.5		6		6	
$\mu_{rail}$	non-linear		non-linear		non-linear		non-linear	
$\mu_{prim}$	non-linear		non-linear		non-linear		non-linear	
$\kappa_{rail}$ / S/m	$5 \cdot 10^6$		$5 \cdot 10^6$		$5 \cdot 10^6$		$5 \cdot 10^6$	
$\kappa_{prim}$ / S/m	0		0		$5 \cdot 10^6$		0	
Boundary	per. 0		per. 0		per. 120		per. 120	
Dimensions	3		3		3		3	
Type	ALIM		ALIM		ALIM		ALIM	

# Appendix C

## Measurement devices

### C.1 Measurement transducer

The measurement transducer is a digital measurement amplifier called *DMCPLUS* [74]. It is controlled by a microprocessor with a sampling rate of up to 9600 samples per second. The accuracy class rating is 0.02 and the resolution is 20 Bit. A photograph of the measurement transducer is given in Figure C.1.

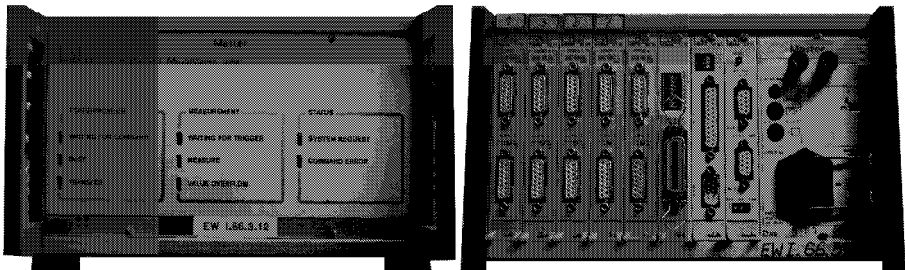


Figure C.1: Measurement transducer in front and rear view.

### C.2 Force transducer

The force transducers are built with eight strain gauges. They are arranged on a steal spring thus, that four of them are stretched and four are compressed when applying a mechanical load. The force transducers are shown in Figure C.2.

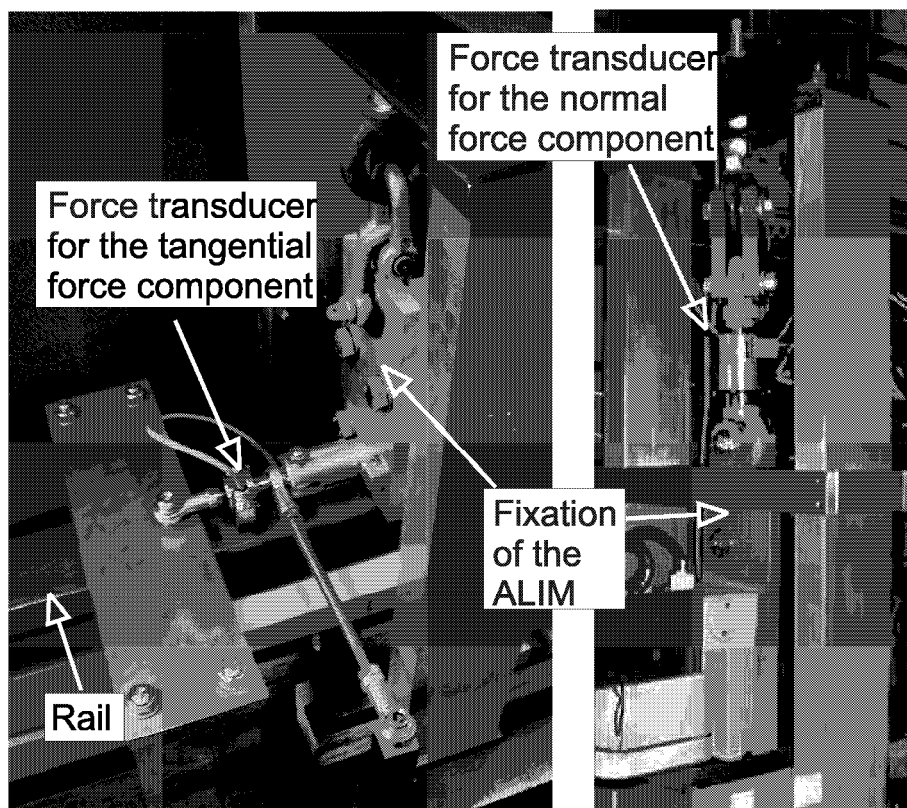


Figure C.2: Force transducers for the measurement of the normal and tangential force component.

### C.3 *Hall* probe

The principle of the *Hall* effect is as follows: A thin metallic plate with a rectangular shape is supplied with a constant DC current from one side to the opposite side. Exposing this plate to a magnetic field normal to the plate surface, there will be a voltage induced in the right angle of the current. This voltage is called *Hall* voltage. In order to obtain the value of flux density from the *Hall* voltage, the correct transformation factor has to be found. This factor is constant for a wide range of flux density values. Nevertheless, it is temperature dependent and for very small flux densities, the transformation is non-linear.

The characteristic of the *Hall* voltage was measured with a defined magnetic field. As shown in Figure C.3, the *Hall* probe was exposed to a constant magnetic field together with a test coil.

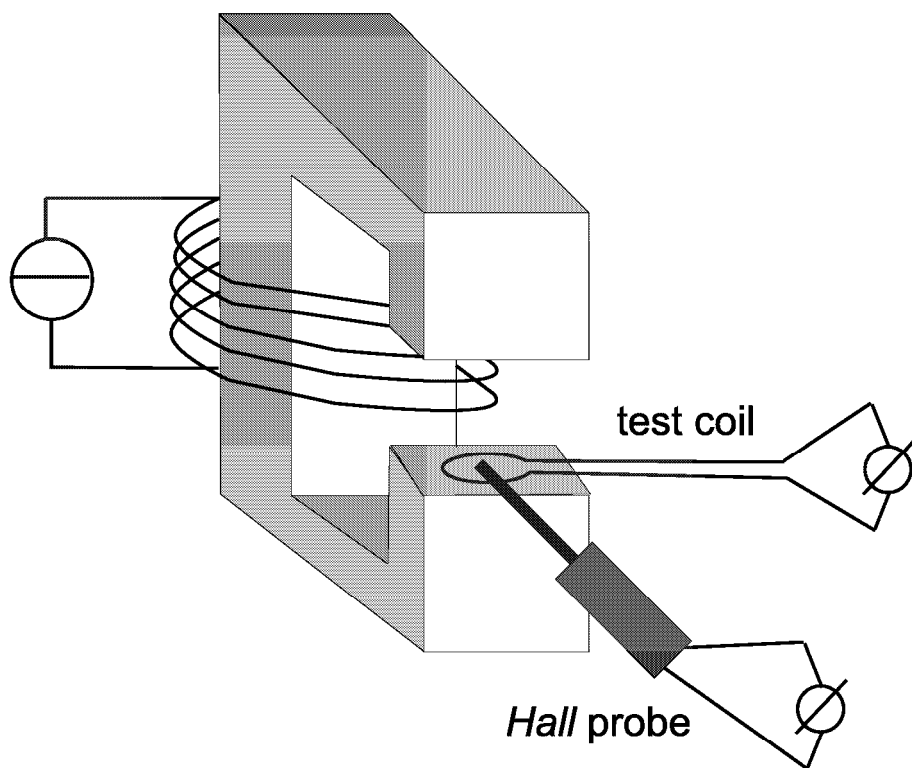


Figure C.3: Test arrangement for the measurement of the *Hall* factor.

The test coil was built with a defined number of turns and cross-section of the wire. The cross-section of the coil perpendicular to the magnetic flux was known. A flux measuring device was used to measure the flux. The *Hall* probe was fixed in the middle of the reference cross-section of the test coil and together with the flux from the test coil, the *Hall* voltage of the *Hall* probe was measured. For the verification of the test results, two calibrated permanent magnets were used as a reference. The measured factor is shown in Figure C.4.

For each *Hall* voltage, there is a factor which gives the flux density at that point. The resulting flux density is also shown in Figure C.4.

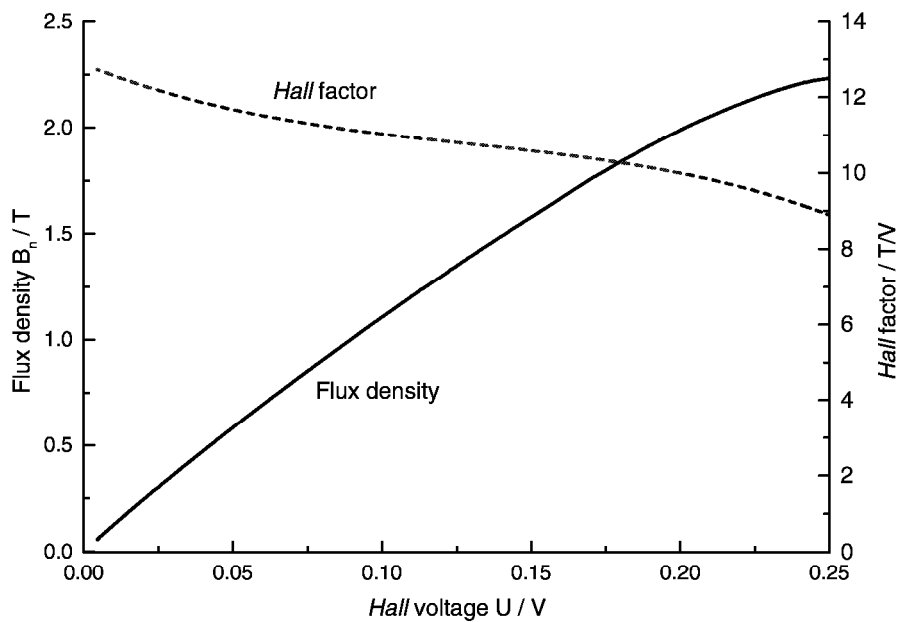


Figure C.4: *Hall* factor and flux density values depending on the *Hall* voltage.



# Appendix D

## Locomotive *BR152*

The main data of the freight train locomotive *BR152* are collected in Table D.1. The block diagram for one bogie of the locomotive is shown in Figure D.1 [75].

Table D.1: Main data of the locomotive *BR152*.

Voltage	15 kV
Frequency	16 2/3 Hz
Tractive effort on starting	300 kN
Power	6400 kW
Maximum speed	140 km/h
Weight	86.7t
Length	19 580 mm
Width	3 000 mm

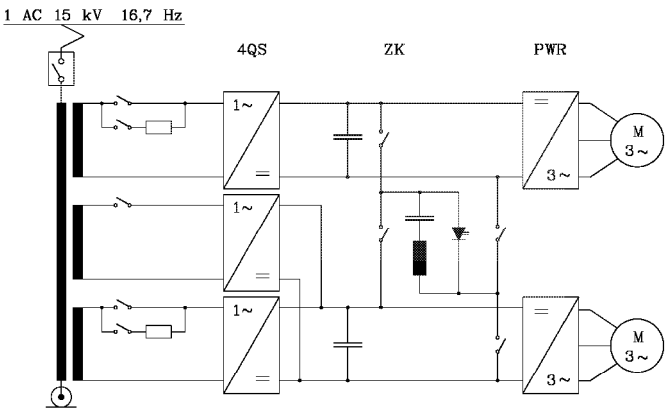


Figure D.1: Block diagram for one bogie of the *BR152* [75].

# Bibliography

- [1] M. Buscher, R. Pfeiffer, H.-J. Schwartz, “Radschlupfregelung für Drehstromlokomotiven (Slip control for locomotives).” *Elektrische Bahnen*, vol. 91, no. 5, pp. 163–178, 1993.
- [2] U. Kröger, “Prinzip, Entwicklung und Konstruktion der linearen Wirbelstrombremsen (Principle, design and construction of linear eddy current brakes).” *ZEV Glasers Annalen*, vol. 109, pp. 368–374, September 1985.
- [3] H. E. Walter, “Electro-magnetic brake.” U.S. Patent No.467243, 1892.
- [4] W. D. Meier-Credner, “Die lineare Wirbelstrombremse - Entwicklung und Einsatz im ICE 3 (The linear eddy current brake - design and application in the ICE 3).” *ETR - Eisenbahntechnische Rundschau*, vol. 49, pp. 412–418, June 2000.
- [5] H. W. Wilson, “Electrification of railways.” *Transactions of the Liverpool Engineering Society*, vol. 26, p. 218, 1905.
- [6] A. Zehden, “Electro-magnetic brake.” U.S. Patent No.732312, 1905.
- [7] E. R. Laithwaite. *Linear electric motors*. Mills & Boon, London, 1971.
- [8] J. Meins, L. Miller, W. J. Mayer, “The high speed maglev transportation system transrapid.” *IEEE Transactions on Magnetism*, vol. 24, pp. 808–811, March 1988.
- [9] D. Albertz, S. Dappen, G. Henneberger, “Calculation of the 3D non-linear eddy current field in moving conductors and its application to braking systems.” *IEEE Transactions on Magnetism*, vol. 32, pp. 768–771, May 1996.
- [10] F. Löser, W. Ruoss, Ph. K. Sattler, “Eddy-current brake system for Transrapid 07.” *Proceedings of the MAGLEV 1988*, pp. 175–184, 1988.
- [11] G. Hartz. *Numerische Berechnung der Felder, Wirbelströme und Kräfte in einer linearen Wirbelstrombremse (Numerical calculation of fields, eddy currents and forces of a linear eddy current brake)*. PhD thesis, RWTH Aachen, Germany, 1985.
- [12] S. Yamamura. *Theory of linear induction motors*. Halsted Press, Tokyo, 1979.

- [13] J. F. Gieras. *Linear induction drives*. Oxford university press, Oxford, 1994.
- [14] S. Yamamura, H. Itoh, F. J. Ahmed, "End effects of linear induction motor." *Electrical Engineering in Japan*, vol. 90, no. 2, pp. 20–30, 1970.
- [15] E. R. Laithwaite. *Induction machines for special purposes*. John Wright & Sons, London, 1966.
- [16] K. Vogt. *Berechnung elektrischer Maschinen (Calculation of electrical machines)*. VCH, Weinheim, 1996.
- [17] A. Binder, "Elektrische Maschinen und Antriebe (Electrical machines and drives)." Skript zur Vorlesung, Institute of Electrical Energy Conversion, Darmstadt University of Technology, Germany, 2000.
- [18] M. G. Say. *Alternating current machines*. Longman scientific & technical, London, 1992.
- [19] S. J. Chapman. *Electric machinery fundamentals*. McGraw-Hill, New York, 1991.
- [20] M. Liwischitz-Garik, C. C. Whipple. *Electric machinery*. Van Nostrand, New York, 1946.
- [21] A. Binder, G. Neidhöfer, "Grossgeneratoren und Hochleistungsantriebe (Large Generators and High Power Drives)." Skript zur Vorlesung, Institute of Electrical Energy Conversion, Darmstadt University of Technology, Germany, 1999.
- [22] H. Sequenz. *Die Wicklungen elektrischer Maschinen (Windings of electric machines)*, vol. 3: Wechselstrom-Sonderwicklungen. Springer, Wien, 1954.
- [23] DIN EN 60034-2. *IEC 60034-2: Drehende elektrische Maschinen - Teil 2: Verfahren zur Bestimmung der Verluste und des Wirkungsgrades von drehenden elektrischen Maschinen aus Prüfungen (ausgenommen Maschinen für Schienen- und Strassenfahrzeuge)*. Beuth Verlag, Berlin, 1998.
- [24] H. Clausert, G. Wiesemann. *Grundgebiete der Elektrotechnik 2 (Basics of electrical engineering)*. Oldenbourg Verlag, München, 1992.
- [25] S. R. H. Hoole, P. R. P. Hoole. *A modern short course in engineering electromagnetics*. Oxford University Press, New York, 1996.
- [26] T. Tärnhuvud, K. Reichert, "Accuracy problems of force and torque calculation in FE-systems." *IEEE Transactions on Magnetics*, vol. 24, pp. 443–446, January 1988.
- [27] E. W. Curtius, A. Kniffler, "Neue Erkenntnisse über die Haftung zwischen Treibrad und Schiene (New discoveries on the adhesion between wheel and rail)." *Elektrische Bahnen*, no. 9, pp. 201–210, 1950.

- [28] M. N. O. Sadiku. *Numerical techniques in electromagnetics*. CRC Press, Los Angeles, 1992.
- [29] U. v. Rienen. *Numerical methods in computational electrodynamics: linear systems in practical applications*. Springer, Berlin, 2001.
- [30] M. Clemens. *Zur numerischen Berechnung zeitlich langsam veränderlicher elektromagnetischer Felder mit der Finiten-Integrations-Methode (On the numerical calculation of slowly varying electromagnetic fields with FIT)*. PhD thesis, TU Darmstadt, Germany, 1998.
- [31] D. Rodger et al., “MEGA V6.24 User Manual.” Distributed with the program package MEGA, Applied Electromagnetics Research Centre, Bath University, UK, 1997.
- [32] J. Jin. *The finite element method in electromagnetics*. John Wiley & Sons, New York, 1993.
- [33] P. J. Leonard, D. Rodger, T. Karagular, P. C. Coles, “Finite Element modelling of magnetic hysteresis.” *IEEE Transactions on Magnetics*, vol. 31, pp. 1801–1804, May 1995.
- [34] W. F. Ames. *Numerical methods for partial differential equations*. Academic Press, New York, 1977.
- [35] Ch. Cuevas, “Regularization methods for solution of linear systems.” *Paper at the Computing Research Conference CRC 2000, Puerto Rico*, 2000.
- [36] Deutsche Bahn, “Eisenbahn- Bau- und Betriebsordnung (EBO).” Bundesminister für Verkehr, 1992.
- [37] “UIC-Kodex, Eisenbahnfahrzeuge, Fahrzeugbegrenzungslinien.” Internationaler Eisenbahnverband, 1993.
- [38] DIN EN 50121 Part 1-5. *Bahnanwendungen - Elektromagnetische Verträglichkeit - Teil 1-5*. Beuth Verlag, Berlin, 2000.
- [39] Deutsche Bahn, “Grenzwerte für die Zulassung von Schienenfahrzeugen aus beeinflussungsschutztechnischer Sicht.” Eisenbahnbundesamt, 1996.
- [40] DIN EN 13674-1. *Bahnanwendungen - Oberbau; Schienen - Teil 1: Symmetrische Breitfußschienen ab 46 kg/m*. Beuth Verlag, Berlin, 1999.
- [41] R. Günther, “Verkehrswesen III, Kapitel 5: Oberbau (Transportation).” Skript zur Vorlesung, Department of Transportation, Technische Fachhochschule Berlin, Germany, 2000.

- [42] W. Lössel, H. Landwehr, J. Prem, "ICE 3 - New generation of european high speed trains." *RTR*, vol. 1, pp. 2–18, 1997.
- [43] A. Nefzger, "Geometrie der Berührung zwischen Radsatz und Gleis (Geometry of the wheel-rail contact)." *ETR - Eisenbahntechnische Rundschau*, no. 3, pp. 113–122, 1974.
- [44] M. Cinotti. "Investigations on an asynchronous linear motor for railway vehicles - Numerical analysis of the longitudinal end-effects.". Master's thesis, Institute of Electrical Energy Conversion, Darmstadt University of Technology, Darmstadt, Germany, 1999.
- [45] J. D. Edwards, B. V. Jayawant, W. R. C. Dawson, D. T. Wright, "Permanent-magnet linear eddy-current brake with a non-magnetic reaction plate." *IEEE Proc.-Electr. Power Appl.*, vol. 146, pp. 627–631, November 1999.
- [46] R. L. Russell, K. H. Norsworthy, "Eddy current and wall losses in screened-rotor induction motors." *Proc. IEE*, pp. 163–175, April 1958.
- [47] P. J. Wang, S. J. Chiueh, "Analysis of eddy-current brakes for high speed railway." *IEEE Transactions on Magnetics*, vol. 34, pp. 1237–1239, July 1998.
- [48] N. Takahashi, S. Kawai, K. Akihashi, "Analysis of rail eddy-current brake for high-speed railroad vehicles." *Electrical Engineering in Japan*, vol. 90, no. 2, pp. 95–104, 1970.
- [49] G. Hartz, Ph. K. Sattler, "Linear eddy-current brake with ferromagnetic reaction-rail. Numerical calculation of the field and of the braking force." *Archiv für Elektrotechnik*, vol. 69, pp. 351–357, 1986.
- [50] N. Allen, D. Rodger, P. C. Coles, S. Street, P. J. Leonard, "Towards increased speed computations in 3D moving eddy current finite element modelling." *IEEE Transactions on Magnetics*, vol. 31, pp. 3524–3526, November 1995.
- [51] P. J. Leonard, D. Rodger, "Comparison of methods for modelling jumps in conductivity using magnetic vector potential based formulations." *IEEE Transactions on Magnetics*, vol. 33, pp. 1295–1298, March 1997.
- [52] Th. Werle, A. Binder, "Asynchronous linear machine as booster for railway vehicles." *Eighth international conference on power electronics, IEE 2000*, vol. Conference proceedings, no. 475, pp. 224–228, 2000.
- [53] R. Boll. *Weichmagnetische Werkstoffe (Soft-magnetic materials)*. Vacuumschmelze GmbH, Hanau, 1990.
- [54] J. Brechtel. "Numerische Berechnungen zum Betriebsverhalten von asynchronen Linear-maschinen im Rad-Schiene-System (Numerical calculations of the performance of linear

- induction machines in the wheel-rail system).”, Institute of Electrical Energy Conversion, Darmstadt University of Technology, Germany, 1999, unpublished.
- [55] Th. Gerhard, “Neuentwicklungen für den ICE 3 (New developments for the ICE 3).” *ETR - Eisenbahntechnische Rundschau*, vol. 46, pp. 427–432, July/August 1997.
- [56] M. Hofmann, Th. Werle, A. Binder, R. Pfeiffer, “Asynchronous Linear Machine for Railway Systems.” *Transactions of the ICEM*, pp. 223–227, 2000.
- [57] B. W. Smith, “Sixty Centuries of Copper.” UK Copper Development Association, 1965.
- [58] W. J. Jeon, S. Katoh, T. Iwamoto, Y. Kamiya, T. Onuki, “Propulsive characteristics of a novel linear hybrid motor with both induction and synchronous operations.” *IEEE Transactions on Magnetics*, vol. 35, pp. 4025–4027, September 1999.
- [59] J. F. Gieras, “Analysis of a single-sided linear induction motor using an equivalent circuit with longitudinal end-effect taken into account.” *etzArchiv*, vol. 7, no. 12, pp. 405–408, 1985.
- [60] J. Faiz, H. Jafari, “Accurate modeling of single-sided linear induction motor considers end-effect and equivalent thickness.” *IEEE Transactions on Magnetics*, vol. 36, pp. 3785–3790, September 2000.
- [61] M. Iwamoto, E. Ohno, T. Itoh, Y. Shinryo, “End-effect of high-speed linear induction motor.” *IEEE Transactions on Industry Applications*, vol. 9, pp. 632–639, November/December 1973.
- [62] S. Yamamura. *Theory of linear induction motors*. John Wiley & Sons, New York, 1972.
- [63] Y. Mori, S. Torii, D. Ebihara, “End effect analysis of linear induction motor based on the wavelet transform technique.” *IEEE Transactions on Magnetics*, vol. 35, pp. 3739–3741, September 1999.
- [64] U. Feldmann, “Ermittlung einer günstigen Polzahl bei asynchronen Linearmotoren mit vorgegebenen Abmessungen und grossen Geschwindigkeiten (Estimation of the number of poles for linear induction machines).” *etz-a*, vol. 97, no. 4, pp. 195–204, 1976. Vortrag und Diskussion.
- [65] W. Schuisky. *Berechnung elektrischer Maschinen (Calculation of electrical machines)*. Springer Verlag, Wien, 1960.
- [66] G. R. Slemon. *Electric machines and drives*. Addison-Wesley, Boston, 1992.
- [67] H. Kuchling. *Taschenbuch der Physik (Physics)*. Fachbuchverlag, Leipzig, 1996.

- [68] P. Guillery. *Werkstoffkunde für Elektroingenieure (Materials for engineers)*. Vieweg, Braunschweig, 1974.
- [69] H. Speckhardt, “Einführung in die Werkstoffkunde für Elektrotechniker (Introduction to materials for electrical engineers).” Skript zur Vorlesung, Institute of Materials, Darmstadt University of Technology, Germany, 1988.
- [70] Hottinger Baldwin Messtechnik, “DMCLABplus - Bedienungsanleitung.” Manual, 1994.
- [71] S. G. Rabinovich. *Measurement Errors and Uncertainties*. Springer Verlag, New York, 1999.
- [72] S. Salon, D. Burow, M. DeBortoli, C. Slavik, “Effects of Slot Closure and Magnetic Saturation on Induction Machine Behavior.” *IEEE Transactions on Magnetism*, vol. 30, pp. 3697–3700, September 1994.
- [73] DIN 5901. *Breitfußschienen - Maße, statische Werte und Stahlsorten*. Beuth Verlag, Berlin, 1995.
- [74] Hottinger Baldwin Messtechnik, “Digitales Messverstärker-System DMCplus - Technische Spezifikationen (Specifications).” Manual, 1993.
- [75] J. Wach, E. Mittendorf, W. Lössel, “Die Lokomotive der Baureihe 152 (The locomotive BR 152).” *ZEVI + DET Glasers Annalen*, vol. 122, no. 9-10, pp. 385–393, 1998.

# Index

- 3-D model, 25
- abstract, vii
- adhesion coefficient, 19
- Ampere's law*, 17
- available space, 32
- base plane, 25
- chording, 9
- coil parameters, 12
  - coil resistance, 14, 83
  - hollow conductor coefficient, 14
- current-density, 14, 17
- current-sheet, 16
- discretization error, 22
- distribution factor, 10
- eddy current brake, 35–56, 106–110
  - circuit diagram, 108
  - eddy current distribution, 51
  - end effect factor, 44
  - flux density, 41, 48, 54, 110
  - longitudinal end effect, 38, 40
  - measured forces, 2, 51
  - measurement, 106
  - models, 37, 45, 129
  - normal force, 40, 47, 53, 109
  - tangential force, 41, 47, 53
  - transversal end effect, 46, 48
- eddy currents, 27
- electric scalar potential, 24
- electromagnetic theory, 20
- Faraday's law*, 18
- Finite Difference Method, 21
- Finite Element Method, 21
- Finite Element models, 129
- Finite Integration Technique, 21
- flux density, 17
- flux lines, 7, 39, 43, 76
- frequency inverter, 2, 62, 121
- Hall effect*, 135
- harmonics, 9, 10
- hollow conductor, 14
- ICE 3* bogie, 34
- introduction, 1
- linear induction machine, 2–4, 57–105, 111–116
  - circuit diagram, 113
  - coil parameters, 84
  - conductivity, 103
  - current, 115
  - design parameters, 60, 72
  - eddy current distribution, 100
  - end effect factor, 81
  - end effects, 5
  - equivalent circuit, 8
  - flux density, 69, 75, 89, 102
  - flux density distribution, 100
  - fractional slot winding, 60
  - harmonics, 69, 92, 115
  - history, 3
  - integer slot yoke winding, 70
  - longitudinal end effect, 75



- measurement, 98, 111
- mesh, 65, 74
- models, 63, 71, 73, 129
- natural frequency, 116
- normal force, 66, 86, 87, 99, 116
- power, 94
- tangential force, 66, 86, 87, 99, 116
- tractive effort, 88
- transversal end effect, 63
- vector plot, 93
- winding concepts, 57
- winding factors, 59
- working principle, 5
- locomotive *BR152*, 138
- longitudinal end effect, 5, 23
- magnetic vector potential, 23, 24, 39
- magnetization curves, 35, 59
- material composition of rail, 128
- Maxwell* equations, 20
- Maxwell* stress tensor, 23
- measurement devices, 134
- MEGA*, 22
- mounting methods, 31
- normal force, 18
- number of slots per pole and phase, 10
- numerical methods, 20
- penetration depth, 12, 46
- periodic boundary conditions, 23
- pitch factor, 9
- pole pitch, 75
- power
  - air gap power, 16
  - input power, 16
  - losses, 15
  - mechanical power, 16
  - power factor, 16
  - power flow diagram, 15
- rail conductivity, 119
- rail profile, 30
- railway regulations, 28
- Roebel* bars, 13
- rotor frequency, 112
- round-off error, 22
- skin depth, 98
- skin effect, 12, 85
- slip, 7
- symmetric boundary conditions, 23
- synchronous velocity, 7
- tangential force, 18
- thermal load, 16
- tractive effort, 18
- transversal end effect, 6, 23
- vertical field, 85
- wheel-rail contact, 1, 18, 20
- winding factor, 11